DESIGN SYNTHESIS AND MINIATURIZATION OF MULTIBAND AND RECONFIGURABLE MICROSTRIP ANTENNA FOR FUTURE WIRELESS APPLICATIONS

QI LUO

A Dissertation Submitted to Departamento de Engenharia Electrotécnica e de Computadores, Faculdade de Engenharia da Universidade do Porto in Partial Fulfillment of the Requirements for the Degree of Doctor of Philosophy

July 2012

Qi Luo: *Design Synthesis and Miniaturization of Multiband and Reconfigurable Microstrip Antenna for Future Wireless Applications,* A Dissertation Submitted to Departamento de Engenharia Electrotécnica e de Computadores, Faculdade de Engenharia da Universidade do Porto in Partial Fulfillment of the Requirements for the Degree of Doctor of Philosophy, © July 2012

THESIS IDENTIFICATION

Title:	Design Synthesis and Miniaturization of Multiband and Reconfigurable Microstrip Antenna for Future Wireless Applications
Keywords:	Monopole Antenna, Fractal Antenna, Antenna Array, Electrically Small Antenna, Compact Antenna, Reconfigurable Antenna, Artifical Magnetic Condutor
Start:	November 2007
Duration:	4 years
Candidate information:	
Name:	Qi Luo
E-Mail:	qiluo@ieee.org
Curriculum Vitae:	http://www.linkedin.com/in/luoqi
Supervisor information:	
Name:	Henrique Manuel de Castro Faria Salgado
E-Mail:	hsalgado@fe.up.pt
Curriculum Vitae:	http://www2.inescporto.pt/utm-en/author/hsalgado
Co-supervisor information:	
Name:	Jose Rocha Pereira
E-Mail:	jrp@ua.pt
Curriculum Vitae:	http://www.it.pt/person_detail_p.asp?id=468
Educational Establishment:	Faculdade de Engenharia da Universidade do Porto-MAPTELE PhD Program
Research Institution:	INESC Tech

STATEMENT OF ORIGINALITY

The work presented in this thesis was carried out by the candidate. It has not been presented previously for any degree, nor is it present under consideration by any other degree awarding body.

Candidate: _____

(Qi Luo)

Principal Supervisor: _____

(Henrique Salgado)

Co-supervisor: _____

(Jose Rocha Pereira)

STATEMENT OF AVAILABILITY

I hereby give consent for my thesis, if accepted, to be available for photocopying and for interlibrary loan, and for the title and summary to be made available to outside organizatioins.

Candidate:

(Qi Luo)

Porto, Portugal, July 2012

ABSTRACT

This thesis is concerned with the design of compact multiband/reconfigurable antennas and antenna arrays for wireless applications.

The size reduction of an antenna has an impact on its radiation performance. Hence, methodologies for the design of compact size antennas with promising radiation characteristics are addressed in this work by employing novel techniques for antenna miniaturization based on fractal geometries and by introducing lumped elements to the printed monopole antenna design. Using fractal geometries three multiband fractal monopole antennas, one fractal-based Inverted-L antenna and one single feed fractal monopole antenna array are presented. The experiment and simulation results of the proposed fractal antennas prove the advantages of fractal antennas, namely, compact size, multi-frequency operation and wide operation bandwidth. A second approach addressed in this work is the application of a technique which includes a chip inductor into the antenna structure for the purpose of reducing antenna size. By investigating the equivalent circuit structure of the chip inductor, a design approach that involves the chip inductor to design a multiband antenna is proposed. Using this methodology two electrically small antennas for dual band WLAN as well as one compact antenna for multiband mobile communication that can cover almost the entire commercial available frequency bands were developed and their performances are discussed.

Moreover, the design of compact antenna arrays is also investigated. The approach discussed in this work to design compact multiband antenna arrays that contain closely space antennas, is to apply both the neutralizing and reconfigurable techniques on the printed monopole antenna array. One compact size antenna array was developed for the WLAN 5.8 GHz USB dongle MIMO application. The other antenna presented is a reconfigurable compact dual band monopole antenna array that can operate at each of the two WLAN frequency bands whilst exhibiting high isolation. Additionally, innovative methods for the design of reconfigurable antennas are also investigated. The approach adopted to design the reconfigurable antenna is based on the concept of active Artificial Magnetic Conductor ground plane. Here a new design is proposed using RF switches mounted on the surface of the AMC that consists of periodic square elements. After optimization, the resonant frequency of the coplanar antenna can be tuned by using such an active AMC ground plane, whose reflection phase is controlled by the states of the RF switches.

These antennas have been implemented and characterized. The numerical simulations conducted in the Finite Element Method based

electromagnetic simulation software package, Ansoft HFSS, are shown to match well with experimental results which proves the adequacy of the techniques devised.

RESUMO

Esta Tese aborda o projecto de antenas compactas, multibanda e reconfiguráveis para aplicações em comunicações sem fios.

A redução do tamanho duma antena tem um impacto negativo no desempenho das suas características de radiação. Por consequência, são abordadas nesta tese metodologias para projectar antenas com características de radiação promissoras empregando novas técnicas de miniaturização baseadas em geometrias fractais e na introdução de elementos discretos no projecto de antenas impressas do tipo monopolo. Usando geometrias fractais, apresentam-se aqui três antenas multibanda do tipo monopolo, uma Inverted-L Antenna e um agregado de duas antenas monopolo. Os resultados experimentais e os obtidos por simulação das antenas fractais propostas provam as vantagens destas antenas, nomeadamente no que diz respeito ao tamanho compacto, à operação multifrequência e à grande largura de banda. Uma segunda abordagem usada neste trabalho é a utilização de uma técnica que usa um elemento indutivo compacto inserido na estrutura da antena com o fim de reduzir o seu tamanho. Analisando a estrutura do circuito equivalente do elemento indutivo, propõe-se uma abordagem adequada para o projecto de antenas multibanda que envolve a utilização destes elementos indutivos na implementação de antenas de reduzida dimensão. Usando esta metodologia foram desenvolvidas e analisadas duas antenas eletricamente pequenas de banda dupla para WLAN, assim como uma antena compacta, para comunicações móveis multibanda, que pode cobrir quase todas as bandas de frequência comerciais disponíveis.

Além disso, foi também investigado o projecto de agregados de antenas compactos. A abordagem usada neste trabalho para projectar agregados de antenas multibanda compactos que contêm antenas muito próximas, consistiu na aplicação das técnicas de neutralização e de reconfiguração a antenas impressas do tipo monopolo. Um agregado de antenas compacto, inserido num dispositivo dongle USB foi desenvolvido para uma aplicação MIMO WLAN a 5.8GHz. A outra antena aqui apresentada é um monopolo compacto reconfigurável e de banda dupla que pode operar em cada uma das duas bandas de frequências WLAN exibindo, mesmo assim, um isolamento elevado. Foram também investigados métodos inovadores para o projeto de antenas reconfiguráveis. A abordagem adoptada para projetar estas antenas baseia-se no conceito de condutor magnético artificial, Artificial Magnetic Conductor (AMC). Por optimização a frequência

de ressonância da antena coplanar pode ser sintonizada usando este AMC activo, cuja fase da reflexão é controlada pelo estado dos interruptores de RF.

Todas as antenas foram construídas e caracterizadas. As simulações numéricas foram realizadas usando o software de simulação eletromagnética HFSS da Ansoft baseado no Método dos Elementos Finitos (FEM). Obteve-se um bom acordo entre os resultados de simulação e experimentais o que comprova a adequação das técnicas desenvolvidas e utilizadas.

ACKNOWLEDGMENTS

It would not have been possible to write this doctoral thesis without the help and support of the kind people around me. First and foremost, I would like to thank my parents. Without out their love, support and encourage, I would not able to go abroad and accomplish what I have done. I would also like to thank my girlfriend, Yu Xin Du, for her persistent support and encourage during these years.

I would like to express my appreciation to my supervisors, Prof. Henrique Salgado and Prof. Jose Rocha Pereira, for accepting me as a Ph.D student. I appreciate all their contributions of time and advices to make my Ph.D experience productive and stimulating. Without their continuous support, patience, enthusiasm, and motivation, I would not accomplish this work. Their guidance helped me in all the time of research and writing of this thesis and I could not have imagined having a better advisor and mentor for my Ph.D study.

Besides my supervisors, I would like to thank the rest of my thesis committees, Prof. Artur Moura, Prof. Custódio Peixeiro, Prof. José Rodrigues Rocha and Prof. Pedro Pinho, for their encouragement, insightful comments, and hard questions.

I would like to acknowledge the Fundação para a Ciência e a Tecnologia (FCT), Portugal in the award of a PhD grant that provided the necessary financial support for this research. I also would like to thank the staff at the Department of Electrical and Computer Engineering, University of Porto and Instituto de Telecomunicações (IT) Aveiro for their assistance and positive attitude. I would like to express my thanks to Paulo Gonçalves and Carlos Graf for their help in fabricating the antenna prototypes for my research work.

Last but not least, I wish to express my greatest thanks to the friends and colleagues, who have supported and helped me during my staying in Portugal in the past five years. Their friendship is a treasure to me and without them, I could not enjoy my staying and have such a nice life experience in Portugal.

CONTENTS

LIST OF FIGURES

LIST OF TABLES

LIST OF ACRONYMS

AC	Alternating Current
AMC	Artificial Magnetic Conductor
DC	Direct Current
DCS	Digital Communications System
DNG	Double Negative
DVB	Digital Video Broadcasting
EBG	Electromagnetic Band-Gap
EM	Electromagnetic
ESA	Electrically Small Antenna
FDTD	Finite-Difference Time-Domain
FEM	Finite Element Method
HFSS	High Frequency Structure Simulator
HIP	High Impedance Surface
IEEE	Institute of Electrical and Electronics Engineers
IFA	Inverted-F Antenna
IFS	Iterated Function System
ILA	Inverted-L Antenna
GPS	Global Positioning System
GUI	Graphical User Interface
GSM	Global System for Mobile Communications
LTE	Long Term Evolution
MIMO	Multiple Input Multiple Output
MoM	Method of Moments
MEMS	Micro-electromechanical Systems
PCB	Printed Circuit Board
PCS	Personal Communications Service
PDA	Personal Digital Assistant
PEC	Perfect Electrical Conductor
PIFA	Planar Inverted-F Antenna
PMC	Perfect Magnetic Conductor
PRS	Partial Reflection Surface
Q	Quality Factor
RF	Radio Frequency
RLC	Resistor-Inductor-Capacitor
SAR	Specific Absorption Ratio
TMRL	Total Multiport Return Loss

UMTS	Universal Mobile Telecommunications System
USB	Universal Serial Bus
WiMAX	Worldwide Interoperability for Microwave Access
WLAN	Wireless Local Area Network
WWAN	Wireless Wide Area Network
ZOR	Zeroth Order Resonator

1 INTRODUCTION

1.1 MOTIVATION

An antenna is an electrical device that converts electric currents into radio waves, and vice versa. It is a key component for all wireless communication equipments and it is critical in deciding the quality of the radio communication. To reach the resonant condition, the dimension of the antenna must be a fraction of the wavelength at its resonant frequency. This means that the lower resonant frequency is, the larger the size of the antenna will be. The currently available and future commercial wireless systems require antennas to have wide bandwidth to support higher data rate and be able to operate at multiple frequency bands defined by various protocols. Take mobile phone communication system as an example. Mobile communications have experienced rapid development in recent years, as presented in Figure 1. Currently the 3rd generation of mobile network, UMTS (1920-2170 MHz) system, has been widely deployed. In the near future, it is expected that Worldwide Interoperability for Microwave Access (WiMAX) and Long Term Evolution systems (LTE) will be implemented on the mobile network to support a higher data rate. According to the LTE protocol, the LTE-Advanced update is expected to offer peak rates up to 1 Gbit/s fixed speeds and 100 Mb/s to mobile users [1].

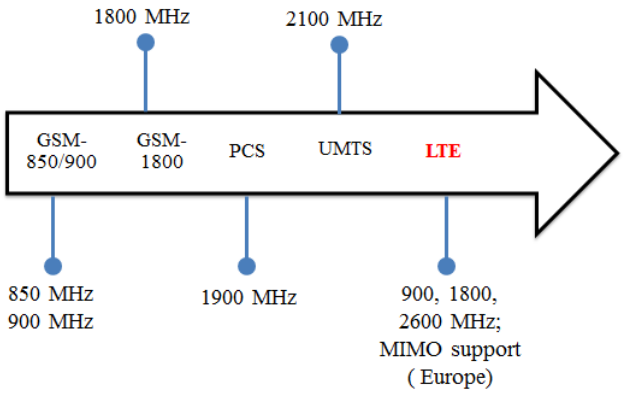

Figure 1: The evolution of the mobile communication standards

The hardware design specifically the antennas also had a large evolution. The first mobile phone antennas were simple monopole or spiral antennas, which can only operate at a single frequency band, located outside the shell of mobile devices. Nowadays, given various wireless protocols, in the physical layer the needs for multiband antennas are increasing. To support different mobile networks, it is re-

quired to have the handset be equipped with an multiband antenna, a quad-band or even penta-band antenna for example, or multiple antennas. LTE requires Multiple Input Multiple Output (MIMO) techniques to be employed on the mobile devices [2]. In order to enable one mobile device to support all of these mobile wireless protocols, at the physical layer, it is essential to have one multiband antenna or even an multiband antenna array integrated on this mobile device.

Similarly, in the evolution of the Wireless LAN (WLAN) communications (Figure 2), different frequency bands have been allocated with the release of newly developed standards. Nowadays, the requirement of WLAN antennas has been changed from single frequency band operation at 2.4 GHz to multiband operation that can support both 2.4 and 5.2/5.8 GHz (2.41-2.48 GHz, 5.250 - 5.350 GHz and 5.725-8.825 GHz). Under the newly released 802.11n standard, it is also required to include the MIMO techniques, which means that more than one antenna has to be equipped in one device [3].

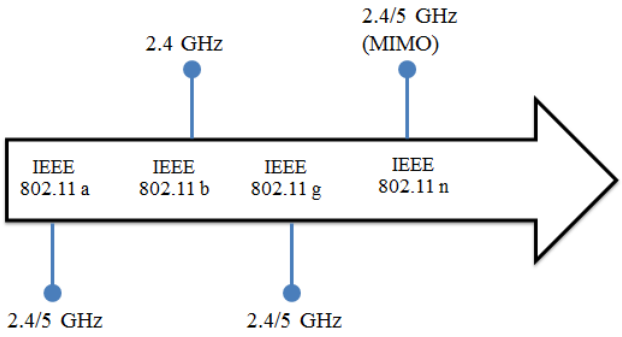

Figure 2: The evolution of the Wireless LAN standards

It is clear that the trend for the antenna engineering is to design compact antennas or antenna arrays that can operate at multiple commercial frequency bands with adequate bandwidth and gain. Figure 3 is an example of a PDA device, which needs not only to operate at different mobile networks but also support WLAN as well as the WiWAX and DVB. This requires more than one multiband antenna to be equipped on the mobile device.

Either designing a multiband antenna or including an extra antenna element to make an antenna array will lead to the increase of the overall size of the antenna system. However, the fact is that the available volume for antenna design keeps decreasing as it is desirable to have one wireless device, especially a portable device, as compact as possible. It is known that theoretically the antenna's performance degrades when the size of the antenna is reduced. Current internal antenna designs are already pushing the limit of fundamental performance of electrically small antennas. Moreover, another challenge issue that needs to be solved is how to include an antenna array on a portable device to support MIMO communications as nor-

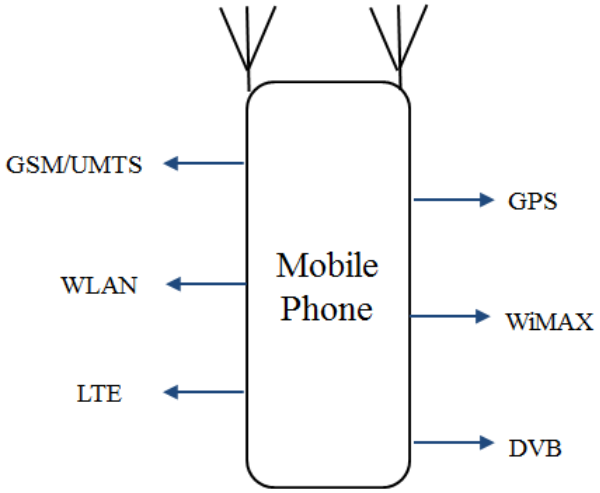

Figure 3: Example of different standards that need to be supported by a future mobile phone

mally the distance between two antennas has to be approximately half a wavelength at the frequency of interested in order to reach a better isolation and low spatial correlation [4]. Therefore, new techniques for designing compact and multiband antenna and antenna array need to be investigated, which is the key motivation of this thesis work.

1.2 APPROACH

1.2.1 *Compact Multiband Antenna Design using Fractals*

The first approach that has been employed is the use of fractal geometries to design compact multiband printed monopole antennas. Fractal geometry is a family of geometries that have the characteristics of inherent self-similar or self-affinity, which were used to describe and model complex shapes found in nature such as mountain ranges, waves and trees [5]. Recently, fractal techniques have been brought to the field of electromagnetic theory research, which is called fractal electrodynamics; it has also been implemented in antenna design, named "fractal antenna engineering", and is attracting many research interests [6, 7, 8, 9].

There are several advantages of using fractal geometries in antenna design. First of all, it can reduce the size of antenna, which makes it a good candidate for miniature antenna design. Basically, fractal geometries are self-filling structures that can be scaled without increasing the overall size. This characteristic provides a chance for antenna designers to explore more new geometries suitable for small antenna design. Although that fractal antennas show many attractive advantages in antenna design, there are few studies on multiband fractal

antenna design especially on its applications to printed monopole antennas. Therefore, this is a field that needs to be further explored.

In the aspect of antenna modeling, due to the complexity of the fractal geometry, it is necessary to find an efficient way to aid the design of fractal-based antennas. Since fractals can be represented by either mathematical formulas or recursive functions [10], MATLAB[1] becomes a natural choice to calculate the fractals. Then, a macro script, which can be executed by most of the antenna simulation software, is written to create the fractal geometry for the purpose of antenna modeling. A simple presentation of this process is shown in Figure 4.

Figure 4: The general working flow of creating fractals for antenna modeling

1.2.2 *Antenna with Lumped Element*

Another technique that has been employed in the design of compact antenna is to introduce lumped elements such as chip inductors directly on the radiation element, which can effectively reduce the size of the antenna. This is a research topic that appeared recently and currently there is limited research work in this related field.

In [11], a compact multiband PIFA was achieved by connecting two parts of the antenna using a capacitor. By suitably selecting the value of the capacitor, the resonant frequency of the lower band was decreased by more than 30%. Similarly, in [12], one varactor was added between the rectangular patch and the ground plane in a coplanar antenna. Using this technique, the resonant frequencies of the coplanar antenna can be decreased and by changing the value of the capacitance through varying the applied voltage of the varactor, the coplanar antenna can be tuned to operate at different frequencies. In [13, 14], a chip inductor was embedded in the printed monopole antenna, which resulted in a decreased resonant length of the fundamental mode and a decrease of a higher resonant mode. Introducing either a capacitor or inductor into the antenna design, the size of the antenna structure can be reduced. However, the RF characteristics of the chip inductor, such as the equivalent inductance, vary with the frequency. As a result, to accurately predict the resonant frequencies of the antenna, it is important to have an appropriate simulation model for the chip inductor during the antenna modeling. The approach proposed in this thesis work is to simplify the equivalent circuit of the

1 MATLAB (**Ma**trix **Lab**oratory) is a numerical computing environment and fourth-generation programming language developed by MathWorks Inc.

chip inductor into the one shown in Figure 5, where the values of the series resistance $R(f)$ and inductance $L(f)$ vary with the frequencies.

Figure 5: The simplified circuit model of the chip inductor

If the antenna is designed to simultaneously resonate at multiple frequencies, to have a good simulation accuracy, it is important to make the antenna structure exhibit independent current paths for each resonant mode because in the simulation model, the values for the equivalent circuit structure of the chip inductor, or in other words, the values of the series resistance $R(f)$ and inductance $L(f)$, can only be calculated at one single frequency where the chip inductor is more determinant.

1.2.3 *Neutralizing Techniques in Compact Antenna Array Design*

To design a compact antenna array, it is important to seek an effective solution to reduce the distance between each antenna because a distance of half wavelength between each antenna is normally required in order to have a good level of isolation.

Several techniques have been proposed to increase the isolation between closely space antenna elements. For example, the use of electromagnetic band gap (EBG) structures on the substrate of the antennas has been studied [15]. Despite that the distance between two patch antennas can be reduced due to the surface wave suppressing from the EBGs, the overall size of the antenna array is still large as the EBG contains periodic structures, the number of which is critical in deciding the isolation level. Introducing defect ground system (DGS) on the ground plane can also suppress the surface wave propagation like EBGs whilst achieving a more compact size [16]. However, this technique requires making several slotted structures on the ground plane, which is not desirable for industry antenna design as the ground plane needs to be used to mount other components.

Recently, a new method named 'neutralization technique' has been proposed for two single-band planar inverted-F antennas (PIFAs) for mobile applications [17, 18]. The principle of this method is to introduce a shorting line to neutralize the current of the two antennas, which in turn increases their isolation. This technique can also be explained as adding a suspending line to reduce the coupling between two antennas [19, 20]. By doing so, there is no need of adding extra space for antenna design. This technique provides a practical solution to design a compact antenna array; however, so far, this method

has two limitations. Firstly, this technique has been employed only in the PIFA antenna design. Secondly and more importantly, this technique can only be applied to single band antenna arrays, yet there is increasing need to have a multi-frequency antenna array.

This technique is further studied in this thesis work and has been successfully applied to the design of a printed monopole antenna array. One major breakthrough that has been achieved is to introduce the reconfigurable concept into the neutralizing technique, which results in a dual band compact printed monopole antenna array with high isolation.

1.2.4 *Reconfigurable Techniques*

Reconfigurable antennas are predicted to be one of the best candidates for future high data rate wireless communication systems [21]. With the development of Microelectromechanical systems (MEMS) technologies, the fabrication of RF switches with good working performance become possible. Generally there are three methods to design an reconfigurable antenna [22]:

1. Total geometry morphing, which employs a large amount of switchable sub-elements to form the desired antenna structure
2. Matching network morphing, which modifies the structure of feed and impedance matching network
3. Smart geometry morphing, which only modifies some important parameters of the antenna

The smart geometry morphing, which uses the minimum number of switches, attracts most of the research interests. Work has been conducted in this area, including the use of PIN diodes or MEMS in designing reconfigurable dipoles, slot antennas and stacked patch antennas [23, 24, 25].

Another approach that can be used to design reconfigurable antennas is to introduce varactor, whose capacitance varies with applied voltage, into the antenna structure. One frequency reconfigurable coplanar antenna [12] and patch antenna [26] were designed by adding one varactor between the antenna and its ground plane. By changing the value of the capacitance, the resonant frequency of both antennas can be adjusted.

Materials that exhibit novel electromagnetic properties not found in nature are attracting much attention of the research community. Such structures, known as metamaterials, are designed to have properties and operate in ways that bulk materials cannot. One example of such microwave metamaterials are electromagnetic band-gap (EBG) structures. These structures are playing a vital role to improve the performance of microwave components and antennas. Many researchers are

using Metallic Electromagnetic Band Gap (MEBG) on antenna design. MEBG is composed by 2-D arrays of conducting elements immersed in the substrate. Generally, MEBG exhibits two unique characteristics: surface wave suppressing when used as EBG surface and in-phase reflection (90 degree to -90 degree) which can be used as an Artificial Magnetic Conductor (AMC) [27]. In some literature, the second characteristic is also mentioned as High Impedance Surface (HIS) [28].

Recently, researchers found that when using the AMC as a ground plane for one antenna, it can to some degree influence the original resonant frequency of the antenna. Therefore, the concept of using a reconfigurable AMC structure to design reconfigurable antennas has been studied [29, 30, 31]. Since EBG is a recent technology, improvements on present techniques for the design of microwave circuits and antennas are continuously being made. Great emphasis is presently being given to the design of multiband AMCs and the use of reconfigurable or active AMC as the ground plane of a multiband antenna, which is also addressed in this thesis.

1.3 AUTHOR'S CONTRIBUTIONS

The main contributions of this dissertation include:

- A method to use MATLAB to aid the modeling of the fractal antennas is proposed. This technique can be applied to most of the EM simulation software packages. A small software tool has been built in MATLAB by using the proposed method, with which several multiband printed fractal-based monopole antennas have been designed. These antennas have compact size and multi-frequency operation characteristics. With the combination of other antenna size reduction techniques such as meander line, the frequency ratio of the antenna can be better controlled.

- An equivalent simplified circuit model of the chip inductor, which is suitable to be introduced to the EM simulation software for antenna modeling, has been proposed. A methodology of designing multiband antenna with chip inductor is also developed. With the proposed method, the radiation performance of the antenna can be accurately predicted. Two electrically small monopole antennas for dual band WLAN application and one multiband printed monopole antenna that can support several commercial frequency bands, including GSM, UMTS, WLAN and WiMAX, were proposed.

- A novel method that introduces the reconfigurable concept to the neutralization technique is studied. It is demonstrated that compact printed monopole antenna arrays can be achieved by using the neutralization technique. By introducing two RF switches

to the neutralization line, the design of compact dual band antenna arrays with high isolation can be achieved.

- A reconfigurable coplanar antenna is designed by using an active AMC ground plane. The frequency reconfiguration of the antenna is achieved by adding RF switches to the AMC ground plane, which itself behaves also as one additional radiation elements similar to a stacked antenna structure. This provides a new approach to design reconfigurable multi-frequency antenna.

This research work has resulted several publications on international journals and conferences. The main publications are:

Journal Publications:

1. Qi Luo; J. R. Pereira and H.M. Salgado. Compact printed monopole antenna with chip inductor for WLAN. *IEEE Antennas and Wireless Propagation Letters*, 10:880-883, September 2011.

2. Q. Luo; J.R. Pereira and H.M. Salgado. Reconfigurable dual band C-shaped monopole antenna array with high isolation. *Electronics Letters*, 46(13):888-889, June 2010.

International Conferences:

1. Q. Luo; C. Quigley; J. Pereira and H. M Salgado. Inverted-L Antennas Array in a Wireless USB Dongle for MIMO Application. *In Proceedings of 6th European Conference on Antennas and Propagation (EuCAP)*, Prague, Czech Republic, March 2012.

2. Qi Luo; Jose Pereira and Henrique Salgado. Compact Printed C-shaped Monopole Antenna With Chip Inductor. In *Proceedings of IEEE International Symposium on Antennas and Propagation*, Washington,USA, July 2011.

3. Qi Luo; H. M. Salgado and J. R. Pereira. Compact Printed Monopole Antenna Array for Dual Band WLAN Application. In *Proceedings of International Conference on Computer as a Tool (EUROCON)*, Lisbon, Portugal, November 2011.

4. Q. Luo; J.R. Pereira and H.M. Salgado. Tunable Multiband Antenna With An Active Artificial Magnetic Conductor Ground Plane. In *Proceedings of European Microwave Conference (EuMC)*, Paris, France, October 2010.

5. Q. Luo; H.M. Salgado and J.R. Pereira. Printed C-shaped Monopole Antenna Array With High Isolation For MIMO Applications. In *Proceedings of IEEE Antennas and Propagation Society International Symposium*, Toronto, Canada, July 2010.

6. Q. Luo; H.M. Salgado and J.R. Pereira. Printed Fractal Monopole Antenna Array For WLAN. In *Proceedings of International Workshop on Antenna Technology (iWAT)*, Lisbon, Portugal, March 2010.

7. Q. Luo; J.R. Pereira and H. Salgado. Fractal Monopole Antenna For WLAN USB Dongle. In *Proceedings of Loughborough Antennas and Propagation Conference*, vol. 1, pp. 245-247, Loughborough, UK, November 2009.

8. Q. Luo; H. M. Salgado and J. R. Pereira. Fractal Monopole Antenna Design Using Minkowski Island Geometry. In *Proceedings of IEEE International Symposium on Antennas and Propagation*, Charleston, United States, June 2009.

National Conferences:

1. Qi Luo; Jose Pereira and Henrique Salgado. Inverted-L Antenna (ILA) Design using Fractal for WLAN USB Dongle. I*n Proceedings of Conference on Electronics, Telecommunications and Computers*, Lisbon, Portugal, November 2011.

1.4 THESIS OVERVIEW

This thesis introduces several antenna and antenna array miniaturization techniques. The antennas proposed in this work are mainly designed for the application in WLAN and personal mobile communications. This work is divided into three parts and the details of each part are outlined in the following sub-sections.

1.4.1 *Part 1: Numerical Methods in Electromagnetic*

An overview of the computational numerical methods is presented in Chapter 2. The basics of three important numerical techniques, Method of Moment (MoM), Finite-Difference Time-Domain (FDTD) and Finite Element Method (FEM), are introduced. These three techniques have been widely employed by many electromagnetic simulation software packages for the design of different types of antennas. Considering the advantages and disadvantages of the above three numerical techniques, the method-of-choice of this thesis work is FEM method, which is more suitable to the design of compact and electrically small antennas that normally have a complicated structure and narrow bandwidth. The main software that was used to simulate the antennas is Ansoft HFSS, which is a 3D EM simulator based on the FEM.

Although commercial software is available for antenna simulation, it is important to understand the theories of the numerical technique. In Chapter 2, the fundamental theory and mathematical derivation of FEM analysis including the domain discretization, interpolating

function and system matrix formulation are also presented. Two examples that use the FEM to solve the differential equations for two-dimensional problem in MATLAB are also demonstrated.

1.4.2 *Part 2: Compact Antenna and Antenna Array Design*

Two different techniques to design antennas of compact size are presented in Chapter 3, 4 and 5. In Chapter 3, several printed monopole antennas including one single feed fractal monopole antenna array using fractal geometries are introduced. These antennas are designed for dual band or triple band WLAN applications and two of them are made under the scenario of a USB dongle application. The detailed methodology considerations on how to use MATLAB to aid the design of fractals in Ansoft HFSS are also discussed in detail in this chapter. Three electrically small antennas with an embedded chip inductor are presented in Chapter 4 and 5. Each of these antennas has an electrically small size and promising radiation performance. The two antennas presented in Chapter 5 were designed for dual band WLAN communications whilst the one proposed in Chapter 6 is designed for multiband mobile communications including GSM (900/1800MHz), PCS (1900MHz), UMTS (2100MHz), WLAN (2.4/5.2GHz) and WiMAX (3.5GHz). A design guideline regarding the appropriate method to employ the chip inductor for multiband antenna design is presented in Chapter 4.

One single band compact printed monopole antenna array is presented in Chapter 6. The proposed antenna array has compact size and the distance between the two antenna elements is less than 1/10th of the wavelength whilst there is a good isolation between each antenna port. The proposed antenna array is designed for the WLAN 5.8 GHz USB dongle application. The technique used in the antenna array design is named "Neutralizing Techniques", which is a new methodology recently proposed for PIFA antenna array design [17].

1.4.3 *Part 3: Reconfigurable Antenna Design*

In Chapter 7, one coplanar antenna that can operate at four different frequency bands is achieved by using an active artificial magnetic conductor (AMC) as the ground plane. In this design, instead of adding them on the antenna element, the RF switches are mounted on the AMC ground plane. By changing the states of these switches, the reflection phase of the AMC can be altered, which in turn tunes the resonant frequency of the coplanar antenna. The novelty of this work lies on two aspects. Firstly, the frequency reconfigurability of the antenna is determined by the ground plane, which is located within a short distance below the antenna. Secondly, in this design, two useful frequency bands are contributed by the radiation from the AMC

unit cells, which is an innovative method to make a multi-frequency antenna.

One reconfigurable dual band compact monopole array is presented in Chapter 8. This antenna array contains two C-shaped monopoles with a shorting line, on which two RF switches were integrated, connecting the two antenna elements that are separated by a distance of $0.09\lambda_{2.4GHz}$. High isolation at 2.4 or 5.2 GHz bands can be achieved by changing the states of the RF switches. By introducing the concept of reconfigurability, it is demonstrated that one antenna array with two closely spaced antennas operating at WLAN dual frequency band with high isolation can be attained.

1.4.4 *Conclusions and Future Work*

Chapter 9 presents the conclusions of this thesis work as well as the future work that should be continually investigated in the scope of compact and electrically small multiband antenna and antenna array design.

Part I

NUMERICAL METHODS IN ELECTROMAGNETICS

2

NUMERICAL METHODS FOR ELECTROMAGNETIC COMPUTATION

2.1 INTRODUCTION

Nowadays, antenna design needs to employ numerical analysis to solve the complex electromagnetic wave propagation, radiation and scattering problems, which are not always analytically calculable. These numerical methods can be used to derive the closed form solution of Maxwell's equations by solving a large amount of integrations or differential equations. Thanks to the advances of the modern computer technologies, several commercial Electromagnetic (EM) simulators are available for antenna design. Generally speaking, there are three main numerical methods that have been widely implemented in the field of antenna simulation, namely Methods of Moments (MoM), Finite-Difference Time-Domain (FDTD) and Finite Element Method (FEM). The fundamental principles of these three popular computational electromagnetic methods, MoM, FDTD and FEM, are briefly introduced in the Section2.2, where some discussions about the advantages and disadvantages of each numerical method in the field of electrically small antenna simulation are also presented. More detailed discussion of the computational electromagnetic can be found at [32, 33, 34].

Since the antennas presented in this thesis work were analyzed by using Finite Element Method, it is important to understand the principles of this numerical method for the purpose of better antenna modeling, which is the main objective of Section2.3. This section gives a detailed introduction of the FEM analysis in the order of the four basic steps involved in a FEM analysis, namely domain discretization, interpolating function selection, system equations formulation and solution of the system equations. Implementation of FEM to solve one-and two-dimensional problems are presented with some examples that were solved with the aid of MATLAB. The discussion of the FEM analysis in the three-dimensional domain is not covered in this chapter due to the large computation complexity.

2.2 A BRIEF REVIEW OF NUMERICAL METHODS

2.2.1 *Methods of Moments*

Methods of Moments was first proposed by Harrington in 1968 [35]. This method makes use of Maxwell's equation in integration form

to formulate the electromagnetic problems in terms of unknown currents and calculates the coupling between the current elements based on the Helmholtz-Equations:

$$\triangle\Phi + k_0^2\Phi = -\frac{\rho}{\varepsilon_0} \tag{1}$$

$$\triangle\overrightarrow{A} + k_0^2\overrightarrow{A} = -\mu\overrightarrow{J} \tag{2}$$

$$k_0 = \omega\sqrt{\varepsilon_0\mu_0} \tag{3}$$

where Φ represents the electrical potential, k_0 is the free space wave number, ρ is the density of the electrical charge, $\overrightarrow{J}$ is the current vector, $\overrightarrow{A}$ is the magnetic vector potential, ε_0 and μ_0 is permittivity and permeability of the free space, respectively. Using the definition of potential functions, the $\overrightarrow{E}$ and $\overrightarrow{H}$ field can be calculated:

$$\overrightarrow{H} = \frac{1}{\mu}\nabla\times\overrightarrow{A} \tag{4}$$

$$\overrightarrow{E} = -j\omega\mu\overrightarrow{A} - \nabla\Phi \tag{5}$$

With the help of the general solutions of the Helmholtz-Equations, and after mathematical derivation the coupling between each current element can be represented in the following form:

$$U_k = \sum_{i=1}^{N} Z_{ki} I_i \tag{6}$$

or

$$\begin{pmatrix} Z_{11} & \cdots & Z_{1i} & \cdots & Z_{1N} \\ \vdots & \ddots & & & \vdots \\ Z_{k1} & & Z_{ki} & & Z_{kN} \\ \vdots & & & \ddots & \vdots \\ Z_{N1} & \cdots & Z_{Ni} & \cdots & Z_{NN} \end{pmatrix} \begin{pmatrix} I_1 \\ \vdots \\ I_k \\ \vdots \\ I_N \end{pmatrix} = \begin{pmatrix} U_1 \\ \vdots \\ U_k \\ \vdots \\ U_N \end{pmatrix} \tag{7}$$

where U_k is the given source voltage, Z_k is the coupling impedance matrix that describes the coupling relationship between each elements and I is the unknown currents needed to be solved. After solving these linear equations, the current distribution on the conductive materials can be calculated and then the other unknowns, for instance the radiation pattern or return loss of one antenna, can be calculated by post-processing.

The use of MoM technique usually leads to a dense matrix and the memory usage is proportional to the N^2, where N is number of nodes within the subject domain after discretization. The MoM method is suitable to solve Perfect Electrical Conductor (PEC) objects, where the

currents are only distributed on the surface. However, MoM will not be an efficient method to solve problems that involves dielectrics and layered structures in finite area. For example, in the software package Advanced Design System (ADS), during the antenna simulation it always considers an infinite substrate and ground plane and try to extract the current distribution on the substrate. This could lead to an inaccurate prediction when the antenna is designed on a substrate of relatively small size.

2.2.2 *Finite-Difference Time-Domain Method*

The FDTD method is based on the theory that the E-field and H-field are inter-related according the Maxwell's differential equations: the time derivative of the E-field is dependent on the curl of the H-field whilst the time derivative of the H-field is dependent on the curl of the E-field:

$$\nabla \times \overrightarrow{E} = -\mu \frac{\partial \overrightarrow{H}}{\partial t} - \sigma_M \overrightarrow{H} \tag{8}$$

$$\nabla \times \overrightarrow{H} = \varepsilon \frac{\partial \overrightarrow{E}}{\partial t} + \sigma_M \overrightarrow{E} \tag{9}$$

In the Cartesian coordinate system, the above two equations can be rewritten as the following six coupled partial differential equations:

$$\frac{\partial H_x}{\partial t} = \frac{1}{\mu_x}\left(\frac{\partial E_y}{\partial z} - \frac{\partial E_z}{\partial y} - \sigma_{Mx} H_x\right) \tag{10}$$

$$\frac{\partial H_y}{\partial t} = \frac{1}{\mu_y}\left(\frac{\partial E_z}{\partial x} - \frac{\partial E_x}{\partial z} - \sigma_{My} H_y\right) \tag{11}$$

$$\frac{\partial H_z}{\partial t} = \frac{1}{\mu_z}\left(\frac{\partial E_x}{\partial y} - \frac{\partial E_y}{\partial x} - \sigma_{Mz} H_z\right) \tag{12}$$

$$\frac{\partial E_x}{\partial t} = \frac{1}{\varepsilon_x}\left(\frac{\partial H_z}{\partial y} - \frac{\partial H_y}{\partial z} - \sigma_x E_x\right) \tag{13}$$

$$\frac{\partial E_y}{\partial t} = \frac{1}{\varepsilon_y}\left(\frac{\partial H_x}{\partial z} - \frac{\partial H_z}{\partial x} - \sigma_y E_y\right) \tag{14}$$

$$\frac{\partial E_z}{\partial t} = \frac{1}{\varepsilon_z}\left(\frac{\partial H_y}{\partial x} - \frac{\partial H_x}{\partial y} - \sigma_z E_z\right) \tag{15}$$

In 1966, Yee [36] introduces the concept of "Yee cell" (Figure 6), which discretizes the computational domain into a rectangular grid. Based on this concept, using the FDTD method the E- and H-field can be calculated step by step in a cyclic manner: the electric field is solved at a given instant in time, then the magnetic field is solved at the next instant in time, and the process is repeated over and over

again. This is the reason why this technique is classified as a time-domain method.

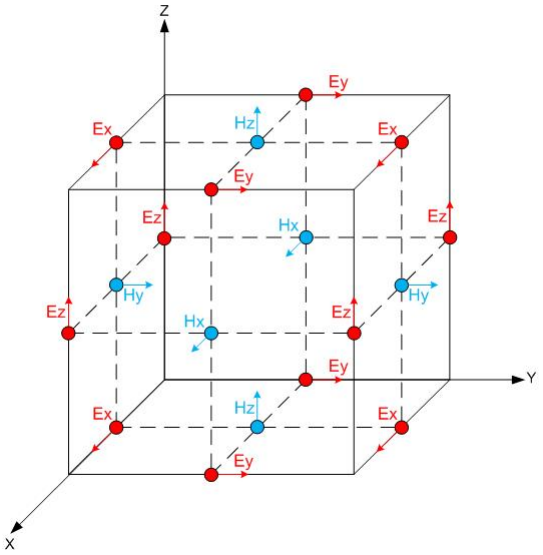

Figure 6: Yee's cell

Using FDTD method, although it takes many time steps to complete the calculation, it can cover a wide frequency range with a single simulation run. The advantages of FDTD methods are that it does not need to compute all the equations simultaneously, it is robust in numerical calculations and it can efficiently solve complex 3D transient problems. However, this technique is not adequate for narrow band antenna structures as in this case, each time step will be increased and it may require long simulation time to accomplish the calculation; moreover, the calculation may not be converged in the final solution, which can cause inaccurate results.

2.2.3 *Finite Element Method*

The FEM method is a powerful tool to find the approximate solution of partial differential equations. This technique was firstly introduced into the field of civil and aeronautical engineering to solve the complex structural analysis. Later, this method gained wide application in other fields including the electromagnetic engineering. This method starts with discretizing the whole domain into a number of sub-domains as shown in Figure 7 and then using an interpolating function, usually a polynomial of 1st or higher orders, to represent the unknowns inside these sub-domains. One example of expressing the unknown in the sub-domain using the interpolating function N is presented in Equation 16, where n is the number of nodes in the element, ϕ_j^e is the value of unknown at node j of element e. The Galerkin's Method and Ritz–Galerkin method are two popular meth-

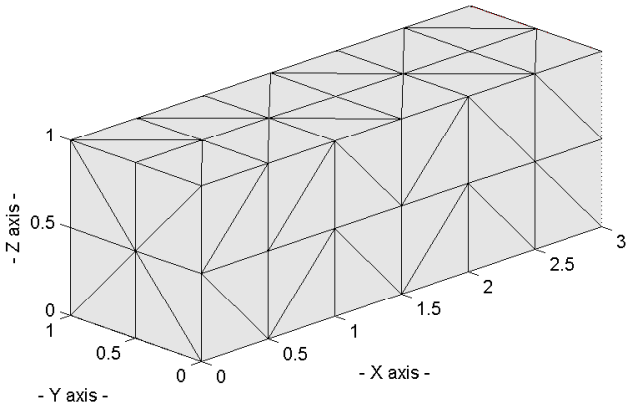

Figure 7: Discretizing a block with triangular meshing

ods that are always employed in the FEM analysis to define the interpolation functions.

$$y^{'} = \sum_{j=1}^{n} N_j^e \phi_j^e \tag{16}$$

With the global boundary conditions and the local continuous relationship between each node, linear equations can be formulated in the frequency domain after including all of these interpolating functions together to form a global system matrix having a form as presented in Equation 17, where K and u is related to the interpolating function in each sub-domain and b is related to the global boundary condition. After solving this global matrix system, the interpolating functions can be obtained and any unknowns can be calculated by applying the interpolating function in the sub-domain where it is contained.

$$\begin{bmatrix} K_{11}^{(1)} & K_{12}^{(1)} & & & & \\ K_{21}^{(1)} & \left(K_{22}^{(1)} + K_{11}^{(2)}\right) & K_{12}^{(2)} & & & \\ & K_{21}^{(2)} & \left(K_{22}^{(2)} + K_{12}^{(3)}\right) & & & \\ \cdots & \cdots & \ddots & \cdots & \cdots & \\ & & K_{21}^{(M-1)} & \left(K_{22}^{(M-1)} + K_{11}^{(M)}\right) & K_{12}^{(M)} & \\ & & & K_{21}^{(M)} & K_{22}^{(M)} & \end{bmatrix} \begin{Bmatrix} u_1^e \\ u_2^e \\ \vdots \\ u_n^e \end{Bmatrix} = \begin{Bmatrix} b_1^{(1)} \\ b_2^{(1)} + b_1^{(2)} \\ b_2^{(2)} + b_1^{(3)} \\ \vdots \\ b_2^{(M-1)} + b_1^{(M)} \\ b_2^{(M)} \end{Bmatrix} \tag{17}$$

FEM analysis is adequate for solving partial differential equations over complex domains, arbitrary shapes and closed space problems. However, the amount of computation is decided by the size of the overall computational domain, which is always discretized into many small size elements such as tetrahedral. Moreover, as this method is based on the frequency domain, the solution needs to be calculated for each frequency. Therefore, this method is not suitable to solve electrically large problems such as parabolic antennas.

More discussions about FEM analysis can be found at Chapter 3, which is a chapter dedicated to the introduction of FEM method.

2.2.4 *Numerical Methods for Electrically Small Antenna Design*

Electrically small antenna refers to an antenna whose maximum dimension is much smaller than its corresponding free space wavelength at its resonant frequency. To design an electrically small antenna, techniques that employ antenna of irregular shapes, substrate with non-homogeneous properties or multiple layers have been proposed. In this case, it is not suitable to simulate such structures using the MoM as the antenna is confined in limited space and has a non-planar structure or inhomogeneous substrate. An electrically small antenna usually has a narrow bandwidth since there is always a trade-off between the antenna size and operation bandwidth/efficiency/gain. The use of FDTD method to analyze such antennas would take a long sequence of time steps to complete because this method is based on the time domain, which is inversely proportional to the frequency domain. However, it is necessary to point out that several commercial EM simulation software packages have integrated other techniques to overcome such limits and improve the calculation efficiency as well as accuracy of the original methods. For instance, the fast multiple method (FMM) has been applied to accelerate the iterative solver of MoM and the Finite integration technique (FIT) has been developed to incorporate with the FDTD analysis.

Compared to the MoM and FDTD methods, FEM is naturally suitable to model antennas of compact size and complicated structure. The computation of FEM is carried out in frequency domain and the amount of equations only depends on the total amount of the mesh generated, which is proportional to the size of the domain needed to be solved. Moreover, FEM is capable of solving antenna of arbitrary shape or within an inhomogeneous media. The objective of this research is to investigate the techniques for multiband antenna miniaturization and the antennas designed in this thesis work will be of compact size or electrically small. Moreover, the shapes of the antennas will have complex geometry (e.g. fractal) and substrates of high permittivity might be used. Therefore, comparing the pros and cons of the above three numerical techniques, the method-of-choice of this thesis work layed on the FEM method. The main software chosen to simulate the antennas is Ansoft HFSS, which is a 3D EM simulator based on the FEM.

2.3 FINITE ELEMENT METHOD

2.3.1 *FEM Analysis*

The Finite Element Method (FEM) is a numerical technique to obtain approximate solution of partial differential equations and integral equations. It can be used to derive the accurate solutions for complex engineering problems such as aircraft and car structural problems. This method was proposed in 1940s and began to be employed in the field of airframe and structure analysis the 1950s. Nowadays, the FEM has been well established and widely used in various fields including mechanical, civil and aeronautical engineering as well as electromagnetic.

The finite element method is considered to be one of the best methods that can efficiently solve a wide variety of practical problems. The principle behind this method is to discretize the subject domain into smaller sub-domains, referred as the finite elements, and then use interpolating functions to approximate the unknowns inside them. These sub-domains contain certain amount of nodes depending on the employed discretization method. The triangular element is a typical choice for solving 2-D problems and the use of tetrahedral element is common for solving 3-D problems. The primary unknown will be solved inside these finite elements and the accuracy of the final solution depends on the order of the interpolation functions used, which may be polynomials with first or higher orders. In the last step, these functions will form a global matrix system with the internal relationships between the nodes and the values at the edges. After applying the global boundary conditions, the solutions can be obtained by solving this global matrix system of equations.

One of the main advantages of this method is that once the general mathematical model has been built, which is normally written in computer code due to the large computation effort required, it can be utilized to solve other similar problems by simply changing the input data (such as the coefficients of the differential equation) and applying suitable boundary conditions.

In the field of microwave and electromagnetics, the finite element method was introduced by Silvester in 1969 [37]. After that, there were a tremendous amount of researches that had been carried out and since 1970s, the finite element method started to be applied in the analysis and design of various antennas [38]. Generally speaking, there are four basic steps included in a finite element analysis [39]:

- Discretization or subdivision of the domain
- Selection of the interpolation function
- Formulation of the system equations

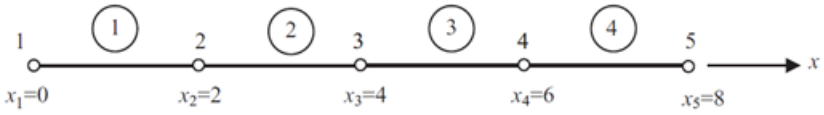

Figure 8: Linear discretization in one-dimensional domain

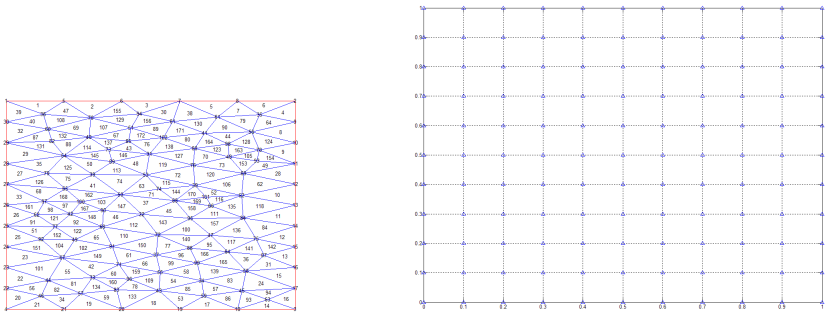

Figure 9: Triangular and Quadrilateral discretization in two-dimensional domain (Meshing were generated in MATLAB)

- Solution of the system equations

Each step will be briefly described in following subsections. Most of the theoretic analysis can be found in [39, 40]. Due to the complexity of the FEM analysis in 3D domain, this chapter focuses mainly on the application of the FEM analysis in 1D and 2D domains.

2.3.1.1 *Domain Discretization*

Discretizing the subject domain is the first step to perform the finite element analysis. This process is also referred as 'meshing' in some literature. Meshing is one of the most important steps in finite element analysis as it can determine the accuracy of the overall solution. Generally speaking, the finer the mesh is, the higher accuracy of the analysis can be reached; however, increasing the mesh always leads to a larger size of the final system matrix, which in turn requires higher computation memory and longer solution time.

In one-dimensional domain, the short line segments are usually employed to mesh the whole domain as shown in Figure 8 [40]. In the case of two-dimensional problem, typically triangular or quadrilateral elements are employed, which is shown in Figure 9. In the three-dimensional scenario, the domain is used to be divided by using tetrahedral elements (Figure 10 [40]).

One important criterion that can be used to measure the quality of the meshing is the discretization error. For irregular shapes, the quadrilateral or cubic elements always have larger discretization error compare to triangular or tetrahedral elements. This is the reason

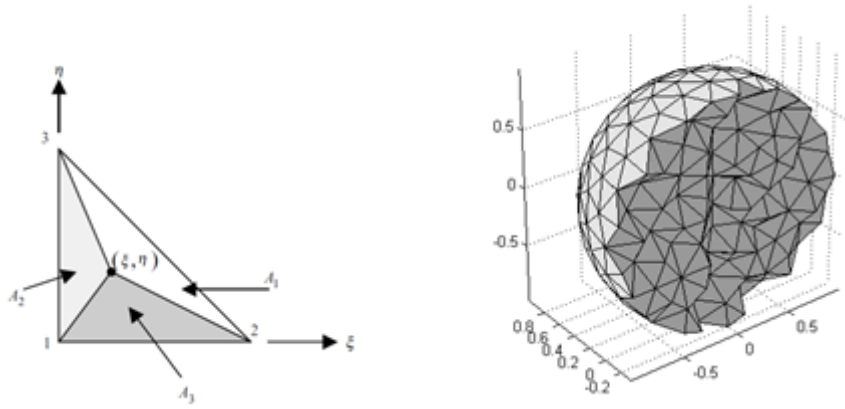

Figure 10: Tetrahedral discretization for object in three-dimensional domain

why in most of the commercial electromagnetic simulation software triangular and tetrahedral are employed. Figure 11 [40] shows the comparison of the discretization error incurred by the use of rectangular element and triangular element. It is obviously that when the domain has an irregular shape, it is difficult to describe it accurately using the rectangular element, which in turn could result in larger computational errors.

2.3.1.2 *Approximation Techniques*

After discretization, the unknowns in the sub-domain need to be solved by doing *weak formulations* to seek for the approximate solutions. Weak formulation is an important mathematical tool to solve problems such as partial differential equations by making use of linear algebra. The unknowns inside each finite element are represented by a set of interpolating functions, which need to be continuous within the element, at least once differentiable and should contain all the lower order terms. The interpolating function is usually selected to be a polynomial of first order for simple computation. This formulation is called the *weak formulation*. It is also possible to use polynomial of higher orders to make a *strong formulation*, which is more complicated and needs more computation time but it can provide more accurate solutions. Once the order of the polynomial is decided, the approximate solution, y' , for the unknown inside the element $\boldsymbol{e}$ can be expressed in the following form:

$$y^{'} = \sum_{j=1}^{n} N_j^e \phi_j^e \tag{18}$$

where n is the number of nodes in the element, ϕ_j^e is the value of ϕ, which is the unknown, at node j of this element. N_j^e is the interpolating function for node j inside element e, which is also known as the expansion or basis function. Function N_j^e, as shown in Equation 19, is

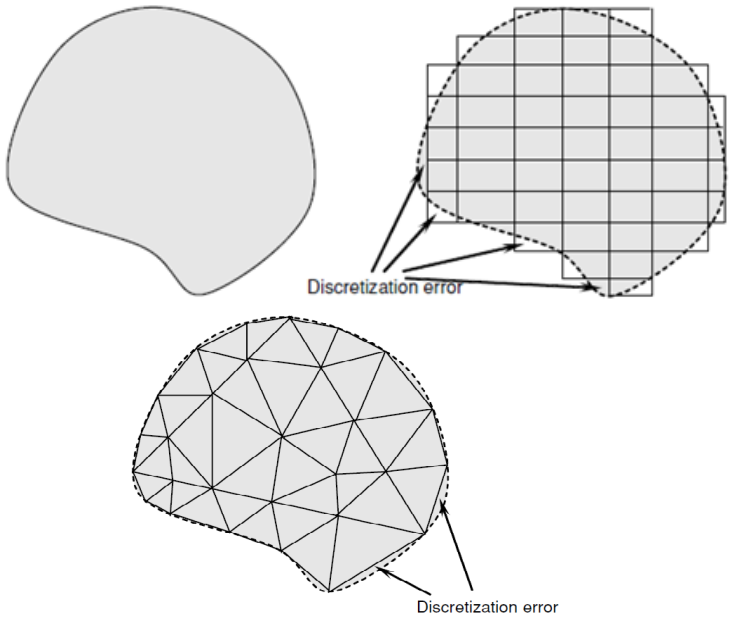

Figure 11: Discretization error caused by using rectangular or triangular elements

required to satisfy that it is only non-zero on the j^{th} node and at other nodes, its value equals to zero:

$$N_j = \begin{cases} 1 & at\ node\ j \\ 0 & at\ other\ nodes \end{cases} \tag{19}$$

The technique that is usually adopted to simplify the calculation is to transform the original coordinates to the natural coordinate, which has a fixed integration limit from -1 to +1. The advantage of using the natural coordinate is that when doing the integration during the weak formulation, at different elements the integration limits do not need to be changed. This can be advantageous when the integration is calculated by computer programing. In one dimensional domain, there are two nodes, x_1^e and x_2^e, for each element. Using the Formula 20, the original coordinate can be mapped to natural coordinates as shown in Figure 12 [40].

$$\xi = \frac{2(x - x_1^e)}{x_2^e - x_1^e} - 1 \tag{20}$$

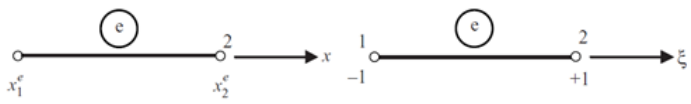

Figure 12: Transformation of the original coordinate to natural coordinate in 1D domain

Similarly, in the 2-D domain, the coordinates of triangular and quadrilateral elements can be mapped into a natural coordinate. For the purpose of easy calculation, normally the nodes of the 2D element are locally numbered in a counter-clockwise direction as depicted in Figure 13 and and 14 [40]. Then, for a triangular element, the coordinates transformation will be:

$$(\xi,\eta) = \begin{cases} \xi = \frac{x-x_1^e}{x_2^e-x_1^e}, & \eta = 0 \quad for\ Node\,1\ and\ Node\,2 \\ \eta = \frac{y-y_1^e}{y_2^e-y_1^e}, & \xi = 0 \quad for\ Node\,1\ and\ Node\,3 \end{cases} \tag{21}$$

Similarly, for quadrilateral element, the coordinates transformation will be:

$$(\xi,\eta) = \begin{cases} \xi = \frac{2(x-x_1^e)}{x_2^e-x_1^e} - 1, & \eta = -1 \quad for\ Node\,1\ and\ Node\,2 \\ \eta = \frac{2(y-y_1^e)}{y_2^e-y_1^e} - 1, & \xi = 1 \quad for\ Node\,3\ and\ Node\,4 \end{cases} \tag{22}$$

where x^e and y^e represent the coordinates of each node on the finite element.

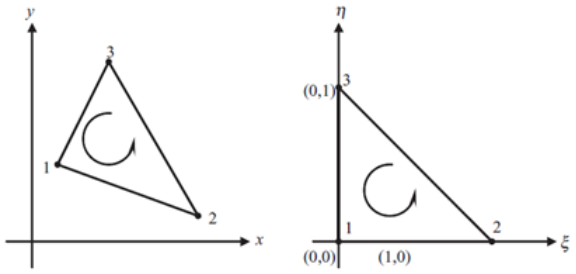

Figure 13: Transformation of the triangular element to natural coordinate

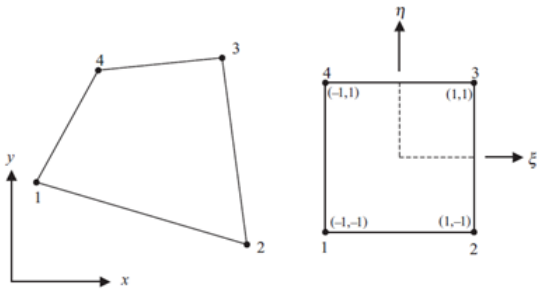

Figure 14: Transformation of the quadrilateral element to natural coordinate

Therefore, after the coordinate transformation, the interpolating function N_j^e in Equation 18 will be transformed to $N_j^e(\xi)$ for one-dimensional problems and $N_j^e(\xi,\eta)$ for two dimensional problems. Then it is important to choose a suitable interpolation function to derive the approximate solution for the unknowns with good accuracy.

In FEM analysis, the *Galerkin's Method* is always employed to define the interpolation functions. Following the Galerkin's Method and using the polynomials of the 1st order, for one-dimensional problems the general form of the interpolating function $N(\xi)$ can be expressed as:

$$N(\xi) = C(1-\xi)(1+\xi) \tag{23}$$

While for two-dimensional problems, in the case of the triangular element, the interpolating function $N(\xi,\eta)$ can be expressed as:

$$N(\xi,\eta) = C_1 + C_2\xi + C_3\eta \tag{24}$$

In the case of quadrilateral element, $N(\xi,\eta)$ is:

$$N(\xi,\eta) = C_1 + C_2\xi + C_3\eta + C_4\xi\eta \tag{25}$$

where the C_n are constants. Moreover, similar to Equation 19, the interpolation function should also satisfy:

$$N_j^e(\xi,\eta) = \begin{cases} 1 & \textit{at node } j \\ 0 & \textit{at all other nodes} \end{cases} \tag{26}$$

and

$$\sum_{j=1}^{n} N_j^e = 1 \tag{27}$$

Given the general form of and the conditions that it needs to satisfy, the interpolating function can be calculated. Assume that it is required to find the solution for Equation 28 within the finite element Ω_e:

$$y = f(x) \tag{28}$$

Following Equation 18 , the approximately solution by using the interpolating N^e is:

$$y^{'} = \sum_{j=1}^{n} N_j^e(\xi)\phi_j^e \tag{29}$$

Then, the weighted residual for this element is:

$$r_i^e = \int_{\Omega_e} [y^{'} - f(x)]d\Omega^e \tag{30}$$

Ideally the residual r_i^e should equal to zero, which represents an accurate approximation of the real solution. After finding the expression for the weighted residual, the system equation is formulated, which will be discussed in the next section.

2.3.1.3 *System Equation Formulation*

The system equation is formed based on the expression of the weighted residual given in Equation 30. The integration by parts is applied to make the equation of the weighted residual has a general form of Equation 32:

$$\int_a^b UdV = UV\,|_a^b - \int_a^b VdU \tag{31}$$

$$\begin{Bmatrix} r_1^e \\ r_2^e \\ \vdots \\ r_n^e \end{Bmatrix} = \begin{bmatrix} K_{11}^e & K_{12}^e & \dots & K_{1n}^e \\ K_{21}^e & K_{22}^e & \dots & K_{2n}^e \\ \vdots & \vdots & \ddots & \vdots \\ K_{n1}^e & K_{n2}^e & \cdots & K_{nn}^e \end{bmatrix} \begin{Bmatrix} u_1^e \\ u_2^e \\ \vdots \\ u_n^e \end{Bmatrix} - \begin{Bmatrix} b_1^e \\ b_2^e \\ \vdots \\ b_n^e \end{Bmatrix} \tag{32}$$

where n is the number of nodes in the finite element, u and K are derived from the interpolating function N; b is constituted by unknowns from integration by parts and constants from applying the boundary conditions. Equation 32 can be rewritten in a more compact form as:

$$[r^e] = [K^e]\,[U^e] - [b^e] \tag{33}$$

Then, the objective is to minimize the residual r_i^e; therefore, the interpolating functions will be solved by equaling the residual to zero. Then, the Equation 33 becomes:

$$[K^e]\,[U^e] = [b^e] \tag{34}$$

Assume that the subject domain has been meshed into M elements, Equation 33 can then be expanded into a global matrix by summation over each element:

$$\sum_{e=1}^{M} [r^e] = \sum_{e=1}^{M} \left([K^e]\,[U^e] - [b^e]\right) \tag{35}$$

Similarly, by setting $\sum_{e=1}^{M} [r^e]$ to a zero vector results:

$$\sum_{e=1}^{M} \left([K^e]\,[U^e] - [b^e]\right) = 0 \tag{36}$$

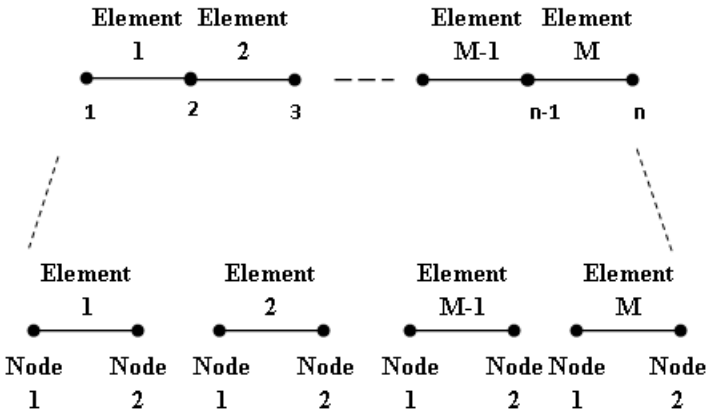

Figure 15: The local relationship of the nodes in 1-D domain

In the one dimensional domain, the expanded global matrix has the form of:

$$\begin{bmatrix} K_{11}^{(1)} & K_{12}^{(1)} & & & \\ K_{21}^{(1)} & \left(K_{22}^{(1)}+K_{11}^{(2)}\right) & K_{12}^{(2)} & & \\ & K_{21}^{(2)} & \left(K_{22}^{(2)}+K_{12}^{(3)}\right) & & \\ \cdots & \cdots & \ddots & \cdots & \cdots \\ & & K_{21}^{(M-1)} & \left(K_{22}^{(M-1)}+K_{11}^{(M)}\right) & K_{12}^{(M)} \\ & & & K_{21}^{(M)} & K_{22}^{(M)} \end{bmatrix} \begin{Bmatrix} u_1^e \\ u_2^e \\ \vdots \\ u_n^e \end{Bmatrix} = \begin{Bmatrix} b_1^{(1)} \\ b_2^{(1)}+b_1^{(2)} \\ b_2^{(2)}+b_1^{(3)} \\ \vdots \\ b_2^{(M-1)}+b_1^{(M)} \\ b_2^{(M)} \end{Bmatrix} \tag{37}$$

In the 2D domain, the expanded global matrix has a similar form as the one shown in Equation 37 except that there are more nodes in each finite element. Normally, it is preferred to rewrite Equation 37 to have a general simplified form as:

$$[K]\{U\} = \{b\} \tag{38}$$

To solve the system equation shown in Equation 38, the local relationships between the nodes need to be applied. For example, in a one-dimensional domain that uses linear elements as shown in Figure 15, it has to satisfy the local continuity equation:

$$N_2^{e(j)} = N_1^{e(j+1)} \tag{39}$$

In a two-dimensional domain that uses triangular elements as presented in Figure 16 [40], in order to reach consistent solution, the following local conditions have to be satisfied:

$$n_x^{e1} = -n_x^{e2} \tag{40}$$

$$n_y^{e1} = -n_y^{e2} \tag{41}$$

$$N_1^{e1} = N_1^{e2} \tag{42}$$

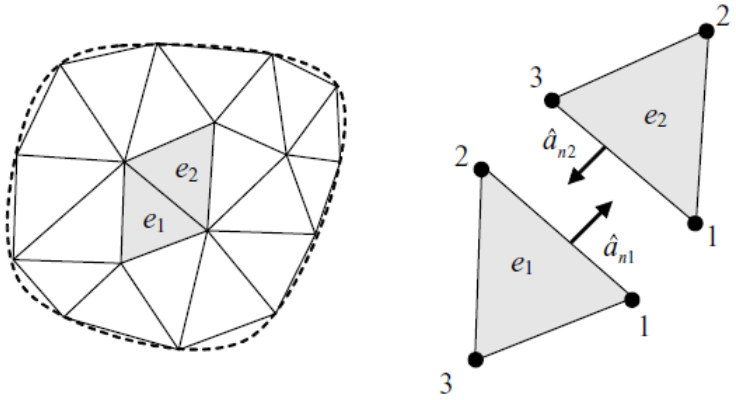

Figure 16: The continuous condition of the domain using triangular finite element

$$N_2^{e1} = N_3^{e2} \tag{43}$$

After applying these local conditions as well as the global boundary conditions, the system of equation can be solved. Normally the system equations are required to be solved with aid of the computer programs as it usually consists of a large amount of linear equations for a single frequency. The size of the global system equation is determined by the number of nodes and elements inside the subject domain. This is the reason why large computation time and computer memory are required when solving an electrically large antenna using the FEM technique.

2.3.2 *Using FEM in 1D and 2D domain*

In this section, the general solutions of several common differential equations solved by using FEM technique will be presented. In one dimensional domain, with the general solution the calculation is much more straightforward than in the two dimensional domain. Hence, in this section, for the 2D domain problem, after introducing the general solution of the differential equations, two examples of using MATLAB to solve EM problems based on the FEM technique are given.

2.3.2.1 *One-dimensional Problem using FEM*

Assume the differential Equation 44 needs to be solved in one dimensional domain and its domain has been discretized into M linear elements as shown in Figure 17.

$$-\frac{d}{dx}\left(\alpha\frac{d\Phi}{dx}\right)+\beta\Phi = f \tag{44}$$

where Φ is the unknown function, α and β are known parameters. The unknown function Φ inside each finite element can be represented by using Equation 18 and can be written as:

$$\Phi^e(x) = \sum_{j=1}^{2} N_j^e(x)\Phi_j^e \tag{45}$$

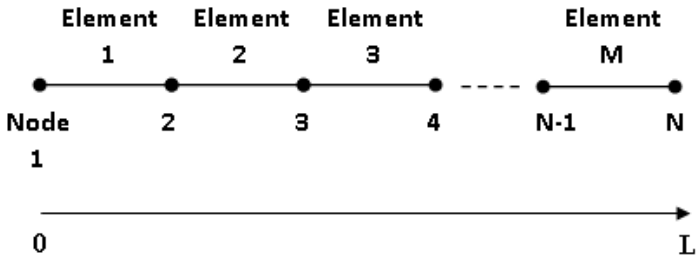

Figure 17: A mesh with M linear elements in one-dimensional domain

By letting the interpolating function N^e have the general form given by Equation 23 and apply the condition presented in Equation 26, the N^e can be found to be:

$$N_1^e(x) = \frac{x_2^e - x}{l^e} \tag{46}$$

$$N_2^e(x) = \frac{x - x_1^e}{l^e} \tag{47}$$

where l^e is the length of each segment:

$$l^e = x_2^e - x_1^e \tag{48}$$

After applying the Galerkin's Method, the weighted residual can be derived to have the following form [39]:

$$\{R^e\} = [K^e]\{\Phi^e\} - \{b^e\} - \{g^e\} \tag{49}$$

where:

$$K_{ij}^e = \int_{x_1^e}^{x_2^e} \left(\alpha \frac{dN_i^e}{dx}\frac{dN_j^e}{dx} + \beta N_i^e N_j^e \right) dx \tag{50}$$

$$b_i^e = \int_{x_1^e}^{x_2^e} N_i^e f \, dx \tag{51}$$

$$g_i^e = \alpha N_i^e \frac{d\Phi}{dx} \Big|_{x=x_2^e} - \alpha N_i^e \frac{d\Phi}{dx} \Big|_{x=x_1^e} \tag{52}$$

Let $\{R^e\} = 0$ can lead to the general solution of a one-dimensional problem that needs to solve the 1st order differential equation shown

in Equation 44. Following the general rules of the FEM technique, [41] gives the general solution for the following second order differential equation in the one-dimensional domain:

$$a\frac{d^2u}{dx^2} + b\frac{du}{dx} + cu = f(x) \tag{53}$$

where a, b, c are given constants. Using the linear shape function, [41] derived that:

$$K^e = \int_{x_i}^{x_{i+1}} \left(-a \begin{Bmatrix} H_1' \\ H_2' \end{Bmatrix} \begin{bmatrix} H_1' & H_2' \end{bmatrix} + b \begin{Bmatrix} H_1' \\ H_2' \end{Bmatrix} \begin{bmatrix} H_1' & H_2' \end{bmatrix} + c \begin{Bmatrix} H_1' \\ H_2' \end{Bmatrix} \begin{bmatrix} H_1' & H_2' \end{bmatrix} \right) dx \tag{54}$$

$$F_e = \{b^e\} + \{g^e\} = \frac{l_e}{2} \begin{Bmatrix} H_1 \\ H_2 \end{Bmatrix} dx \tag{55}$$

where:

$$H_1(x) = \frac{x_{i+1} - x}{l^e} \tag{56}$$

$$H_2(x) = \frac{x - x_i}{l^e} \tag{57}$$

The expression of K^e can be calculated by evaluating the integration with the linear interpolating function given in Equation 23. Since in one-dimensional domain, the domain is discretized into linear segment with only two nodes, so K^e can be further derived to have a more simple form as:

$$K^e = -\frac{a}{l^e} \begin{bmatrix} 1 & -1 \\ -1 & 1 \end{bmatrix} + \frac{b}{2} \begin{bmatrix} -1 & 1 \\ -1 & 1 \end{bmatrix} + \frac{c\,l^e}{6} \begin{bmatrix} 2 & 1 \\ 1 & 2 \end{bmatrix} \tag{58}$$

Then, the global system matrix can be formed according to the Equation 37 and the solution can be found by taking into consideration of the global boundary conditions of the domain and the local relationship of the nodes as presented in Equation 39.

2.3.2.2 *Two-Dimensional Problem using FEM*

In the two-dimensional domain, assume that the following differential equation needs to be solved:

$$-\frac{\partial}{\partial x}\left(\alpha_x \frac{\partial \Phi}{\partial x}\right) - \frac{\partial}{\partial y}\left(\alpha_y \frac{\partial \Phi}{\partial y}\right) + \beta\Phi = f \tag{59}$$

where Φ is the unknown function, α_x, α_y and β are constant, f is a function of x and y. In two dimensional domain, the derivation of the general solution is much more complicated than in one-dimensional

domain as the increasing of nodes and unknown variables. The general solution for the equation shown in Equation 59 is given in [39]. Firstly, the unknown function is approximated by using the interpolating functions:

$$\Phi^e(x,y) = \sum_{j=1}^{3} N_j^e(x,y)\Phi_j^e \tag{60}$$

In [39], the domain is discretized using triangular elements. Using the weak formulation and the general form (Equation 24) as well as the characteristics of a interpolation function given in Equation 26 and 27, the interpolating function N^e can be found to be:

$$N_j^e(x,y) = \frac{1}{2\Delta^e}(a_j^e + b_j^e x + c_j^e y) \tag{61}$$

where:

$$a_1^e = x_2^e y_3^e - y_2^e x_3^e \tag{62}$$

$$b_1^e = y_2^e - y_3^e \tag{63}$$

$$c_1^e = x_3^e - x_2^e \tag{64}$$

$$a_2^e = x_3^e y_1^e - y_3^e x_1^e \tag{65}$$

$$b_2^e = y_3^e - y_1^e \tag{66}$$

$$c_2^e = x_1^e - x_3^e \tag{67}$$

$$a_3^e = x_1^e y_2^e - y_1^e x_2^e \tag{68}$$

$$b_3^e = y_1^e - y_2^e \tag{69}$$

$$c_3^e = x_2^e - x_1^e \tag{70}$$

$$\Delta^e = \frac{1}{2}\begin{bmatrix} 1 & x_1^e & y_1^e \\ 1 & x_2^e & y_2^e \\ 1 & x_3^e & y_3^e \end{bmatrix} \tag{71}$$

The weighted residual can be written in the following form:

$$\{R^e\} = [K^e]\{\Phi^e\} - \{b^e\} - \{g^e\} \tag{72}$$

where:

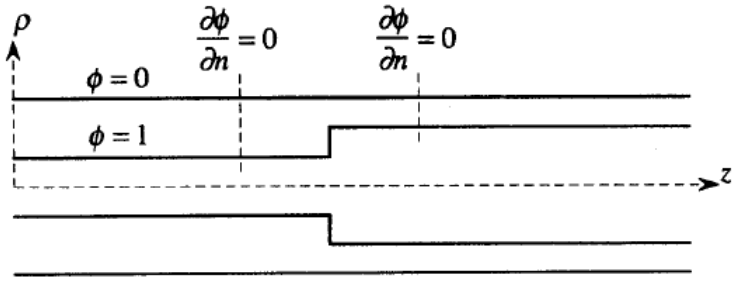

Figure 18: The cross section of the joined coaxial waveguide at ρz plane

$$K_{ij}^e = \iint_{\Omega_e} \left(\alpha_x \frac{\partial N_i^e}{\partial x} \frac{\partial N_j^e}{\partial x} + \alpha_y \frac{\partial N_i^e}{\partial y} \frac{\partial N_j^e}{\partial y} + \beta N_i^e N_j^e \right) dxdy \tag{73}$$

$$b_i^e = \iint_{\Omega_e} f N_i^e dxdy \tag{74}$$

$$g_i^e = \oint_{\Gamma^e} N_i^e D \cdot \hat{n}^e d\Gamma \tag{75}$$

$$D = \left(\alpha_x \frac{\partial \Phi}{\partial x} \hat{x} + \alpha_y \frac{\partial \Phi}{\partial y} \hat{y} \right) \tag{76}$$

Equations 61 to 76 form the general solutions of the differential equations using FEM analysis in two-dimensional domain. In the next section, this general solution will be applied to solve two EM problems with the aid of programming in MATLAB.

2.3.2.3 *Examples of Using FEM to solve 2D Problems*

Based on the analysis presented in the previous sections, the differential equations have the form as Equation 44, 53 or 59 can be solved by using the FEM technique. Since that the solution for 1D problem is straightforward, this section only focuses on using FEM to solve problems in 2D domain.

One example of using FEM to solve the differential equations in two dimensional domain is to solve the Poisson equation in a waveguide. Assume two coaxial waveguides, which have different inner radius, are joined together as shown in Figure 18. This problem was addressed in [39] and is solved here by implementation of FEM in MATLAB. Since the geometry is symmetric with the z axis, so the potential satisfies the Poisson Equation (Equation 77) with the boundary condition shown in Figure 19. Since the Poisson equation has a similar form as the one given in Equation 59, the general solution derived in [39] can be applied.

$$-\frac{1}{\rho}\frac{\partial}{\partial \rho}\left(\epsilon_r \rho \frac{\partial \Phi}{\partial \rho}\right) - \frac{\partial}{\partial z}\left(\epsilon_r \frac{\partial \Phi}{\partial z}\right) = \frac{\rho_c}{\epsilon_0} \tag{77}$$

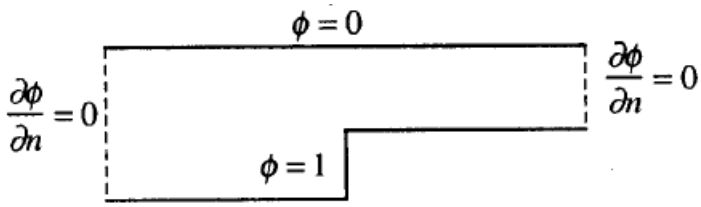

Figure 19: The subject domain with boundary conditions

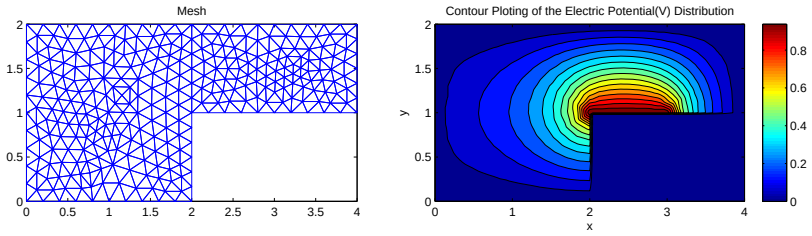

Figure 20: The mesh of the domain and the calculated electric potential distribution. The unknowns inside the subject domain is meshed and solved in MATLAB

Firstly the subject domain shown in Figure 19 is divided using the triangular mesh (see Figure 20). Then, by adopting the general solutions given by Equation 60 and 73, after forming the global system matrix the values of the unknowns on each node can be calculated and the field inside the coaxial cable is evaluated by using the interpolating function in its corresponding element. Figure 20 shows diagrams of the meshing of the waveguide with the triangular element and the calculated electric potential distribution. A simple Pseudocode that briefly describes the FEM programming is given in Figure 21.

It is also important to emphasize that once the computer code has been developed, the same code can be utilized to solve other differential equations just by simply changing the input parameters and adding relevant boundary conditions. For example, the electric potential inside a box with metallic walls as the one shown in Figure 22 can be calculated by solving the Laplace's equation:

$$\frac{\partial^2 V}{\partial x^2} + \frac{\partial^2 V}{\partial y^2} = 0 \tag{78}$$

This differential equation can also be associated to the Equation 59, which has been used to derive the general solutions in 2D domain, by comparing the coefficient of each unknown variables (x and y). This problem is solved by following the same procedure described previously and using the same code developed in MATLAB. Figure 23 presents the calculated electric potential distribution inside the metallic box and its corresponding meshing, which has 306 nodes

CREATE the shape of the domain in PDETool
GENERATE Mesh (default: triangular element)
EXPORT mesh with nodes number, nodes coordinate and element number
FUNCTION (mesh)
READ mesh
DEFINE global boundary
FOR 1 to number of nodes
Create nodes connectivity information
FOR 1 to number of elements
Create interpolating function
Create System Matrix
SOLVE global matrix
END OF FUNCTION
FOR 1 to number of interpolating points
Calculate the unknowns within the solved interpolating functions
PLOT contour figure

Figure 21: Pseudo-code of the FEM programming in MATLAB

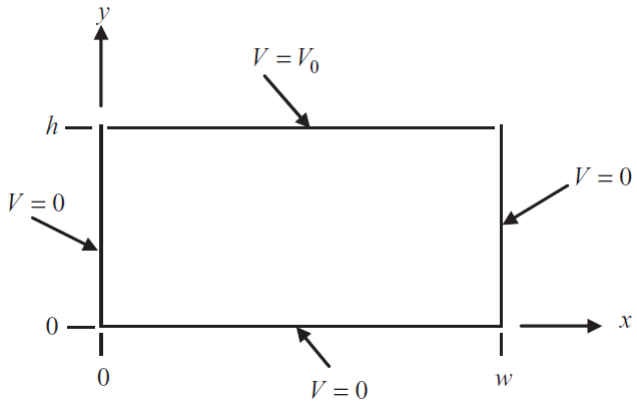

Figure 22: The rectangular box with metallic walls

and 548 triangles. In this problem, it it assumed that the rectangular box has a dimension of $5_{cm} \times 10_{cm}$ and the $V_0 = 1$.

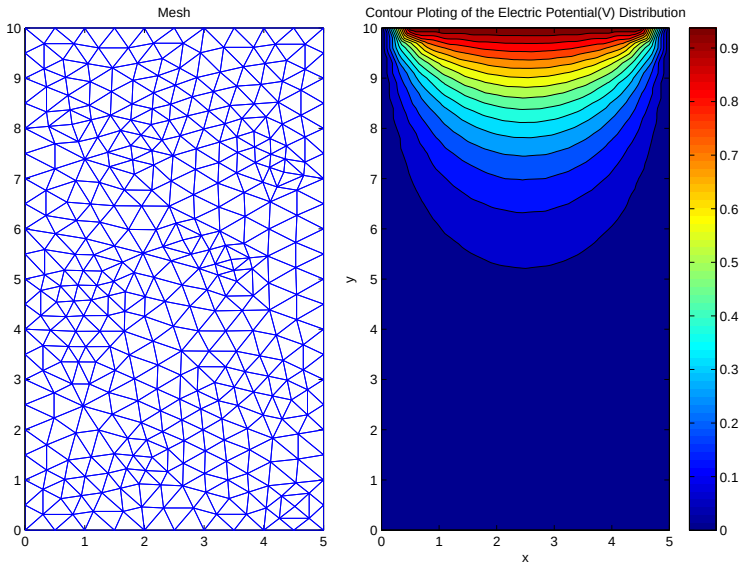

Figure 23: The plot of the mesh of the metallic box and the calculated electric potential distribution by using FEM

2.3.3 *Summary of the Chapter*

In this chapter, three main numerical methods include MoM, FDTD and FEM have been briefly reviewed. These three methods are based on different principles and each of them has their own advantages in solving different numerical problems in the field of antenna design. For instance, MoM is suitable for simulating metallic structures such as wired antenna; FDTD is adequate for calculating wide band antenna and FEM is good candidate to solve compact antenna structure with complex shape or multiple layers. These techniques have been implemented in different commercial electromagnetic simulation software packages and widely used in the field of antenna design. There are continuous studies on improving these methods by integrating other computational methods with the original ones. Considering the pros and cons of each method in the aspect of compact and electrically small antenna design, the FEM is chosen to be used in this study.

The mathematical foundations of the FEM analysis in one- and two-dimensional domains are presented. The general solutions for some typical partial differential equations have been derived. Using these general formulas, MATLAB codes have been developed to use the FEM techniques to solve the field distribution for a joined coaxial waveguide and a metallic box. From these two examples, it is shown that FEM is a very efficient method to solve electromagnetic prob-

lems that involves differential or partial differential equations. The computation method, which is usually written in computer code, can always be re-used to solve other similar problems as presented in the two examples.

Regarding to the use of FEM in antenna design, as the large complexity of the mathematical analysis due to the fact that the antennas are required to be modeled in 3D domain and it is also critical to employ suitable model of the antenna excitation, this subject is not addressed in this thesis work. Generally, commercial numerical simulation software is required to aid the antenna design. In the rest of this thesis, all of the antennas are designed and simulated in Ansoft HFSS.

Part II

COMPACT ANTENNA AND ANTENNA ARRAY DESIGN

3

FRACTAL ANTENNA DESIGN

3.1 INTRODUCTION

This chapter presents the design of compact printed monopole antennas using fractal techniques. The objective of this study is to utilize the space filling characteristic of the fractals to reduce the size of a monopole antenna whilst maintain its good radiation performance. Moreover, it also aims to make such compact antennas operate at multiple frequency bands of interests.

This chapter is organized as follows. Firstly the basics of fractals and the use of mathematical methods to generate fractal geometries are introduced in Section 3.2. Then, a methodology that utilizes MATLAB to aid the modeling of fractals in EM simulation tool, is demonstrated in Section 3.3. With the help of these developed MATLAB functions, several fractal-based multiband printed monopole antennas have been proposed. Section 3.4 introduces two multiband fractal monopoles using Minkowski Island geometry. Section 3.5 and 3.6 present two fractal inspired antennas for WLAN USB dongle application. One single feed fractal monopole antenna array, which exhibits higher directivity as a result of employing two identical fractal elements, is demonstrated in Section 3.7. Section 3.8 is a brief summary of this chapter.

3.2 BASICS OF FRACTAL GEOMETRY

In 1975, Mandelbrot coined the word "fractal" from the Latin word 'fractus' to label objects or shapes that have similar properties at all levels of magnification or across all times. Mandelbrot defined fractal as:

> "A fractal is by definition a set for which the Hausdorff-Besicovitch dimension strictly exceeds the topological dimension" [42].

The Hausdorff-Besicovitch dimension, which is also referred as Hausdorff dimension in some literature, is one of the most important methods to define the dimension of a fractal geometry. The dimension of a fractal geometry is greater than one but smaller than two and cannot be expressed as an integer. In this case, it is required to use the Hausdorff dimension to describe it. For a fractal F, its Hausdorff dimension is defined as [43]:

$$dim_H F = inf\{ s \geqslant 0 : H^s(F) = 0 \} = sup\{ s : H^s(F) = \infty \} \quad (79)$$

where i*nfinum* infA is the greatest number m such that $m \leq x$ for all x in A or is $-\infty$, *suprenum* supA is the least number m such that $x \leq m$ for every x in A or is ∞. $dim_H F$ is the Hausdorff dimension of F, s is a non negative number and $H^s(F)$ is defined as:

$$H^s(F) = \lim_{\delta \to 0} H^s_\delta(F) \quad (80)$$

where

$$H^s_\delta(F) = inf\left\{ \sum_{i=1}^{\infty} |U_i|^s : \{U_i\} \text{ is a } \delta - \text{cover of } F \right\} \quad (81)$$

In Equation 81, $\{U_i\}$ is a countable collection of sets of diameter at most δ that cover F. The dimension of F, $dim_H F$, should satisfy:

$$H^s(F) = \begin{cases} \infty & \text{if } 0 \leq s < dim_H F \\ 0 & \text{if } s > dim_H F \end{cases} \quad (82)$$

Hausdorff dimension is abstract and difficult to calculate in an intuitive way; as a result, there are other methods including Packing Measure, Box-counting and Self-similarity method that can be used to measure the dimension of fractals. One of the most used methods is Self-similarity method, which is an intuitive way to calculate the dimension of fractals that can be generated by self-repeating. It gives a good approximation to the Hausdorff dimension and the definition of self-similarity dimension is [10]:

$$M([\alpha]) = (diam[\alpha])^s \quad (83)$$

where M is the number of self-similar elements and s is the dimension. *diam* is the maximum diameter of this fractal, which equals the magnification factor of the fractal. Therefore, the dimension s can be calculated by doing a Log algorithm at both sides:

$$s = \frac{\log M([\alpha])}{\log diam[\alpha]} \quad (84)$$

Take the *Koch Curve* in Figure 24 as an example. For the *Koch Curve* of the second iteration, there are 4 identical line segments, which corresponds to $M([\alpha]) = 4$. Each of them is $1/3$ of the size of the initial line segment, so the magnification is 3, which means that $diam[\alpha] = 3$. Then, the dimension of the 2nd iteration *Koch Curve* is:

$$s = \frac{\log M([\alpha])}{\log diam[\alpha]} = \frac{\log 4}{\log 3} = 1.26$$

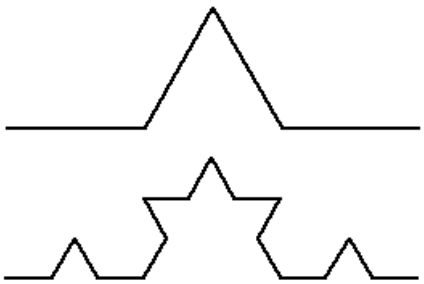

Figure 24: The first two iterations of the Koch Curve

Since a fractal is a self-affinity geometry that has repeating patterns, iteration methods can be used to mathematically create such geometries. Generally, there are three types of iterations that can be adopted to create fractal geometries:

- Generator Iteration
- Iterated Function System (IFS) Iteration
- Formula Iteration

Generator Iteration creates fractals by repeatedly substituting certain geometric shapes with other shapes. A pre-defined generator replaces certain part of the initial structure at each iteration. For example, some simple fractal geometries such as *middle third Cantor set*, can be realized by repeatedly cutting the middle line segment as shown in Figure 25.

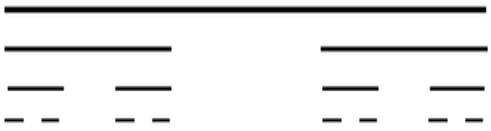

Figure 25: The structure of Cantor set

Iterated Function System (IFS) is a finite family of contractions $S = \{S_1, S_2, \ldots, S_m\}$, where S_m is a contraction that transforms sets into geometrically similar sets with probability $P = \{P_1, P_2, \ldots, P_m\}$. P_i is the relative weight for each contraction S_i and P_i needs to satisfy [44]:

$$\sum_{i=1}^{n} P_i = 1 \tag{85}$$

A unique fractal can be determined by one IFS. The transformation includes several functions such as rotation, move and reflection. Therefore, it can be seen that Generator Iteration is actually the simplest scenario of an IFS transformation with $S_1 = S_2 = \cdots = S_m$ and

uniform probability distribution. With an nonuniform distribution of the probability set P, some 'irregular' shapes can be defined such as the one shows in Figure 26 [43]. In some literature, these structures are referred as 'randomized fractal' with statistical self-similarity.

Formula iteration uses infinite summation of one mathematical expression to create a fractal structure. It usually leads to an non-smooth curve due to the infinity summation. Figure 27 [43] shows one fractal example generated using the following formula:

$$f(t) = \sum_{k=0}^{\infty} (\frac{3}{2})^{-k/2} sin((\frac{3}{2})^{-k/2} t) \tag{86}$$

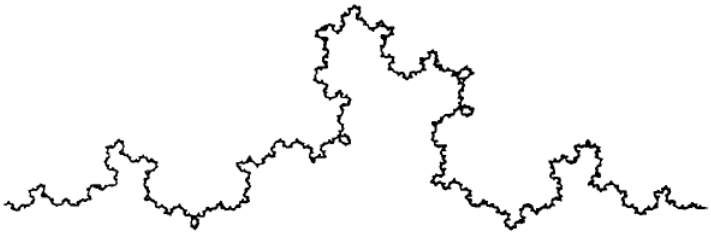

Figure 26: A random version of the Koch Curve

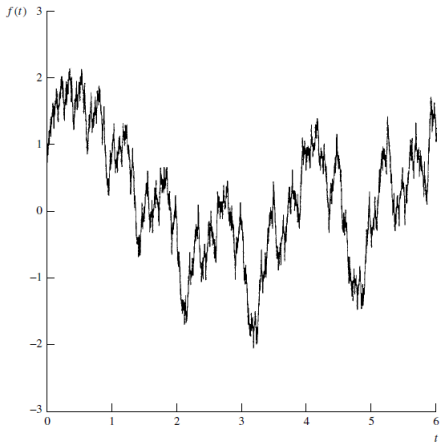

Figure 27: Graph produced by formula iteration using Equation 86

3.3 MODEL FRACTALS IN EM SIMULATION TOOL WITH THE AID OF MATLAB

As stated in Chapter 2, all the antennas presented in this thesis were designed and simulated in Ansoft HFSS, which is a 3D electromagnetic (EM) simulation software based on Finite Element Method (FEM). To use this EM simulator, as in other software packages, the antenna structure with all the geometrical details has to be modeled in the simulation environment. Considering antenna design based on fractal geometries, it is very inefficient to manually draw such compli-

cated geometries. Therefore, in order to solve this problem, a set of MATLAB m-functions have been developed to aid the modeling of fractal antennas.

The proposed method contains several steps. The first step is to use MATLAB to calculate and describe the fractal geometry in the form of a matrix. The fractal geometry is calculated using the recursive method to realize the Iterated Function System. The geometric information of this geometry is saved in a matrix that contains the value of X- and Y-coordinates of each node. The coordinates of these points are ordered in sequence from its start point to its end point. For example, Figure 28 shows the first iteration of the Koch curve. Assume that the coordinate of the start point (P1) is (0, 0) and it ends at P5 (0, 1), then in MATLAB the Koch curve is described by a 2-dimensional array as shown in Table 1.

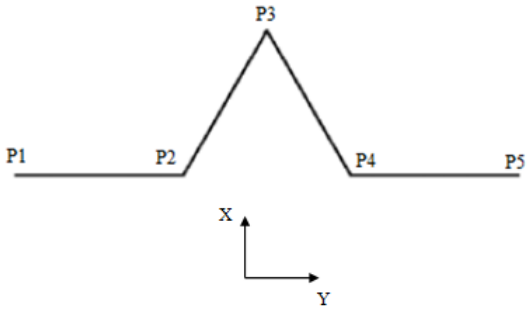

Figure 28: The 1st iteration of Koch Curve

Table 1: The list of coordinates for the Koch Curve

Point number	X-coordinate	Y-coordinate
1	0	0
2	0	0.333
3	0.289	0.5
4	0	0.666
5	0	1

To model one antenna, it is necessary to assign certain dimensions to each line to avoid having a structure of zero width. Therefore, in the simulation environment each line needs to be represented by a rectangular with a certain width. Based on the geometric matrix, a Visual Basic Script (VBScript)[1] file, which is a scripting language that can be read by most of the commercial EM software packages including HFSS, is written in MATLAB to translate the geometrical information with given physical dimensions into commands that can be executed by the EM simulator. For example, the Koch curve shown in Figure 28 will be transformed to the structure presented in Figure 29. To simplify the design process, some important parameters such as the total size (the maximum diameter) of the fractal geometry and the width of the microstrip line are added as design parameters for the antenna model, which enable user to reconfigure and update the antenna structure by adjusting these geometric parameters in the simulation software. The overall process of how to build the fractal in the EM simulation tool is illustrated in Figure 30 and a small sample of MATLAB code is given in Figure 31.

Figure 29: The model of Koch Curve in the simulation tool

Following the procedures described above, several MATLAB functions were written to create a variety of fractal geometries including *Koch Loop* and *Minkowski Island.* Some of these geometries have been applied to the design of printed monopole antennas, as presented in the following sections. These codes were compiled into a single MATLAB GUI, which provides a user friendly interface as depicted in Figure 32.

Using this tool several well-known fractal geometries such as Koch Snow, Hilbert Curve and Minkowski Island with pre-defined dimensions can be easily created. Figure 33 shows the application of this tool to create a Hilbert Curve of the 3rd iteration in HFSS. This tool works in following steps:

1. Firstly, the desired fractal curve is selected from the option list and then the user can specify the dimensions according to the

1 VBScript (Visual Basic Scripting Edition) is an Active Scripting language developed by Microsoft. In HFSS, it is used to create macros that can be executed to design models or export/import HFSS data. More information can be found in [45].

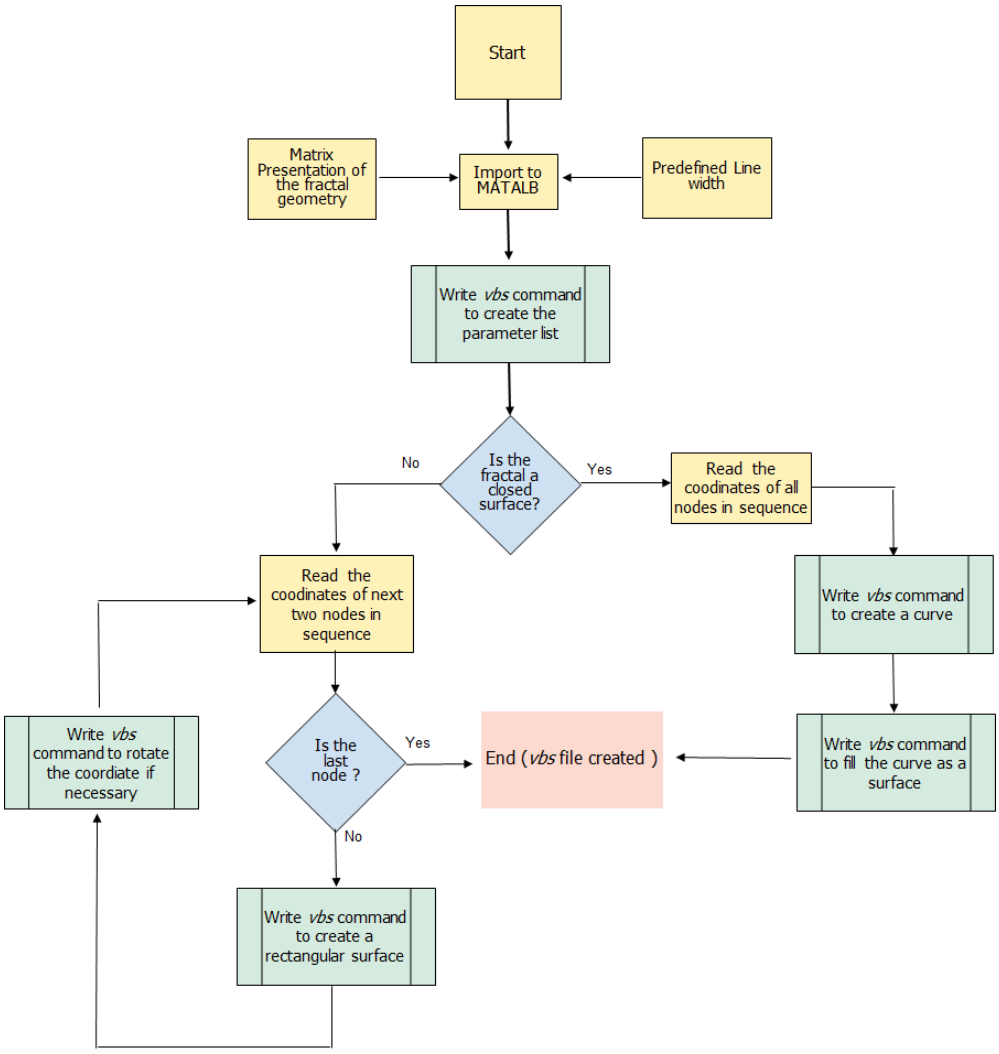

Figure 30: Process of design fractal geometries in simulation tool

requirement. Except for the iteration number, the 'size' and 'linewidth' parameters are not critical because these values can be changed in the final simulation model in HFSS.

2. The 'preview' button can be selected to preview the structure of the selected fractal geometry.

3. After specifying the directory to save the files, the corresponding *vbs* file is created by clicking the 'Run' button.

4. Run the *vbs* file under the user defined directory automatically creates the required fractal geometry in HFSS with the predefined parameters. The size and the line width can be directly modified in the parameter list in HFSS.

Figure 33 (c) shows the fractal geometry, Hilbert Curve, in the simulation software after executing the corresponding *vbs* file. One param-

```
function test_MinLoop
close all;
hfssScriptFile = 'E:\fractal design\fractal.vbs'; % set up
file path
fid = fopen(hfssScriptFile, 'wt'); % create vb file for a
new project
createNewProject(fid);
% add Local variables
addLocalVariable(fid,'size',25); % use "size" to control
the overall length of the fractal
addLocalVariable(fid,'w',0.25); % use "w" to control the
width of the microstrip line
iteration = 2; % define the iteration of the fractal
geometry
d = 4; % d is the depth of each iteration
fractal_curve_new(fid,iteration,d); % translate into the
final vbs file
fclose(fid); % close the vbs file
```

Figure 31: Example of MATLAB coding to create *vbs* file for designing fractal in HFSS

eter list, which enable one to adjust the fractal by updating the value of each parameter, is also created as depicted in Figure 33(b).

One additional tool was also created in MATLAB, which aims to create a microstrip impedance transformer line. This tool adopts two techniques, triangular taper and exponential taper, to design a microstrip line with the desired impedance characteristics. With this tool, the design of an impedance matching line for printed microstrip antenna is greatly simplified. Figure 34 (a) shows the interface of this tool and Figure 34 (b) presents one example of its application to create one impedance transformer line using triangular taper in HFSS. In this example, it is assumed that the substrate has permittivity of 3.38 and thickness of 0.813 mm. The theoretical explanation of the tapered microstrip transmission line can be found in [46].

In following sections, several proposed fractal-based printed monopole antennas are going to be presented. All of these antennas were designed by utilizing the tools described above.

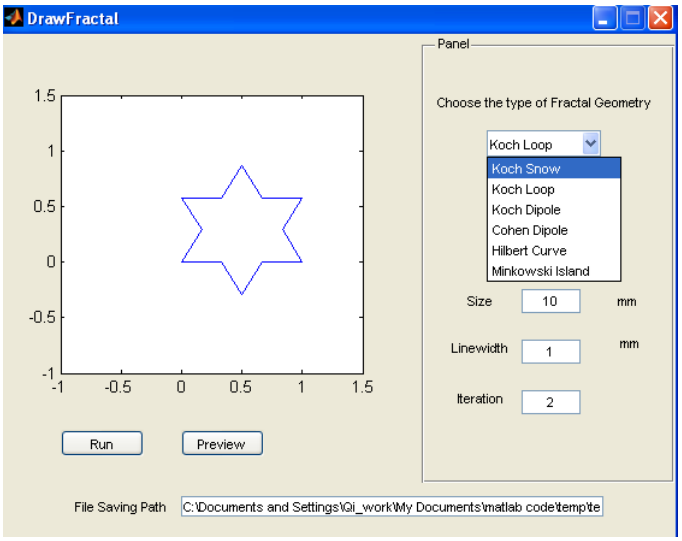

Figure 32: Interface of the MATLAB GUI tool for making fractal geometries in HFSS

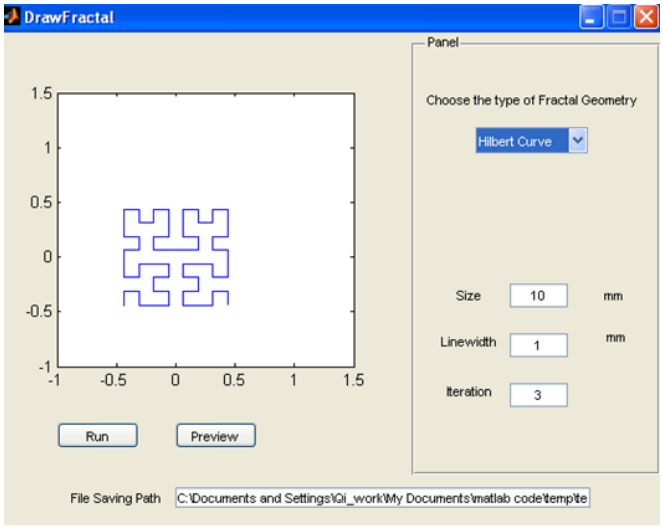

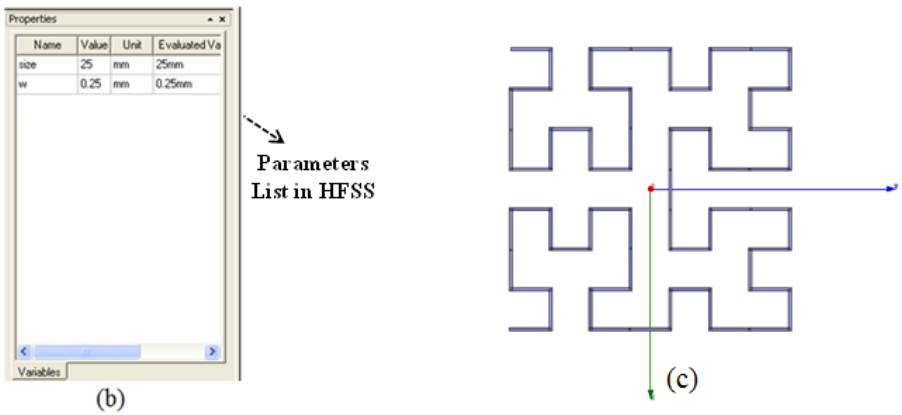

Figure 33: (a) Using GUI tool to make a vbs file for Hilbert Curve of 3rd Iteration (b) The parameters list shown in HFSS after executing the vbs file (c) Top view of the Hilbert Curve in HFSS

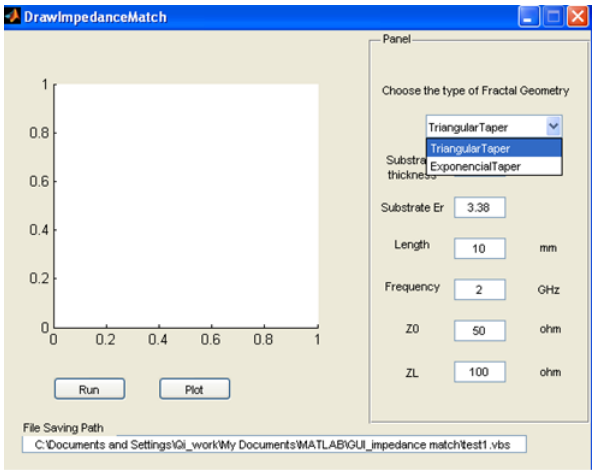

(a)

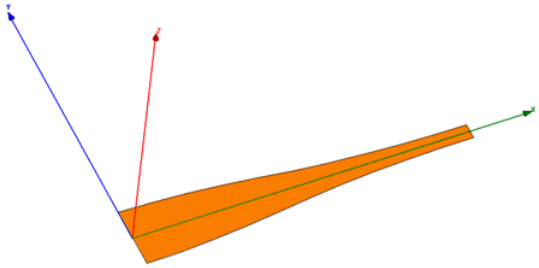

(b)

Figure 34: (a) Using GUI tool to make a vbs file for designing a microstrip impedance match line using the triangular taper technique; the impedance of this microstrip line is transformed from 50 to 100 ohm (b) Top view of the designed microstrip impedance line in HFSS

3.4 MULTIBAND FRACTAL MONOPOLE ANTENNA USING MINKOWSKI ISLAND GEOMETRY

3.4.1 *Motivation*

Recently, fractal techniques have been brought to the field of antenna design, named "fractal antenna engineering", and is attracting many research interests because of its advantages in antenna miniaturization as well as in providing multiband resonant frequencies with similar radiation characteristics. Indeed, the fact that fractal is a geometry that is self-repeated at different scale, which means that the fractal technique can be explored for designing antenna with multiple band operation. In [6], an overview of the progress of the fractal-based antenna design covering more than 120 published articles was presented. In the letter, it is found that most of the designs employed fractal techniques to design patch antennas and vertical monopoles with a large horizontal ground plane, in which case the size reduction brought by using fractals were not clear. Some designs adopted fractal of higher iterations [9, 47], which makes the antenna difficult to fabricate and increases the internal losses of the antenna. Recently, the modified Sierpinski gasket geometry was used in the design of a printed monopole antenna [48]. Compared to the use of the traditional Sierpinski geometry, the modified structure can achieve a higher size reduction. Although this antenna can operate at multiple frequencies, the bandwidth at the higher band is relatively narrow. Moreover, the resonant frequency at the higher band is sensitive to the width of the triangular ring.

Although fractal geometries are self-filling structures that can be scaled without increasing the overall size, not all the geometries can contribute to the compact antenna design. Previous research found that some fractal geometries such as Hilbert and Peano curves, which exhibit a high degree of space filling, cannot effectively reduce the resonant frequency of the antenna due to the canceling of the current between closely spaced lines [49]. It also has been proved that the multiband operation is not a unique feature of fractal geometries and in some cases non-fractal geometries show better performance in terms of operation bandwidth and radiation efficiency [50]. However, from the experimental results provided in [50], it is can be seen that wired antennas with fractal geometries do show better impedance matching characteristics.

The objective of this work is to apply the fractal geometry to the design of printed monopole antennas, which have attracted much research interest due to its simplicity, broad bandwidth and ease of integration in communication systems. Moreover, the chosen fractal can effectively reduce the size of the antenna whilst maintain the radiation performance of the antenna at a promising level.

3.4.2 *Antenna Design*

With the aim of demonstrating the applicability of the fractal technique to the design of multiband compact antennas, two printed monopole antennas were implemented based on the Minkowski Island geometry. The proposed antennas are designed for WLAN and WiMAX applications. The reason why Minkowski Island was chosen is that through our studies, it is found that applying this fractal geometry to the design of the printed monopole antenna can provide the desired frequency ratio for the design target. The frequency ratio of a multiband antenna is defined as the highest resonant frequency divided by the lowest one, which can be express as:

$$FR = \frac{f_{Max}}{f_{min}} \tag{87}$$

In this study, the objective is to design a dual band WLAN antenna that can operate at 2.4 and 5.2 GHz bands. This means that the desired frequency ratio needs to be:

$$FR = \frac{f_{Max}}{f_{min}} = \frac{5.2}{2.4} = 2.17 \tag{88}$$

The study of the frequency ratio of the monopole antenna using the Minkowski Island geometry will be discussed in next section. Figure 35 shows the first two iterations of Minkowski Island. Compared to other fractal geometries such as Hilbert curves, Minkowski Island geometry is much simpler and can work more efficiently with respect to the frequency reduction. As demonstrated in Figure 36, when a Hilbert curve is employed to design a printed monopole antenna, the closely spaced lines can cause a large amount of current cancellation, which means that the effectively electrically length of the antenna with Hilbert Curve cannot benefit much from using such space filling geometry.

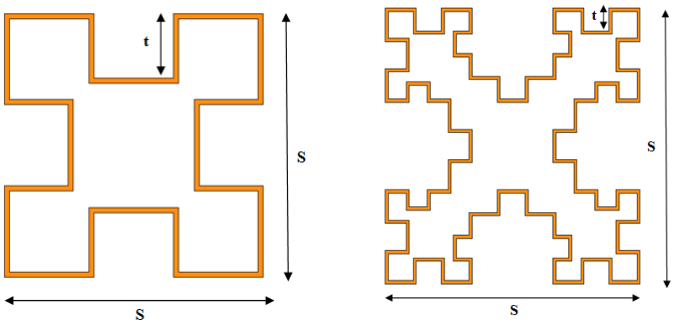

Figure 35: The 1st iteration and 2nd iteration of Minkowski Island geometry

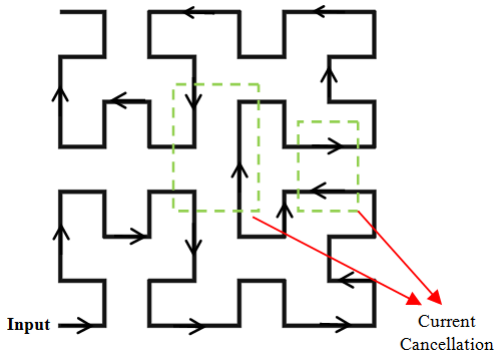

Figure 36: Demonstration of the current cancellation of monopole design using the Hilbert Curve

Theoretically, the higher iteration of one fractal is, the more size reduction of one antenna can be reached. However, in this study the reason why we did not choose to adopt other higher iterations is that when increasing the number of iterations, this specific fractal geometry becomes quite complex and a microstrip line of very narrow width is needed to describe it; then the conductor losses will increase significantly, which reduces the radiation efficiency of the antenna.

Figure 37 (a) presents the proposed fractal monopole with the geometry of the 1st iteration Minkowski Island. Its size is 28 mm $\times$ 18 mm with a partial ground plane having a width of 35 mm and length of 10 mm on the back side of the substrate. The width of the microstrip line (w) is 0.5 mm. Figure 37 (b) shows another proposed fractal monopole using the 2nd iteration Minkowski Island. Its size is 21.5 mm $\times$ 18 mm and the size of the ground plane is 30 mm $\times$ 10 mm. As the result of using a higher iteration fractal, the width of the microstrip line (w) is reduced to 0.25 mm. The depth t, shown in Figure 35, is $1/4$ of the side length ($\frac{1}{4}$s) at each iteration for both antennas. The line width of both antennas were decided by two factors. Firstly, the width of the microstrip line needs to be narrow enough to avoid the intersection between adjacent lines. This issue is more significant for fractal of higher iterations. The second consideration is for antenna input impedance matching. Both of the proposed antennas are printed on the top side of the substrate, 0.813 mm thick Roger 4003 with relative permittivity ε_r=3.38, while the ground plane is printed at the bottom side. Behind the antenna elements, there is no ground plane.

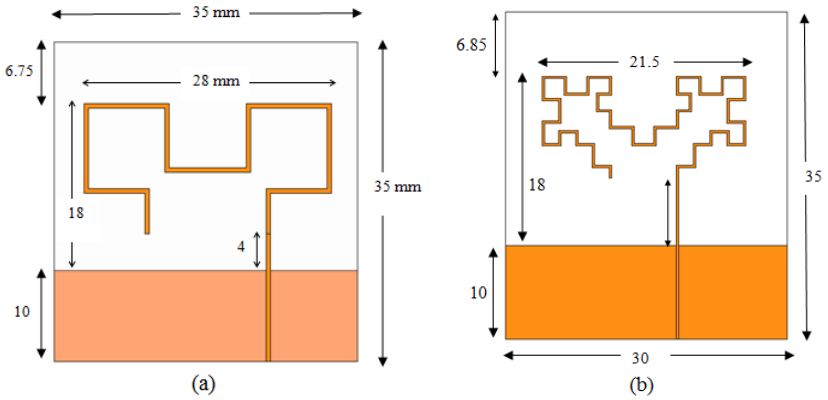

Figure 37: The proposed fractal monopole antenna with geometry of: (a) 1st iteration Minkowski Island; (b) 2nd iteration of Minkowski Island

3.4.3 *Simulated and Experimental Results*

The frequency ratio of the monopole antenna with the Minkowski Island can be controlled by changing the value of t, which is indicated in Figure 38. Let the value of t equals to s/d, parametrical studies were carried out by varying the value of d and the resulted frequency ratio of the antenna is plotted in Figure 38. As can be seen from Figure 38, although using fractals can contribute to the size reduction and multiple frequency operation of an antenna, the frequency ratio of the antenna is only limited from 2.05 to 2.17, which is a quite narrow range. Therefore, this fractal geometry cannot be applied to design multiband antennas with different frequency ratio. A solution to overcome this limitation will be presented Section 3.5 and 3.6.

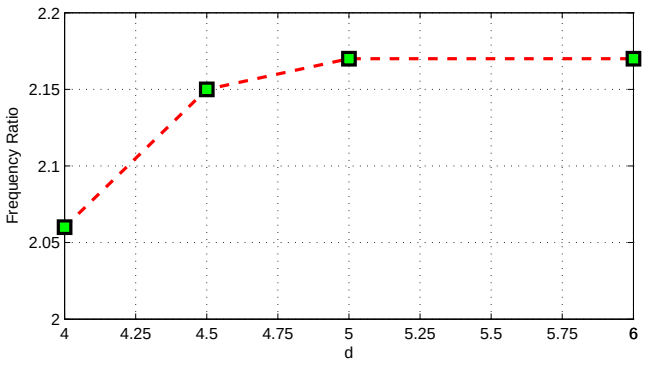

Figure 38: The frequency ratio of the antenna with different value of d

Both of the proposed monopole antennas have a compact size compared to conventional printed monopole antennas, which need to have a length of approximately a quarter of wavelength. Moreover, it is found that without using any additional impedance matching, both of the proposed antennas exhibit good impedance match at multi-

ple frequency bands, which is confirmed by the measurement results shown in Figure 39. The results show that the printed monopole of 1st iteration of Minkowski Island exhibits 10 dB return loss bands of 2.30 - 2.48 GHz, 3.3 - 3.7 GHz and 4.9 - 6.0 GHz, which covers the entire required frequency bands for 802.11a/b/g and WiMAX communications. For the 2nd iteration of Minkowski Island fractal monopole, the bands are 2.31 - 2.47 GHz and 5.0 - 5.5 GHz, which covers the two desired frequency bands for WLAN 802.11b/g standards.

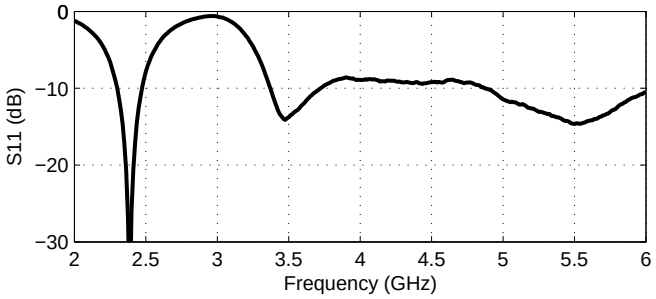

(a)

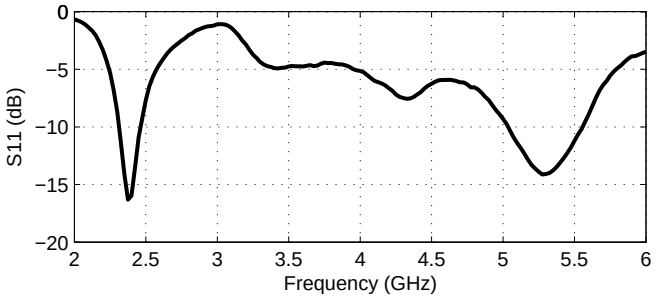

(b)

Figure 39: Measured S11 of the proposed antenna with the: (a) 1st iteration and (b) 2nd iteration of Minkowski Island geometry

Figure 40 presents the simulated surface current distribution of the proposed monopole antenna with the 1st iteration of Minkowski Island geometry at 2.4, 3.5 and 5.2 GHz. It is found that at 2.4 GHz, the resonance is influenced by the overall length of the fractal curve, the 3.5 GHz resonant frequency is mainly determined by the central part of the fractal geometry and the two corners of the fractal geometry are responsible for the higher band at 5.2 GHz.

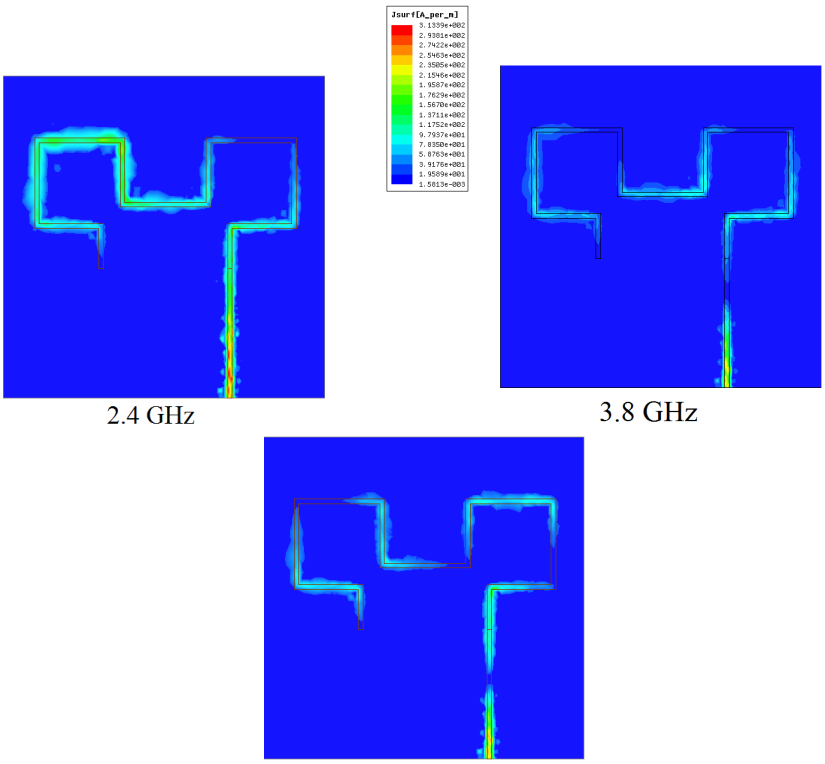

Figure 40: Simulated surface current distribution of the monopole antenna with the 1st iteration of Minkowski Island

Figure 41 presents the simulated surface current distribution of the proposed monopole antenna with the 2nd iteration of Minkowski Island geometry at 2.4 and 5.2 GHz. Similar to the 1st design, it is observed that for this antenna the lower frequency band is contributed by the overall length of the fractal, while the higher band is determined by the two corners of the fractal geometry.

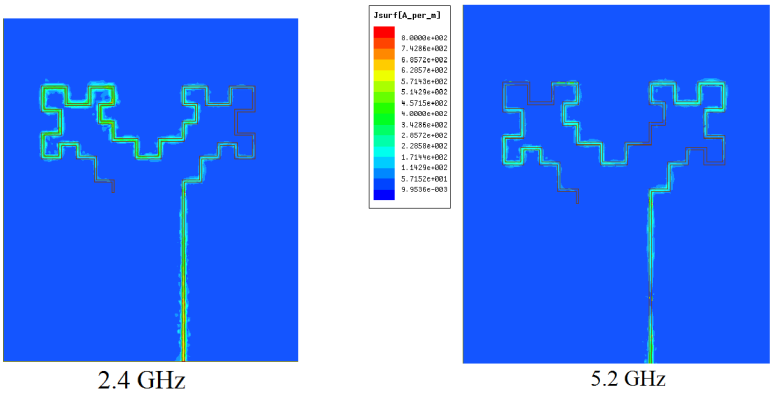

Figure 41: Simulated surface current distribution of the monopole antenna with the 2nd iteration of Minkowski Island

Figure 42 and 43 show the measured radiation patterns of the two proposed antennas. In both figures, the dotted line line depicts H

plane and solid line represents E plane. It is found that both antennas have radiation patterns as typical printed monopole antennas. The radiation patterns at H-plane are almost isotropic and in the E-plane they exhibit broadside radiation patterns, as expected. The measured maximum gain is around 1.5 dB at 2.45 GHz and 2.3 dB at 5.2 GHz for both antennas. According to the simulation results, the radiation efficiency is 94% and 88% at 2.45 GHz, 97% and 93% at 5.26 GHz for the printed monopole of 1st and 2nd iteration of Minkowski Island, respectively. From these results, it is found that although higher size reduction can be achieved using higher iteration of the fractal geometry, the bandwidth as well as the radiation efficiency also decreases. This should be considered as a trade-off between size reduction and antenna performance.

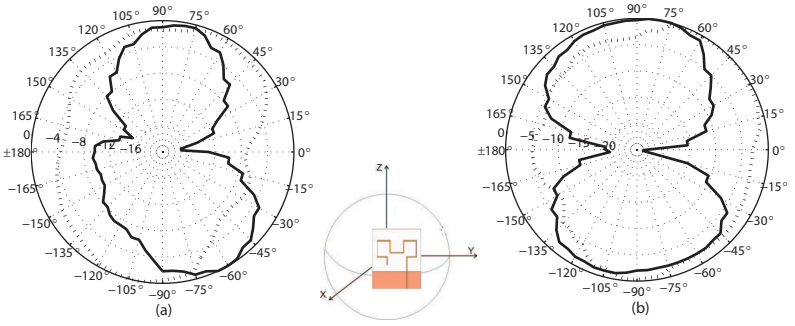

Figure 42: Measured radiation pattern of the proposed antenna with 1st iteration Minkowski Island at: (a) 2.4 GHz and (b) 5.2 GHz. Solid line represents measured results on X-Z Plane while dashed line represents measured results on X-Y plane

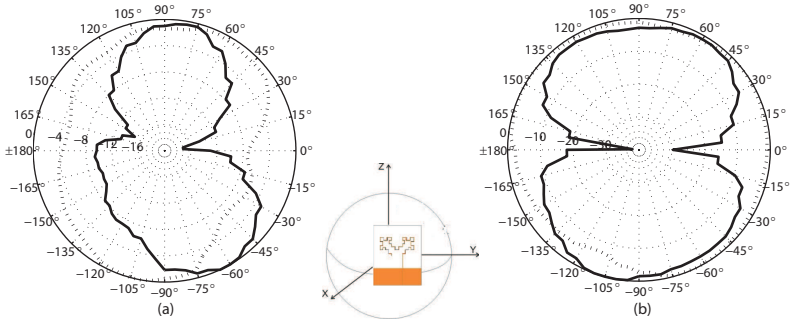

Figure 43: Measured radiation pattern of the proposed antenna with 2nd iteration Minkowski Island at: (a) 2.4 GHz and (b) 5.2 GHz. Solid line represents measured results on X-Z Plane while dashed line represents measured results on X-Y plane

3.4.4 *Antenna with Different Size of Ground Plane*

It is known that the ground plane size can influence the impedance matching and resonant frequency of a printed monopole antenna.

Hence, instead of viewing the antenna as one separate component of the wireless device, it should be taken as an integrated part of the entire layout of the transceiver. The performance of these two proposed fractal monopole antennas with different sizes of ground planes have been studied through numerical simulations in HFSS. Figure 44 (a) and (b) show the return loss of the two antennas presented in Figure 37 with different sizes of the ground plane. It was found that when increasing the size of the ground plane to 45 × 80 mm, which can be considered as the size of a PC card, both of the proposed Minkowski Island fractal monopoles can still exhibit good impedance matching over the required frequency bands except for some frequency shift, which can be easily solved by resizing the antenna. This means that the proposed two antennas can be implemented on PCB boards of different sizes with small modifications.

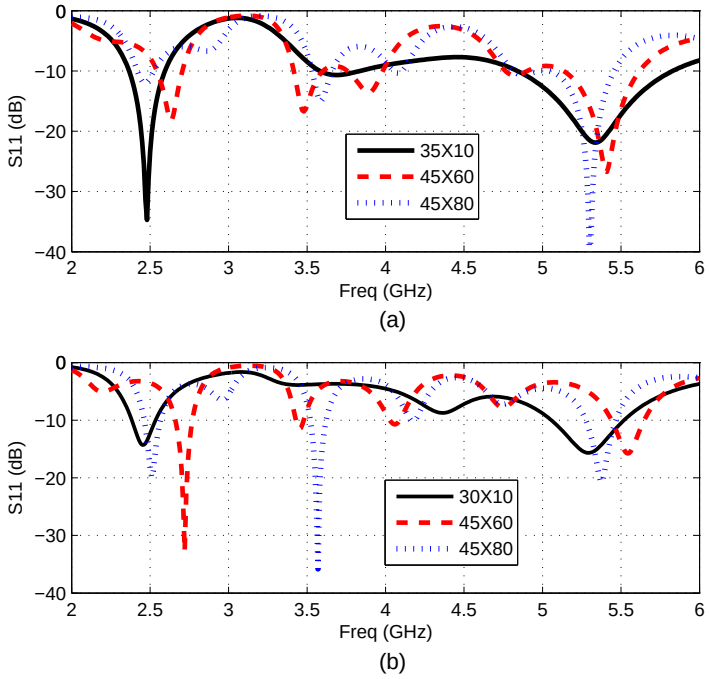

Figure 44: Simulated S11 of the proposed antenna: (a) with 1st iteration Minkowski Island and (b) with 2nd iteration Minkowski Island on ground planes of different size

3.4.5 *Conclusion*

Two printed fractal monopole antennas of compact size using the 1st and 2nd iteration of Minkowski Island geometries are proposed. The two proposed antennas exhibit good impedance match at both 2.4 and 5.2 GHz band, which is confirmed by the measurement results. It is also observed that the proposed monopole antenna with the geometry of the 1st iteration Minkowski Island can also operate at 3.5 and 5.8 GHz, which means that it almost covers the entire required

frequency bands for 802.11a/b/g and WiMAX communications. Both the simulation and measurement results suggest that these two fractal antennas are good candidates of multi-frequency antennas with high radiation efficiency and can be easily matched to the 50 Ω terminal with different sizes of ground plane. It is also important to point out that comparing the measurement results of the two proposed antennas, it is observed that although the size reduction can be achieved by using fractal geometries of higher iteration, the bandwidth as well as the radiation efficiency also decreases. This should be considered as a trade-off between size reduction and antenna radiation performance.

3.5 FRACTAL MONOPOLE ANTENNA FOR WLAN USB DONGLE

3.5.1 *Motivation*

The results presented in the previous section show that the fractal geometries can be applied to the design of multiband printed monopole antennas with reduced size. However, it is also found that as a multiband antenna, the frequency ratio of the fractal antenna using the Minkowski geometry is nearly fixed, which indicates that in order to extend the fractal technique to other multiband antennas design, there is a need to explore an effective solution to overcome this limit.

The methodology proposed in this work to extend the frequency ratio of the fractal-based antenna design is to combine the fractal geometry with the meander line. Then, this methodology is applied to the design of a compact antenna suitable for a commercial wireless device: WLAN USB dongle. Specifically the objective of this study is to design a printed fractal monopole antenna for WLAN USB dongle applications and based on the industrial requirement, the overall size of this antenna including the ground plane is chosen to be 20 mm $\times$ 60 mm and the available space for antenna design is limited to no more than 20 mm $\times$ 10 mm.

In [51], two internal multiband PIFA antennas were proposed for UMTS and WLAN applications for a USB dongle. Although both of them have compact size and can cover several useful commercial frequency bands, they are rather complicated to fabricate and the use of a short pin means that the size of the ground plane will play a significant role in influencing the resonant frequencies. In [52], one printed monopole antenna was also designed for WLAN USB dongle. This antenna employed the meander-line to reduce the occupied volume of the radiation element. However, this antenna can only operate at 2.4 GHz band, which is not enough for the targeted dual band WLAN application. In [53], one two armed printed monopole for WLAN has been proposed. The use of multiple arms provides an alternative solution to design a multiband printed monopole antenna. Yet, its size seems inappropriate for a USB dongle. In this work, the antenna pro-

posed has a completely planar structure, multiple frequency operation and compact size, which overcomes these limitations and further justifies the advantages of implementing fractals in printed monopole antennas design.

3.5.2 *Antenna Design*

A variation of the Koch fractal, which also can be referred as Cohen dipole fractal geometry, was used to design the proposed multiband printed monopole antenna. The Cohen dipole geometry, which is a variation of Koch fractal, was first proposed by Nathan Cohen [54] to design a dipole antenna with the feeding at the center position. Figure 45 shows the first three iterations of the Cohen dipole fractal geometry.

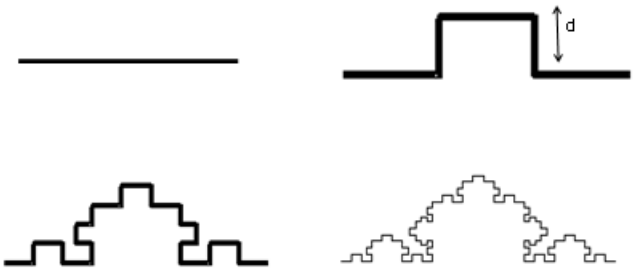

Figure 45: The first three iterations of Cohen dipole

Similar to the previous studies presented in Section 3.4, in this work the second iteration of the fractal was employed as higher iterations require a narrow microstrip line, as depicted in Figure 45, which increases the loss of the antenna. Figure 46 shows the top and bottom view of the proposed printed fractal monopole antenna. This antenna is designed on the Roger 4003 substrate with dielectric constant of 3.38 and thickness of 0.813 mm. The space occupied by the monopole antenna on the substrate is 10 mm $\times$ 20 mm and the size of the ground plane is 50 mm $\times$ 20 mm, which is a typical size for a USB dongle. This structure was further optimized by doing numerical simulations in Ansoft HFSS to achieve a better impedance match at the required frequency bands. It is found that the size of the fractal geometry is critical in defining both the resonant frequencies while the existence of the horizontal microstrip line (the one with length of 8.1 mm shown in Figure 46) plays the role of adjusting the resonant frequencies to the desired region. Without the horizontal microstrip line, it is found that the proposed antenna can only exhibit resonances at around 2 and 6 GHz, which fails to cover the desired frequencies for WLAN dual-band applications. However, adding the horizontal microstrip line with the appropriate length, the frequency ratio of the fractal antenna can be more controlled. To avoid repetition, the para-

metric studies of the antenna structure are presented in Section 3.6, which utilizes the same antenna geometry to design an Inverted-L antenna (ILA).

After optimization, the width of the feeding microstrip line was chosen to be 1 mm and the width of the horizontal microstrip line was 0.5 mm. For the fractal, the width of the microstrip line was set to 0.35 mm. The depth d (shown in Figure 45) of the Cohen dipole is set to be $1/5$ of the line length at each iteration. Figure 47 shows the top and bottom view of the fabricated antenna prototype on the substrate Roger 4003.

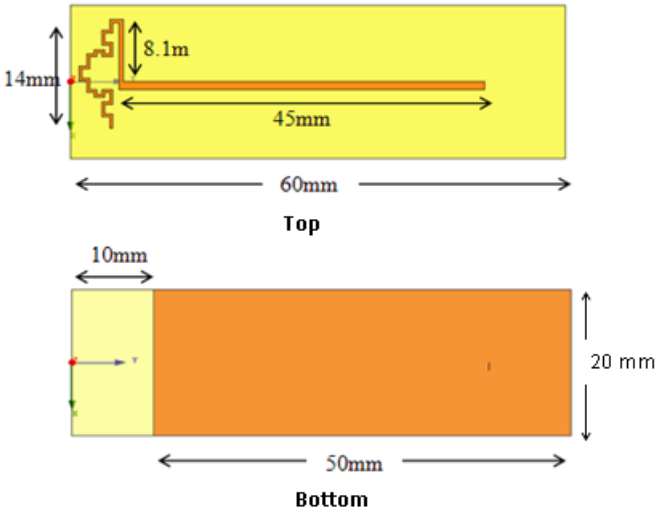

Figure 46: Top and bottom view of the proposed fractal monopole antenna

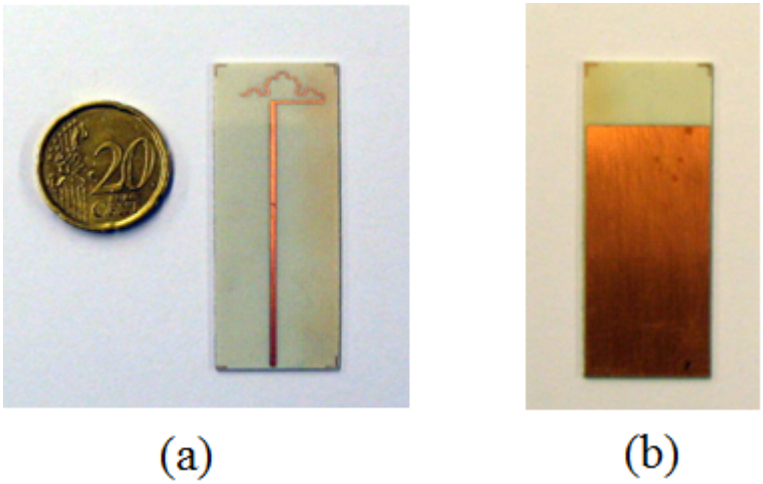

Figure 47: (a) Top and (b) bottom view of the fabricated fractal monopole

3.5.3 *Simulated and Experimental Results*

Figure 48 presents the measured return loss (S11) of the fabricated antenna. The experimental result shows that this antenna has a 10 dB return loss bandwidth of 2.22 to 2.52 GHz and 5.03 to 5.84 GHz, which covers the entire required band for WLAN 802.11a/b/g standards.

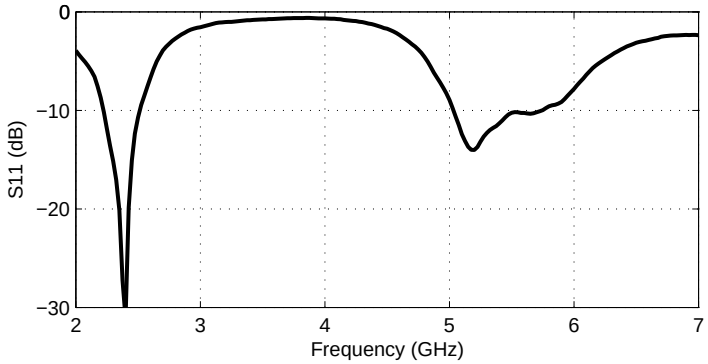

Figure 48: Measured S11 of the proposed USB fractal antenna

Figure 49 presents the simulated surface current distribution at 2.4, 5.2 and 5.8 GHz. It can be seen that at lower resonant frequency, 2.4 GHz, the surface current is concentrated on the meander line and all the fractal. At the higher frequency band, there is a strong current on the central section of the fractal.

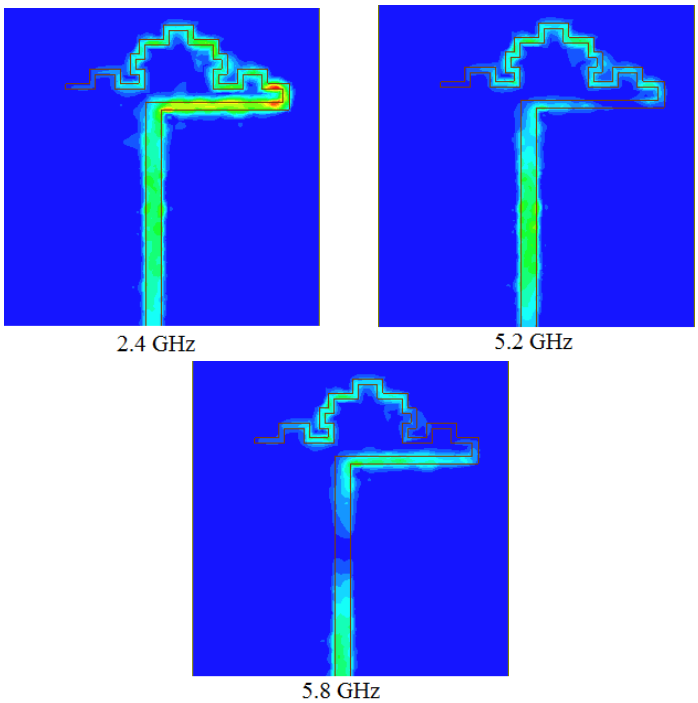

Figure 49: Simulated surface current distribution at 2.4, 5.2 and 5.8 GHz of the proposed antenna

Figure 50 shows the measured radiation patterns of both E-and H-plane at 2.4 and 5.2 GHz. From these experimental results, it can be seen that at both bands the radiation patterns in the H plane is almost isotropic while in the E plane the proposed antenna exhibits broadside radiation pattern and has two nulls at 90 and 180 degree, which acts similarly to a typical monopole antenna. Based on the simulation results, it is found that the proposed antenna has a constant peak gain of 1.8 dBi and 2.4 dBi at 2 and 5 GHz bands, respectively. Furthermore, the simulation results also indicate that this antenna has high radiation efficiency at both bands: 95% at 2.4 GHz band and 94% at 5.2/5.8 GHz band.

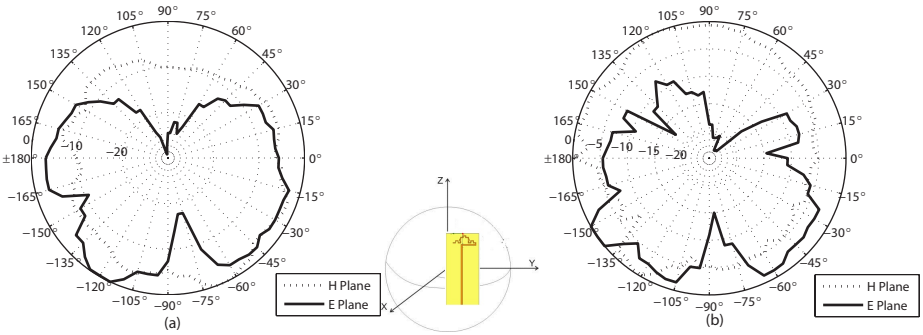

Figure 50: Measured radiation patterns at: (a) 2.4 GHz and (b) 5.2 GHz. Solid line represents measured results on X-Z Plane (E-Plane) while dashed line represents measured results on X-Y plane (H-plane)

3.5.4 *Conclusion*

In this work one printed fractal monopole antenna for WLAN USB dongle application has been proposed. In this design, the meander line is combined with a variation of the Koch fractal to achieve the desired multiband operation characteristic. Besides being compact, the proposed antenna has a completely planar structure, which is simple and easy to fabricate. Measurement results confirm that the proposed antenna covers the required frequency bands for WLAN 802.11a/b/g and the simulation results show that at both bands, the antenna exhibits high radiation efficiency.

One disadvantage of this design is that the feeding line of the antenna needs to cross a large section of the ground plane, which may be not convenient for an industry product design. In next section, an improved design which changes the antenna type to an Inverted-L antenna will be presented.

3.6 INVERTED-L ANTENNA (ILA) DESIGN USING FRACTAL FOR WLAN USB DONGLE

3.6.1 *Motivation*

This work is a continuation of the previous investigation presented in Section 3.5, which utilizes the fractal technique to design a compact printed monopole antenna for dual-band WLAN USB dongle applications. As stated in Section 3.5, one disadvantage of the previous design is that it requires additional space for the feeding line. This study aims to use the same fractal-based structure of the previous work to design an Inverted-L Antenna (ILA), which has been widely used in portable devices and can be easily integrated into an industry product. Moreover, the radiation performance of the proposed antenna when connected to a laptop computer was also investigated in this work.

3.6.2 *Antenna Design*

As a typical printed monopole antenna, the antenna element with the feeding line and the ground plane are printed at the top and bottom side of the substrate, respectively. The feeding port is located at the end of the substrate as shown in Figure 51. This might be a problem in a practical industry design as other components, such as RF module, also need to be mounted on the same ground plane.

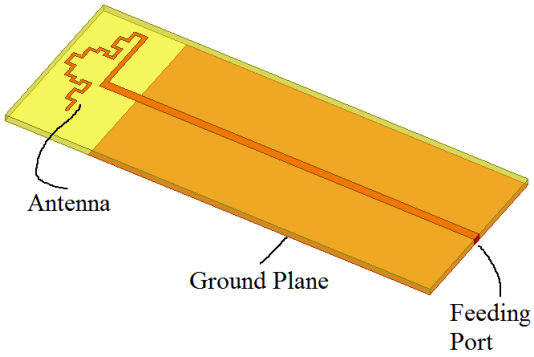

Figure 51: The structure of the previously designed antenna for WLAN USB Dongle

Figure 52 shows the proposed ILA antenna using the fractal-meander line based geometry. This antenna has the same dimension as the previous monopole antenna and is also designed on the same substrate: Roger 4003 with thickness of 0.813 mm. It can be seen that in this design, the antenna element and the ground plane are printed on the same side of the substrate and in the back side of the substrate, there is no copper. This could further simplify the fabrication process.

Most importantly, the feeding point has moved to the top edge of the partial ground plane and this leaves enough space to mount other hardware components.

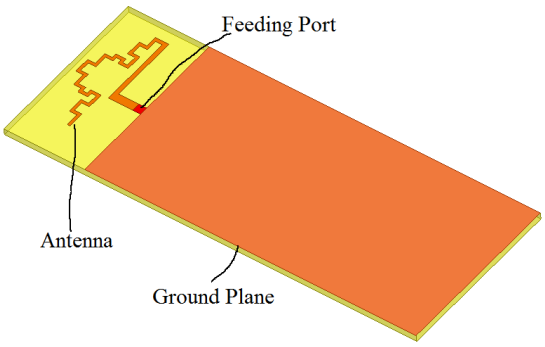

Figure 52: The proposed fractal ILA for WLAN USB Dongle

3.6.3 *Simulated and Experimental Results*

The proposed fractal ILA was fabricated (Figure 53) and Figure 54 compares the return loss between simulation and measurement results. It can be seen that there is a good agreement between the simulated and measured return loss. The experimental result indicates that the proposed antenna has a S11< -10 dB bandwidth from 2.25 to 2.60 GHz and 5.06 to 5.62 GHz. Comparing the proposed ILA with the previously developed monopole antenna, the return loss of both antennas are very similar, as seen in Figure 55. It is believed that both antennas should exhibit similar radiation patterns; hence, the radiation patterns of this fractal ILA are not going to be presented again in this section.

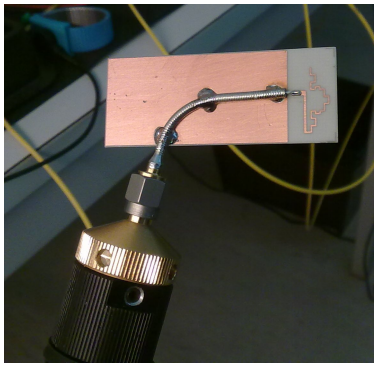

Figure 53: Photo of the fabricated prototype during return loss measurement

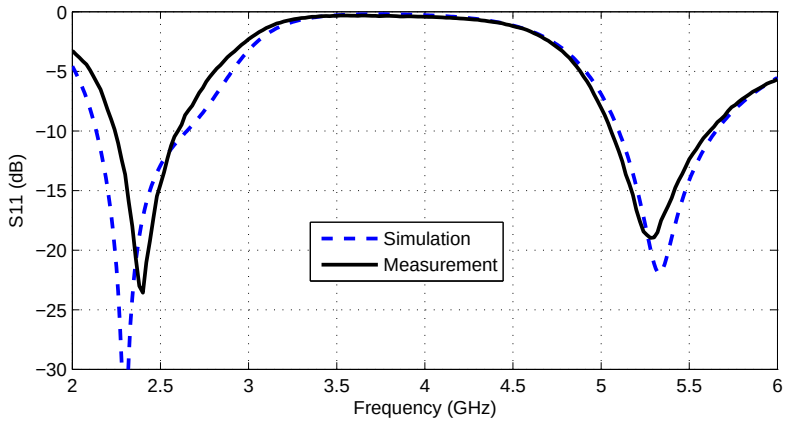

Figure 54: Comparison of the simulated and measured S11 of the fractal ILA

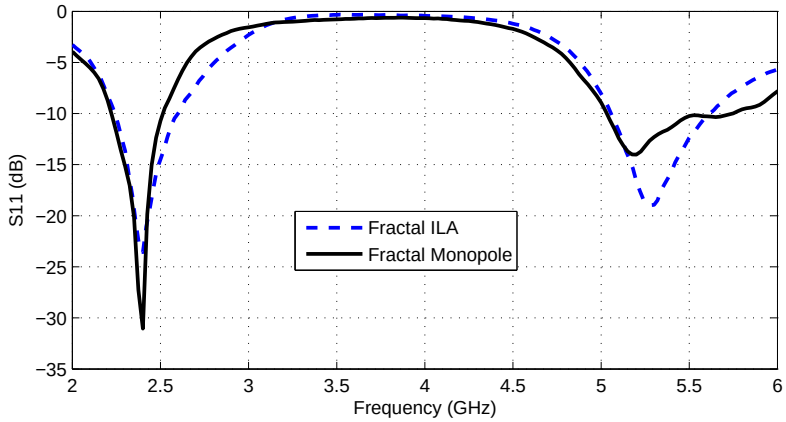

Figure 55: Comparison of the measured S11 of the fractal ILA and previously proposed fractal monopole

In order to show the effectiveness of antenna size reduction by using the fractal geometry, one more Inverted-F Antenna (IFA) was designed. This antenna uses the same substrate and the radiation element was also confined within the required area of size 20 mm × 10 mm, as shown in Figure 56.

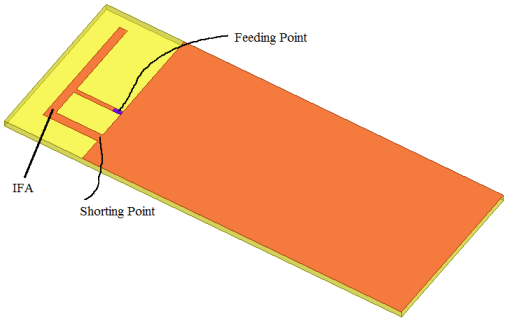

Figure 56: The structure of a typical Inverted-F antenna

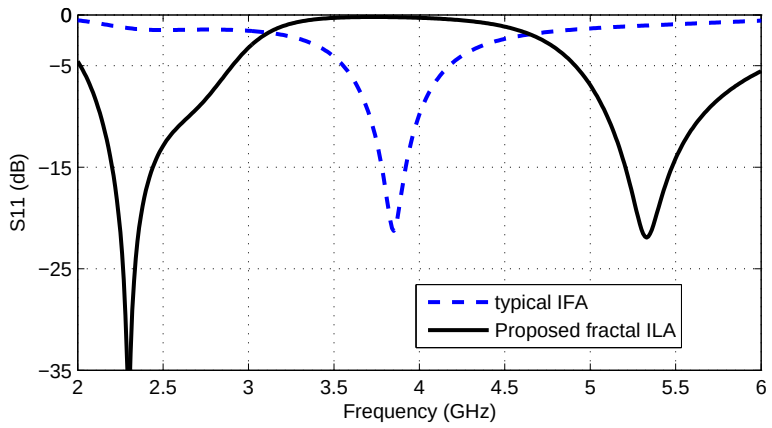

Figure 57: Comparison of the simulated return loss between the proposed fractal ILA and a typical Inverted-F antenna

Figure 57 compares the simulated return loss of this IFA with the proposed fractal ILA. As can be observed from this figure, the simple IFA can only operate at 3.85 GHz. Compared to the IFA, besides exhibiting a dual band operation, the proposed ILA antenna can resonate at 2.3 GHz, which represents a frequency decrease of 40%.

As stated before, the antenna needs to be taken as an integrated part of the entire layout of the transceiver. It is predictable that after assembling and connecting the USB dongle to the device, for instance a laptop computer, the radiation performance of the antenna might be affected. Therefore, it is necessary to do some parametrical studies for the proposed antenna in order to find out how the resonant frequencies of the antenna can be tuned to desired ones in the final stage of product design. Two key parameters, L_0 which is related to the overall length of the fractal and L_1, which is length of the horizontal meander line, were chosen as the variables. These two parameters are labeled in Figure 58. Figure 59 (a) and (b) present the simulated return loss of the proposed fractal ILA with different values of L_0 and L_1, respectively. It is found that the overall length of the fractal determines the resonant frequencies at both bands while the length of L_1 has a major influence on the higher band. The distance between the fractal and the horizontal line, which is indicated as L_2, has little influence on the resonant frequencies and impedance matching of the antenna, as shown in Figure 60. Therefore, this length is kept short in order to make the antenna be compact. By utilizing these findings, the frequency ratio of such fractal antenna can be controlled from 2.2 to 2.6 (see Figure 61) and the resonant frequencies of the antenna can be tuned to the frequencies of interests according to the requirements.

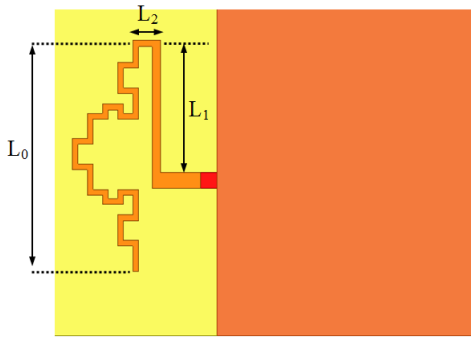

Figure 58: The layout of the proposed antenna

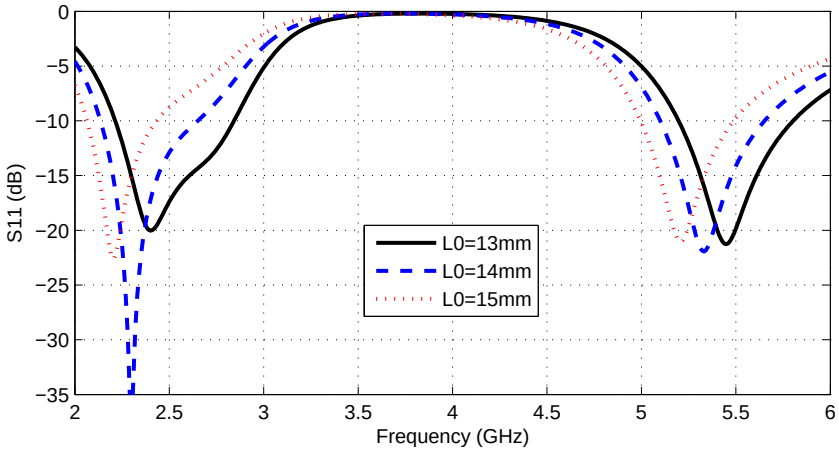

(a)

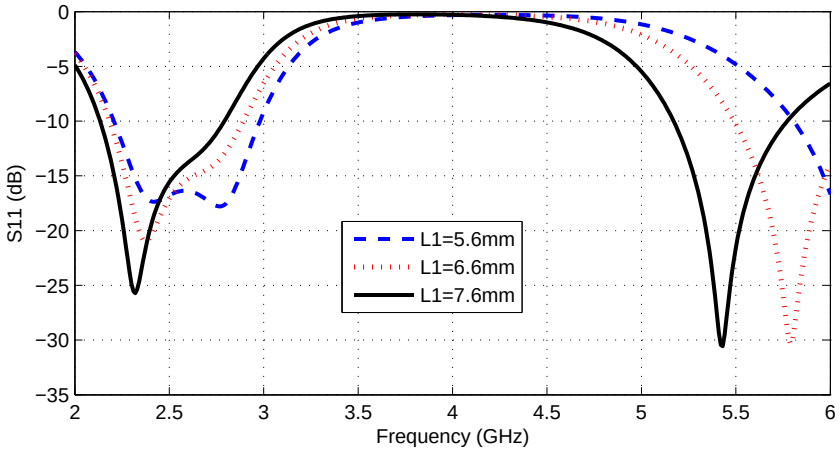

(b)

Figure 59: Parametrical studies for the proposed antenna: (a) simulated S11 of the antenna with different value of L_0; (b) simulated S11 of the antenna with different value of L_1

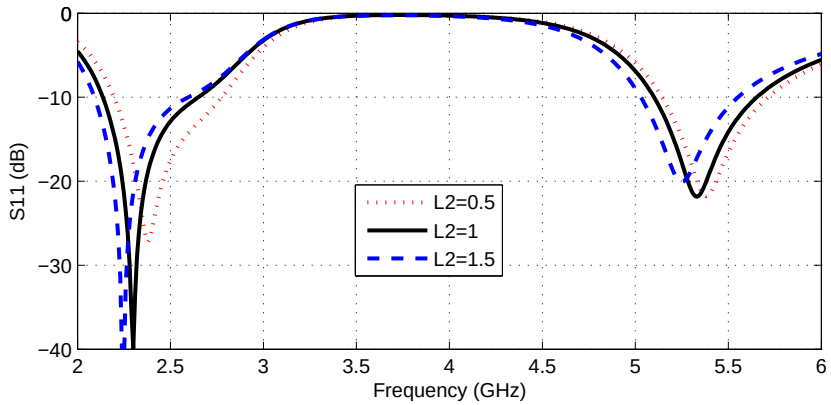

Figure 60: Simulated S11of the antenna with different value of L_2

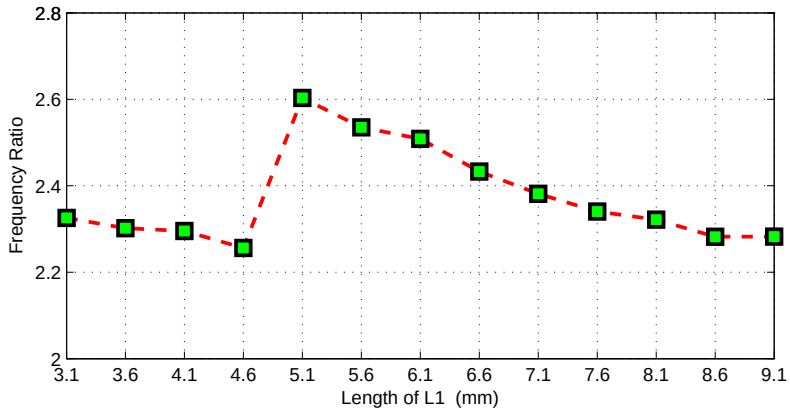

Figure 61: The frequency ratio of the antenna with different value of L_1 (the length of L_0 is fixed to 14 mm)

3.6.4 *Antenna Performance Connected to a Laptop*

The influence of the laptop on the radiation performance of the antenna was studied by simulating the USB dongle attached to a Laptop computer that is modeled as finite conductive material for simple consideration. When the USB dongle is connected to the laptop, it is equivalent to extend the size of the ground plane of the antenna to a much larger one. As the simulation software package used in this study, Ansoft HFSS, is a based on the Finite Element Method, in which the calculation is proportional to the size of the overall domain, therefore, to save simulation time and computation memory, the size of the laptop is truncated to half of the size of the real laptop computer. The simulation model is presented in Figure 62. The laptop is modeled as two copper plates vertically joined together to mimic the case when the laptop is opened. Each of the copper plate is 20 cm long and 10 cm wide, which is approximately half of the size of a notebook PC.

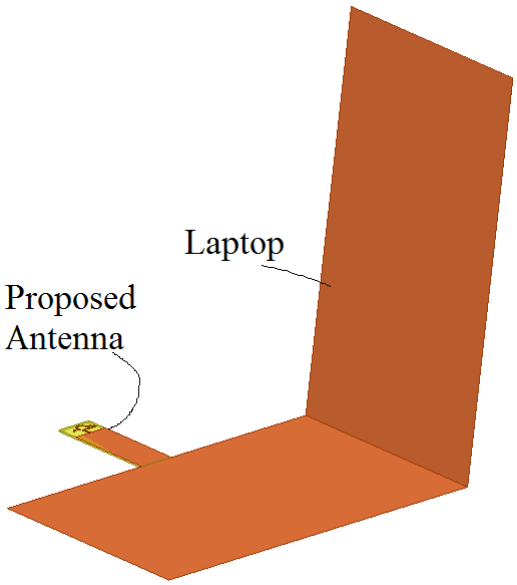

Figure 62: The simulation model of the fractal ILA connecting to the laptop in HFSS

Figure 63 shows the comparison of the simulated return loss of the proposed antenna with and without connection to the laptop computer. As expected, with the antenna connects to the laptop, some frequency shifts at both bands were observed. At the lower band, the amplitude of the return loss has degraded by more than 10 dB. After resizing the fractal, both resonant frequencies were tuned to the desired frequency bands, as shown in Figure 63 by the black solid line. After tuning, the simulation results show that the proposed antenna (connected with the laptop) exhibits a VSWR 3:1 bandwidth, which is the standard accepted by most portable devices manufactures, over 2.36 to 2.54 GHz and 4.96 to 5.84 GHz. This covers the entire frequency bands for IEEE 802.11 a/b/g applications.

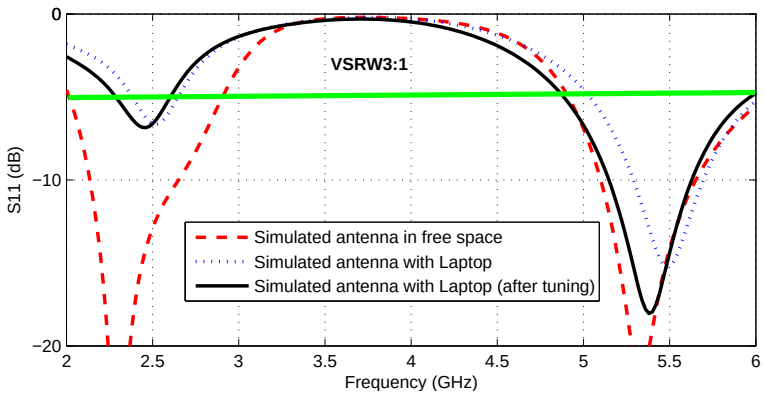

Figure 63: Simulated S11 of the proposed antenna with and without the laptop

Figure 64 presents the comparison of the simulated return loss of the proposed antenna with the laptop computer of different sizes. As can be seen from this figure, the size of the laptop computer affects in some degree the resonant frequencies of the antenna. However, above 15 cm the resonant frequencies of the antenna are no longer influenced by the length particularly at the lower band. This proves the validity of the simple simulation model of the laptop computer.

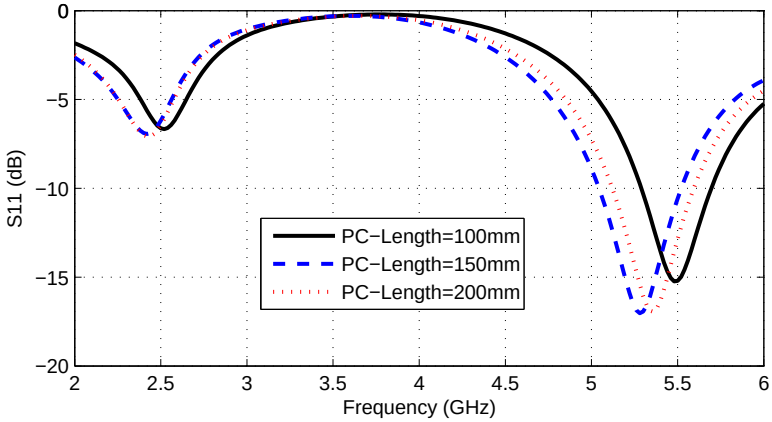

Figure 64: Simulated S11 of the proposed antenna with laptop computer of different length

Figure 65 presents the simulated 3D radiation patterns of the proposed fractal ILA in free space and when connects to the laptop at 2.4 and 5.2 GHz. It can be observed that there is a large influence of the laptop on the radiation pattern of the antenna. Moreover, according to the simulation results, the radiation efficiency of the antenna decreased by more than 40% compared to the case when in free space.

3.6.5 *Conclusions*

In summary, in this study a fractal ILA using the 2nd iteration of the *Cohen Dipole* fractal geometry combined with the meander line has been proposed. This antenna exhibits wide operation bandwidth and the radiation performance of the proposed antenna connected to a laptop computer is also studied. It is found that connecting the USB dongle to the laptop computer can affect the resonant frequencies of the antenna and greatly change its radiation patterns. The frequency shifting of the proposed antenna caused by the laptop can be tuned by resizing the fractal, which has been confirmed by the simulation results.

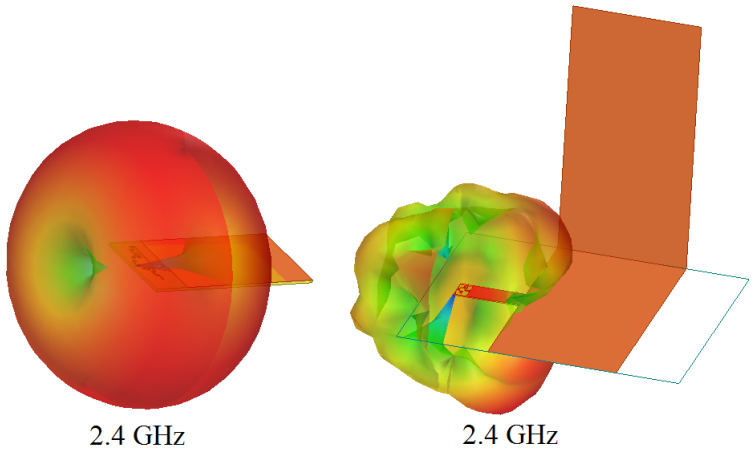

(a)

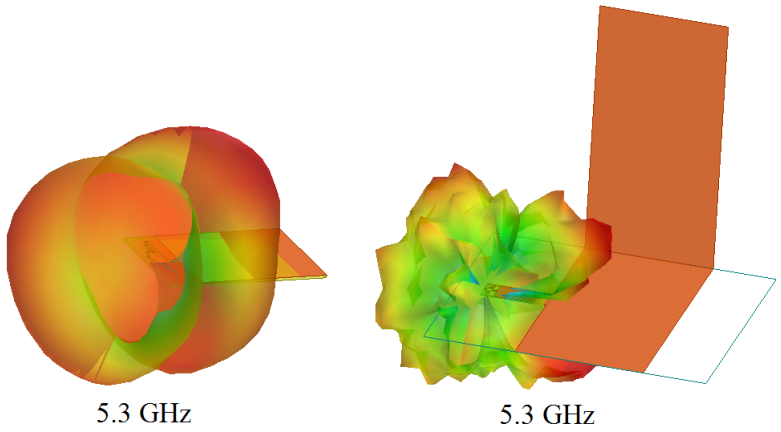

(b)

Figure 65: Simulated radiation patterns of the proposed fractal ILA in free space and connected with a laptop computer

3.7 SINGLE FEED FRACTAL MONOPOLE ANTENNA ARRAY

3.7.1 *Motivation*

To increase the directivity of a antenna system, the use of antenna arrays is an effective solution if an additional antenna element can be added in the wireless device. A single feed antenna array has the advantages of easy fabrication and does not need any extra RF components such has phase shifter. The objective of this work is to design one compact single feed multiband printed monopole antenna array for WLAN dual band application. It is desirable to design such antenna in planar structure as it can simplify the fabrication process and reduce the fabrication cost. Based on the results of the previous studies in Section 3.4, which confirms the size reduction and multiple frequency operation of the antenna using the fractal technique, the 2nd iteration of the Minkowski fractal geometry was chosen for this design.

In [55, 56], two single feed circular polarized microstrip antenna arrays were presented. The concept behind these two designs is to use the antenna array to achieve circular polarization and improve the directivity of the antenna. However, these two antennas have relatively large size and can only operate at a single frequency band. One printed single feed monopole antenna array has been reported in [57]. In that design the antenna array contains three equally spaced equilateral triangular monopoles of different sizes, which contribute to the multiple resonant frequencies at 2 and 5 GHz bands. However, the antenna in [57] is actually a multi-armed structure rather than a real array. The radiation performance of the antenna does not benefit much from using such antenna array. In [58], two multiband printed monopole antennas using the 1st and 2nd generation of the Minkowski fractal geometry were presented. The antennas have compact size and show multiband operation with wide bandwidth. However, so far, there is not much work reported on the use of fractals to design compact single feed printed monopole antenna arrays.

One common problem that is always encountered during the design of multiband antenna is how to improve the impedance matching at multiple resonant frequencies. In [59], band broadening was achieved through the use of a rectangular monopole backed by a trapezoid conductor. However, this method can greatly change the resonant frequency of original antenna and the size of the trapezoid is very critical, which is not easy to optimize. Reference [60] shows an example of designing a multiband printed monopole antenna using Genetic Algorithm. Although the antenna has a wide operation band, it has a complicated pattern and the impedance matching improvement was achieved through repetitive numerical simulations. In this work, these limitations are overcomed by adding a rectangular stub

on the edge of the partial ground plane to improve the impedance matching of the antenna with little influence on the original resonant frequencies.

3.7.2 *Antenna Design*

The 2nd iteration of the Minkowski fractal geometry (Figure 35) was chosen for this design due to its compact size. Figure 66 shows the geometry of the first prototype of the proposed fractal monopole array. This antenna was fabricated on a Roger 4003 substrate of thickness 0.813 mm and relative permittivity 3.38. To facilitate the simulation and fabrication, at this stage the size of the substrate was chosen to be 60 mm $\times$ 65 mm and the size of the ground plane is 30 mm $\times$ 65 mm. The antenna is constituted by two equal 2nd iteration Minkowski fractal monopoles fed by a single microstrip line of 1.89 mm wide. The line width of the fractal geometries is 0.25 mm and they are connected to the feed line by another horizontal microstrip line of width 1.2 mm. The partial ground plane is printed on the back side of the substrate and the antenna is printed on the top side.

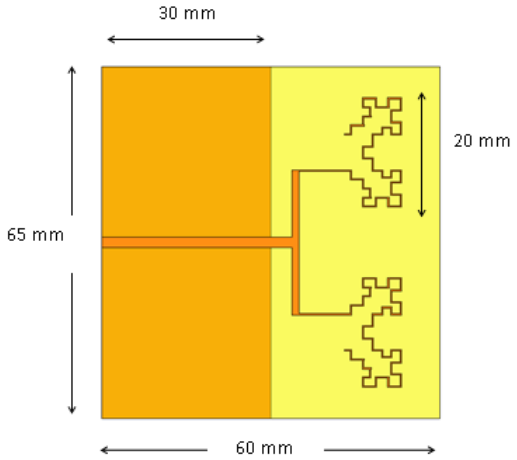

Figure 66: Structure of the 1st prototype fractal monopole antenna array

After optimizing the width of the feed lines by performing numerical simulation in HFSS, it is found that the bandwidth of this antenna is not as good as expected. More specifically, the bandwidth at the higher band (5 GHz) is quite narrow. Figure 67 presents the measured return loss of this antenna prototype.

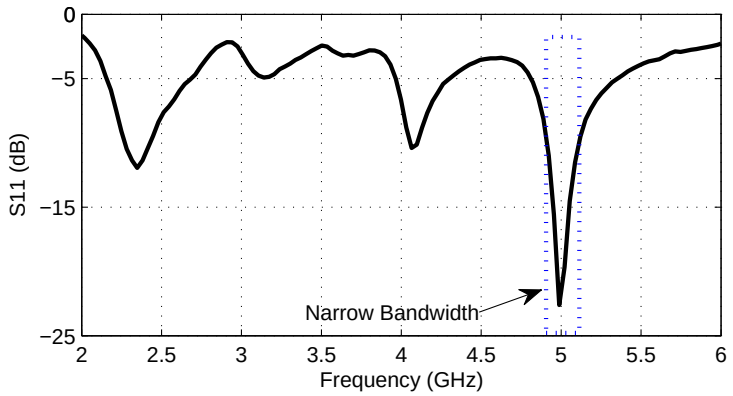

Figure 67: The measured S11 of the 1st prototype of the designed single feed fractal antenna array

Therefore, it is necessary to find a method to improve the bandwidth of the antenna at the higher band without affecting too much the resonant frequency at the lower band. Some common impedance matching methods such as quarter-wavelength transformer line or microstrip taper line, besides their large size they are not suitable for this situation as they can only be applied to single band antenna. After several attempts, it was found that by adding a stub on the top edge of the ground plane, the impedance match of the antenna can be improved with little influence on the original resonant frequencies. Figure 68 presents the proposed method with different shapes of the stubs including rectangular, circular and triangular on the ground plane. These different structures were simulated and Figure 69 compares the simulated return loss of these designs with the original design. It is observed that adding a stub on the top edge of the ground plane can effectively improve the bandwidth of the proposed antenna, which is a method much simpler and more robust than the one proposed in [59]. Comparing the different shapes, stub of rectangular shape is more effective in improving the return loss. This finding has been confirmed by both simulation and measurement results, which will be presented later.

Figure 70 shows the geometry of the 2nd proposed fractal monopole array with improved impedance matching. Compared to the one presented in Figure 66, the only difference is that in the second design, one stub of size 3 mm $\times$ 8 mm is added on the top edge of the ground plane.

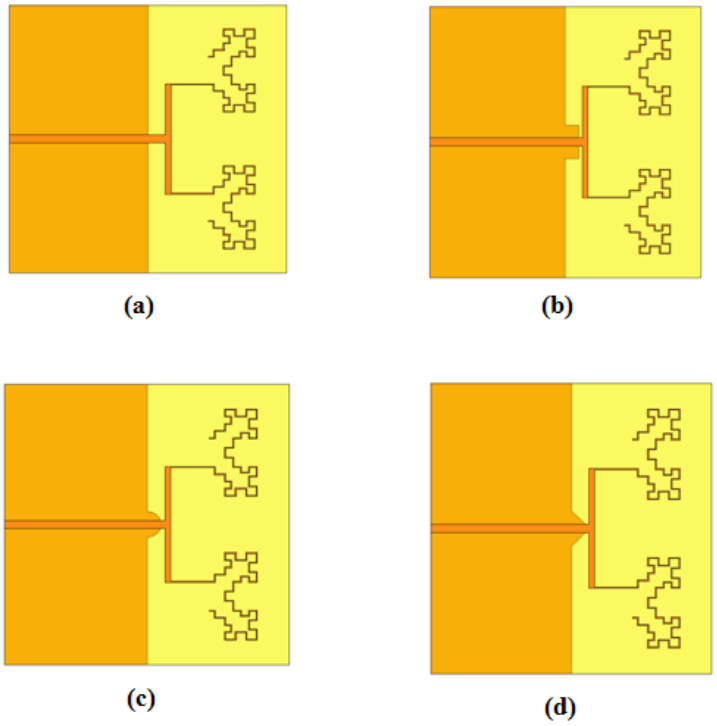

Figure 68: Proposed fractal antenna with different shapes of stubs on the ground plane: (a) Original design; (b) Ground plane with rectangular shape stub; (c) Ground plane with circular shape stub; (d) Ground plane with triangular shape stub

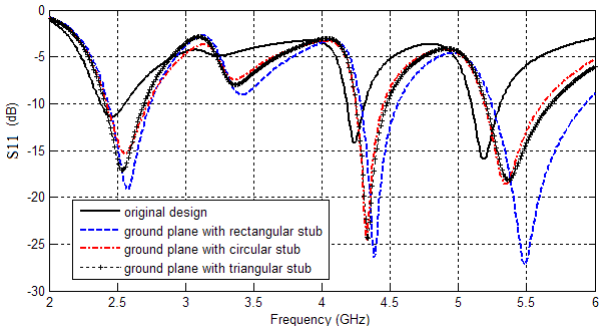

Figure 69: Simulated S11 of the proposed antenna with different stubs on the ground plane

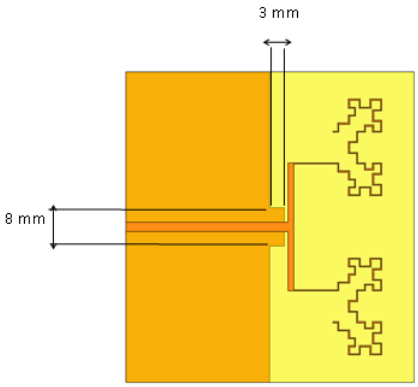

Figure 70: Structure of the 2nd prototype fractal monopole array antenna with improved impedance match

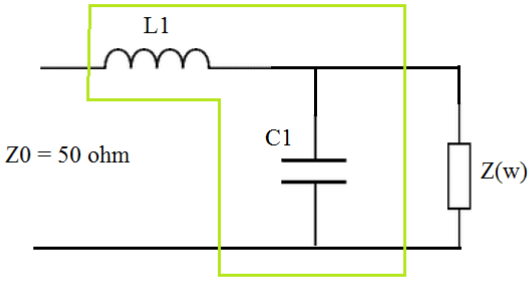

Figure 71: Antenna with a L-Matching Network

The improvement of the impedance matching of the proposed fractal antenna with the addition of a stub on the partial ground plane, can be explained by modeling the stub as an equivalent L-Matching Network, as shown in Figure 71. The value of the inductance (L_1) and capacitance (C_1) at each resonant frequency is determined by the size/shape of the stub and the thickness/permittivity of the substrate. For the proposed antenna, due to the use of the fractal geometry, which has the advantage of self-affinity and exhibiting similar radiation characteristics at multiple resonant frequencies, the impedance matching was improved simultaneously at both resonant frequencies with the addition of an equivalent L-Network. This can be concluded as one additional merit of employing fractals in monopole antenna design. Figure 72 (a) and (b) show the simulated input impedance for the antenna presented in Figure 66 and 70, respectively. The red line with crosses corresponds to the frequency band of 5 - 6 GHz while the blue line represents the 2.3 - 2.8 GHz band. Comparing both figures, it can be found that after adding the stub the impedance match

of both bands are improved especially for the upper band, which broads the bandwidth at 5 GHz band significantly.

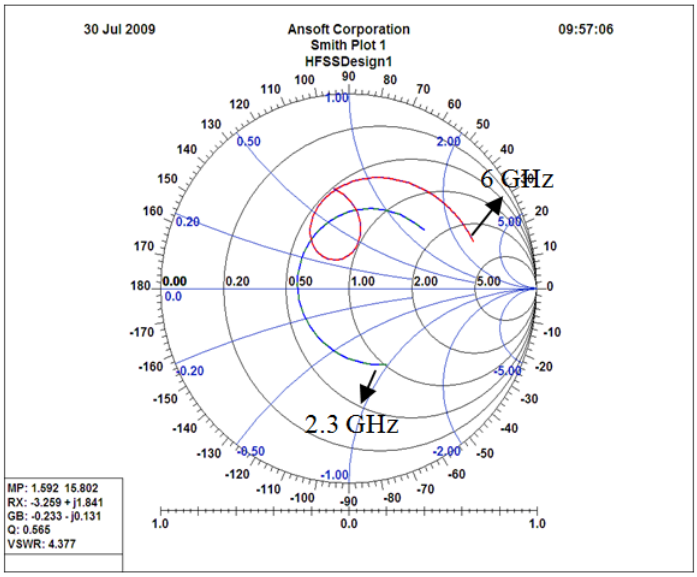

(a)

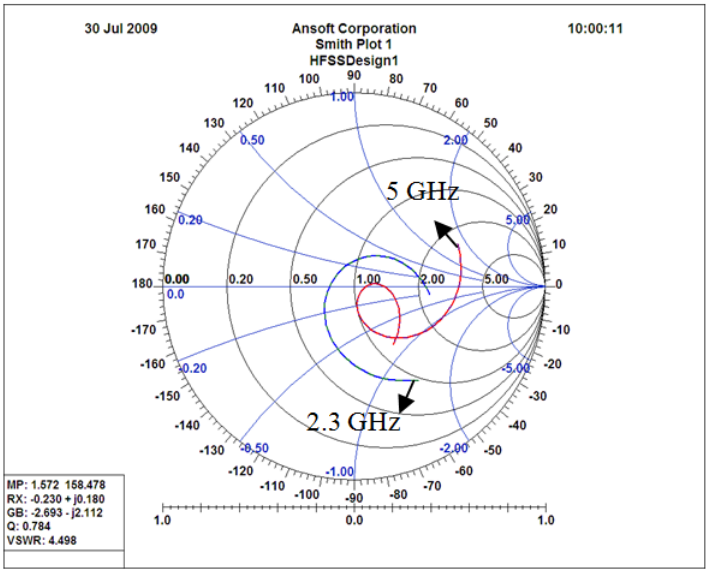

(b)

Figure 72: The simulated input impedance of the fractal monopole array: (a) without using the proposed impedance match method; (b) with the rectangular stub on the ground plane

3.7.3 *Simulated and Measured Results*

Figure 73 presents the measured return loss of the two printed fractal monopole antenna arrays shown in Figure 66 and 70. The measurement results confirm that after introducing a rectangular stub on the top edge of the ground plane, the return loss of the proposed printed monopole array can be improved with little effect on the original resonant frequencies. After applying the proposed impedance matching method, the bandwidth at the lower band is increased by around 50% and the bandwidth at the higher band is almost doubled. The measured return loss shows that this 2nd prototype can operate from 2.31 to 2.52 GHz and from 5 to 5.33 GHz, which covers the desired frequency bands for 802.11 b/g wireless standards.

Figure 74 (a) shows the simulated 3D radiation pattern of this antenna array. Compared to the radiation patterns of the fractal antenna that only uses one radiation element, which is presented in Figure 74 (b), the radiation patterns of this single feed fractal array are more directive and as a result, the directivity of this antenna at both bands is improved by at least 2 dBi.

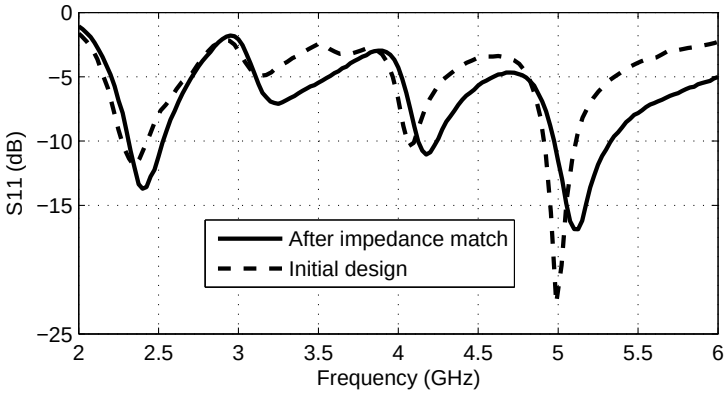

Figure 73: The measured S11 of the fractal monopole antenna array with-/out the proposed impedance matching method

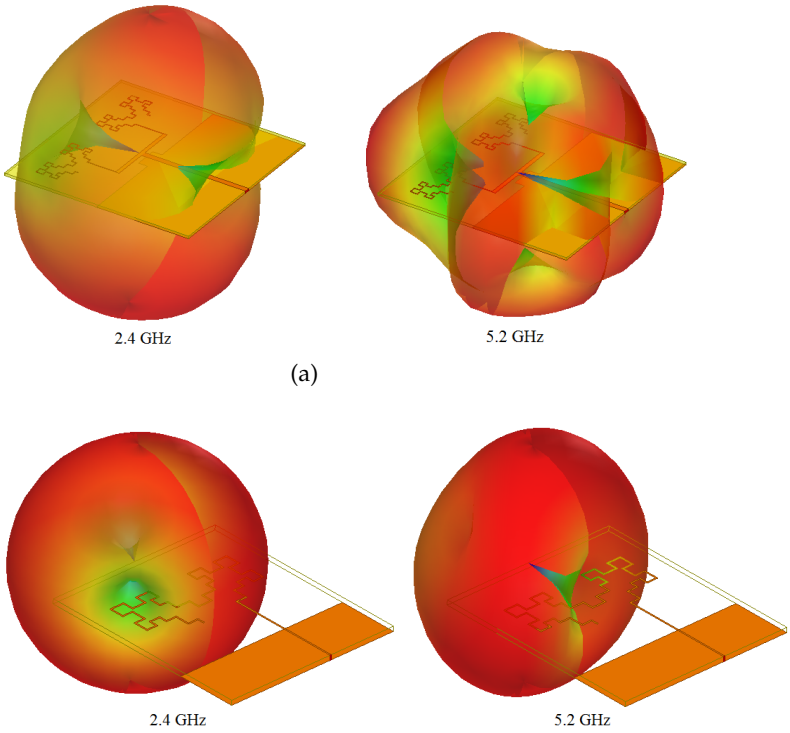

Figure 74: Simulated 3D radiation pattern of the: (a) single feed fractal antenna array; (b) single fractal antenna

3.7.4 *Proposed Antenna on a PDA Size Substrate*

The proposed fractal monopole array was also designed on a PDA size substrate of 112 mm long and 65 mm wide. In order to achieve better antenna performances, numerical simulations were done in Ansoft HFSS to optimize the size of the stub on the ground plane. Figure 75 shows top and side view of the final antenna structure. Figure 76 shows the measured and simulated return loss of this design. It can be observed that after optimization, it is possible to further increase the operating bandwidth of the antenna: it has a 10 dB bandwidth from 2.32 to 2.49 GHz and from 5.1 to 5.88 GHz, which covers the required 2.4, 5.2 and 5.8 GHz bands for 802.11a/b/g applications. Comparing the measured and simulated results, some frequency shifts were observed, which might be caused by the fabrication accuracy or numerical simulation error. By adjusting the size of the fractal geometry, the resonant frequencies can be easily tuned to the desired ones.

Figure 77 (a), (b), (c) show the measured radiation patterns (both E-and H-plane) of the proposed antenna on the PDA size substrate at 2.4, 5.2 and 5.8 GHz, respectively. It can be seen that in the lower band, the radiation pattern of this antenna array is similar to a normal printed monopole antenna, which has a isotropic radiation pattern at

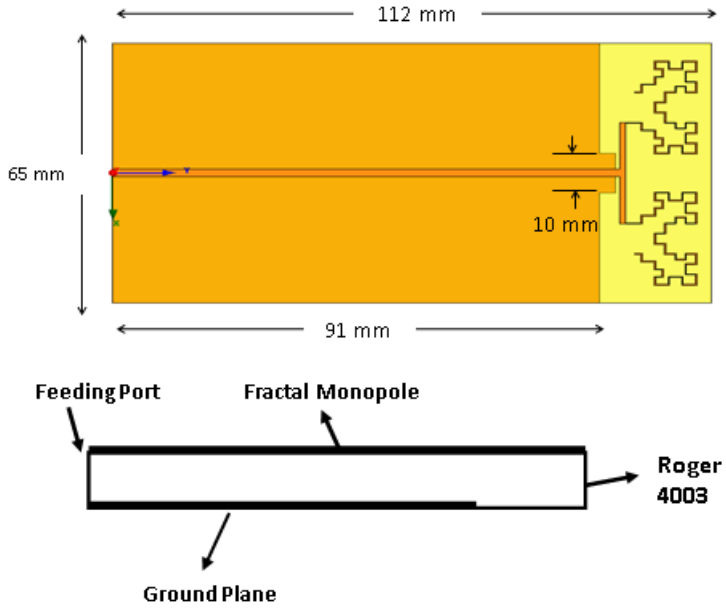

Figure 75: Top and side view of the proposed fractal monopole array on a PDA size substrate

the H plane and two broadside radiation pattern at the E plane. In the upper band, the radiation patterns at both 5.2 and 5.8 GHz are more or less omnidirectional but there are some nulls in the E plane, which are due to the cancellation from the two radiation elements. The measurement results also indicate that the maximum gain of this printed monopole array can reach 2.3 dBi in the lower band and 5.6 dBi in the upper band. Compared to the case of a single radiation element, a minimum of 2 dB gain improvement has been achieved. Based on the simulation results, the radiation efficiency of this antenna array is 86% at 2.4 GHz, 82% at 5.2 GHz and 89% at 5.8 GHz.

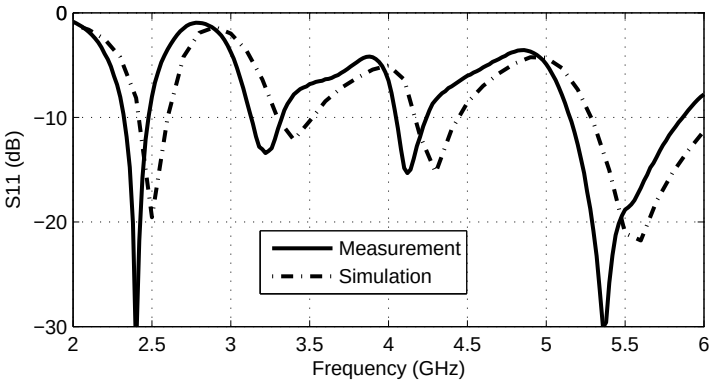

Figure 76: The measured and simulated S11 of the antenna array on a PDA size substrate

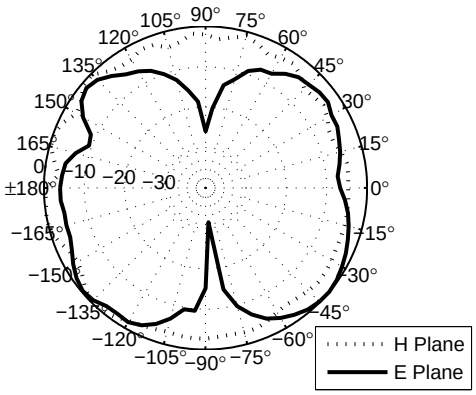

(a) 2.4 GHz

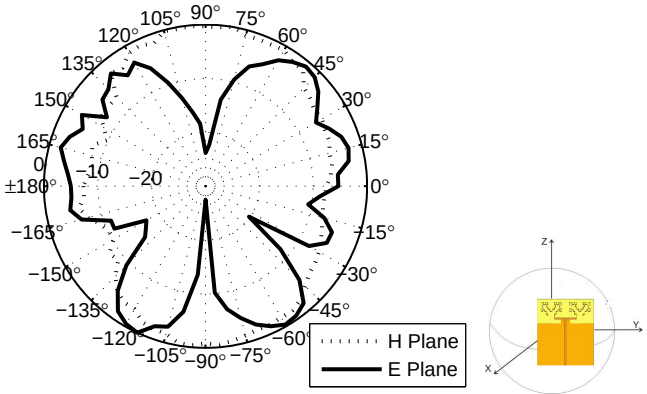

(b) 5.2 GHz

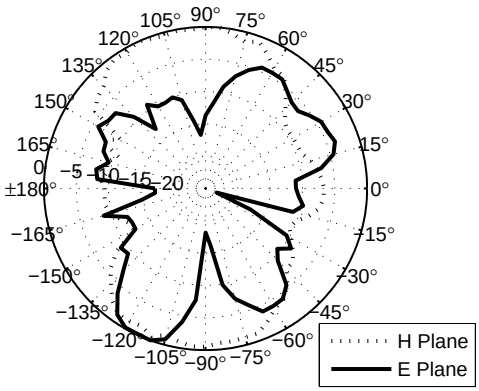

(c) 5.8 GHz

Figure 77: Measured radiation patterns of the proposed fractal array on the PDA size substrate. The solid line represents measured results on X-Z Plane (E-Plane) while dashed line represents measured results on X-Y plane (H-plane)

3.7.5 *Conclusion*

A single feed multiband printed fractal monopole antenna array that uses the 2nd iteration of the Minkowski geometry was designed for WLAN applications. It is found that by adding a rectangular stub

on the edge of the partial ground plane, the impedance match at both bands (2 and 5 GHz) can be improved with little influence on the original resonant frequencies, which has been confirmed by both simulation and experiment results. Moreover, the proposed antenna geometry was designed on a PDA size substrate. The experimental results show that this antenna has wide operation bandwidth in both bands and has a 2 dB gain improvement compared to the antenna with only one radiation element.

3.8 SUMMARY OF THE CHAPTER

In this chapter, the fractal techniques have been employed to the design of compact multiband printed monopole antennas. A set of MATLAB functions were developed to aid the modeling of fractal structures in Ansoft HFSS. This methodology utilizes recursive functions to calculate the coordinates of each node of the fractals and then write a *vbs* file that can be executed by the EM simulation software to create fractals in simulation environment with required physical dimensions. Then, based on this tool, three multiband fractal monopole antennas, one fractal-based Inverted-L antenna and one single feed fractal monopole antenna array are proposed, all of which were designed for the dual or triple bands WLAN application. The experimental results confirm the advantages of fractal antennas: compact size, multi-frequency operation and wide operation bandwidth. The publications resulted from the work presented in this chapter are:

1. Qi Luo; Jose Pereira and Henrique Salgado. Inverted-L Antenna (ILA) Design using Fractal for WLAN USB Dongle. I*n Proceedings of Conference on Electronics, Telecommunications and Computers*, Lisbon, Portugal, November 2011.

2. Q. Luo; H.M. Salgado and J.R. Pereira. Printed Fractal Monopole Antenna Array For WLAN. In *Proceedings of International Workshop on Antenna Technology (iWAT)*, Lisbon, Portugal, March 2010.

3. Q. Luo; J.R. Pereira and H. Salgado. Fractal Monopole Antenna For WLAN USB Dongle. In *Proceedings of Loughborough Antennas and Propagation Conference*, vol. 1, pp. 245-247, Loughborough, UK, November 2009.

4. Q. Luo; H. M. Salgado and J. R. Pereira. Fractal Monopole Antenna Design Using Minkowski Island Geometry. In *Proceedings of IEEE International Symposium on Antennas and Propagation*, Charleston, United States, June 2009.

4

ELECTRICALLY SMALL ANTENNA DESIGN USING CHIP INDUCTOR

4.1 INTRODUCTION

Besides using fractal techniques to design antenna of reduced size, another technique that has been implemented in this thesis work is to introduce a lumped element, more specifically a chip inductor, into the antenna radiation element. In this way, the effective electrical length of the printed monopole is increased by an actual chip inductor instead of employing the fractal geometries that can bend a microstrip line of large length in an area of small size.

The objective of this chapter is to use this new technique to design electrically small size antennas. Therefore, before presenting the proposed antennas, the concept of electrically small antenna and the trade-off between the antenna size reduction and antenna radiation performance is introduced in Section 4.2. Then, based on studying the equivalent model for the chip inductor, a design procedure regarding to how to build an appropriate chip inductor simulation model in HFSS is presented in Section 4.3. After that, Section 4.4 and 4.5 presents two proposed electrically small monopole antennas for dual band WLAN applications. A brief summary of this chapter is given in Section 4.6.

4.2 PHYSICAL LIMITATIONS OF ELECTRICALLY SMALL ANTENNA

The definition of the electrically small antenna was first given by Wheeler in 1947. In his work [61], the electrically small antenna is considered as one antenna whose maximum dimension is less than the radian-length, which is $1/2\pi$ of the wavelength. Similar definition were also given by [62]. In several of his works [49, 63], Steven Best make a more clear explanation of this definition as:

$$ka < 0.5 \tag{89}$$

where a is the radius of sphere that can enclose the maximum dimension of the antenna as shown in Figure 78 and k is the wavenumber, which equals:

$$k = 2\pi/\lambda \tag{90}$$

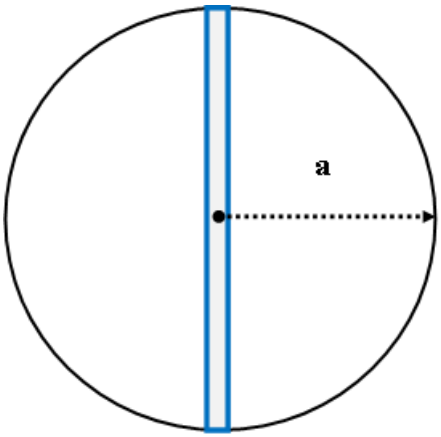

Figure 78: A dipole antenna enclosed in a sphere with radius of a

According to [61], the antenna within this size limit can be made to behave as a lumped capacitor or inductor and the fundamental limitation on the bandwidth and the efficiency of a small antenna is related to the radiation power factor, p_e or p_m, which can be represented by

$$p_e = \frac{G_e}{wC} \tag{91}$$

when the antenna is made to behave as a lumped capacitor or by

$$p_m = \frac{R_m}{wL} \tag{92}$$

when it behaves as a inductor, where G_e is the radiation conductance in parallel with antenna, R_m is the radiation resistance in series with antenna, w is the radian frequency, C is the capacitance of antenna and L is the inductance of the antenna.

The limitations of the electrically small antennas was also investigated by Chu [64]. By investigating the equivalent circuit models for an electric dipole and employing the TM and TE spherical wave modes, the limits of quality factor (Q) of an antenna was calculated and shown to be inversely proportional to the size of the antenna. Assuming there is one equivalent circuit that gives a good approximation to the antenna and it has fixed values at antenna's operation frequency, according to the study presented in [65], the bandwidth of the antenna can be related to the Q as:

$$Bandwidth = \frac{1}{Q} \tag{93}$$

The equation is relatively accurate when $Q \gg 1$. When $Q < 2$, this equation fails to provide a precise results. However, the relationship between bandwidth and Q still stands, which means that the bandwidth of one antenna is always inversely proportional to its Q. The minimum value of Q that one antenna can exhibit was further stud-

ied in [66] and in this study a formula to calculate the lower bound of the quality factor was derived:

$$Q_{lb} = \left[\frac{1}{(ka)^3} + \frac{1}{ka}\right] \tag{94}$$

Equation 94 gives the lower bound of the Q factor for a linearly polarized antenna and it agrees with the calculation results using Chu's equivalent circuit model. The exact value of the Q of one antenna can be calculated using the expression given in [67]:

$$Q(\omega_0) = |\frac{\omega_0}{2R_0(\omega_0)}X_0^{'}(\omega_0) - \frac{2\omega_0}{|I_0|^2R_0(\omega_0)}[W_L(\omega_0) + W_R(\omega_0)]| \tag{95}$$

where w_0 is the radian frequency, I_0 represents the current propagated on the antenna, $W_L(\omega)$ is the energy lost on the antenna and $W_R(\omega)$ is the energy radiated by the antenna. $R(\omega)$ and $X(\omega)$ are the real part and imaginary part of the complex input impedance of the antenna, respectively. Through some mathematical manipulation, [67] simplified Equation 95 into the following equations:

$$Q(\omega_0) = \frac{2\sqrt{\beta}}{FBW_v(\omega_0)} \tag{96}$$

where

$$FBW_v(\omega_0) = \frac{\omega_+ - \omega_-}{\omega_0} \tag{97}$$

$$\sqrt{\beta} = \frac{s-1}{2\sqrt{s}} \tag{98}$$

The parameter s is the criterion for the maximum VSWR and ω_+, ω_-, ω_0 represent the higher frequency bound, lower frequency bound and central frequency of the antenna, respectively. This gives a good approximation of the actual value of the Q at both resonant and anti-resonant frequencies compared to the one given in [64] and has been widely accepted by most researchers. Moreover, the authors in [67] redefined a more accurate formula to calculate the lower bound of the quality factor of the antenna by introducing the radiation efficiency η_r:

$$Q_{lb} = \left[\frac{1}{(ka)^3} + \frac{1}{ka}\right]\eta_r \tag{99}$$

As can be seen from the above equations, the antenna of smaller size always exhibits a higher quality factor. However, the bandwidth of an antenna is inversely proportional to the value of quality factor, which means that the size reduction of one antenna will lead to a narrow band antenna design. Although introducing losses to the

resonant structure can improve the bandwidth of the antenna, this will decrease the antenna radiation efficiency. Therefore, it can be concluded that there is a trade-off between the size reduction of the antenna and its radiation performance. In the following sections, the quality factors of the proposed electrically small antennas are calculated using Equation 96 and compared to their responding quality factor lower bounds (Equation 99), to examine the effectiveness of embedding the chip inductor in the antenna structure to the design of electrically small antennas.

4.3 SIMULATION MODEL OF CHIP INDUCTOR

This section presents the methodology considerations of introducing the chip inductor into the antenna design. As the objective of this part of investigation is to introduce the chip inductor into the antenna design, it is important to build an adequate model for the chip inductor during the antenna simulation in order to obtain an accurate prediction of the antenna radiation performances. The chip inductor, Coilcraft 0402HP, was chosen to be studied as an example and Figure 79 shows the equivalent lumped element model for this chip inductor from its data sheet [68].

Figure 79: The equivalent circuit structure of the chip inductor

As can be seen from this figure, a packaged chip inductor contains series and parallel resistors as well as parallel capacitors. According to the data sheet, the Resistance R_{VAR} varies with frequency according to:

$$R_{VAR} = k \times \sqrt{f} \tag{100}$$

where k is a constant and the f is the frequency in Hertz (Hz). Values for k and for the rest of the lumped elements can be found on the data sheet of the Chip inductor. By mathematically solving the circuit, the expression of the total impedance can be found to be:

$$Z = R_2 + \frac{(R_1 - j/wc_1)(R_{VAR} + jwL)}{(R_1 + R_{VAR}) + j(wL - 1/wc_1)} \tag{101}$$

The equivalent circuit structure of the chip inductor can be simplified to the one shown in Figure 80 by mathematically fitting the equivalent impedance of both networks and allowing the resistance and inductance of the simple model to be frequency dependent. This

simplified RL model can be easily included in the EM simulation environment for antenna simulation by assigning a RLC boundary condition. The simplified circuit is equivalent to the original one, only if the values of the resistance (R) and inductance (L) are allowed to change with frequency, because of R_{VAR}'s dependence with frequency.

Figure 80: Simplified equivalent circuit structure of the chip inductor

By equating Equation 101 to the equivalent impedance of the simplified circuit, the expressions of the series resistance $R(f)$ and inductance $L(f)$, which are a function of frequency, can be expressed as:

$$R(f) = \frac{E \times A + D \times B + A \times L/C_1}{A^2 + B^2} + R_2 \tag{102}$$

$$L(f) = \frac{D \times A - B \times (R_1 R_{VAR} + L/C_1)}{w \times (A^2 + B^2)} \tag{103}$$

where

$$A = R_1 + R_{VAR} \tag{104}$$

$$B = w \times L - \frac{1}{wC_1} \tag{105}$$

$$D = w \times L \times R_1 - \frac{R_{VAR}}{w \times C_1} \tag{106}$$

$$E = R_1 \times R_{VAR} \tag{107}$$

$$w = 2\pi f \tag{108}$$

The chip inductor used in the proposed antennas, which will be presented later, was Coilcraft 0402HP-20N series model with inductance of 20 nH and size of only 1.12 mm $\times$ 0.66 mm. According to the data sheet of this inductor provided by Coilcraft, for the 0402HP series the value of k is $5.63 \times 10^{-5} \Omega . \mathrm{Hz}^{1/2}$ and the values for the parallel resistance R_1, series resistance R_2, parallel capacitance (C_1) and inductance (L) are 18 Ω, 0.155 Ω, 0.038 pF and 20 nH, respectively. Figure 81 shows the calculated series resistance $R(f)$ and inductance $L(f)$ against frequency using the above equations. It is observed that up to 2 GHz, this inductor has relatively constant inductance and low

serial resistance. However, at higher frequencies, both values increase rapidly specially the resistance.

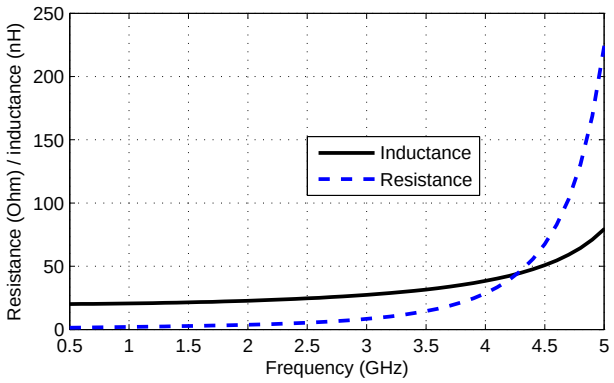

Figure 81: The value of equivalent series resistance and inductance of the chip inductor (Coilcraft 0402HP-20N) against frequency

Equation 101 has also been used to calculate the equivalent impedance of another chip inductor from Coilcraft, 0302CS-20NX, for the purpose of comparison. Figure 82 shows the calculated values of $R(f)$ and $L(f)$. By comparison, it is found that this chip inductor behaves similarly to the Coilcraft 0402HP-20N, except that the variation of the series inductance $L(f)$ against frequency is slightly larger in the higher frequency band (Figure 83).

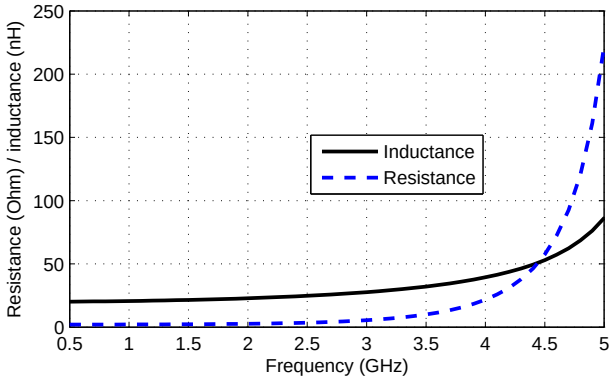

Figure 82: The value of equivalent series resistance and inductance of the chip inductor (Coilcraft 0302CS-20NX) against frequency

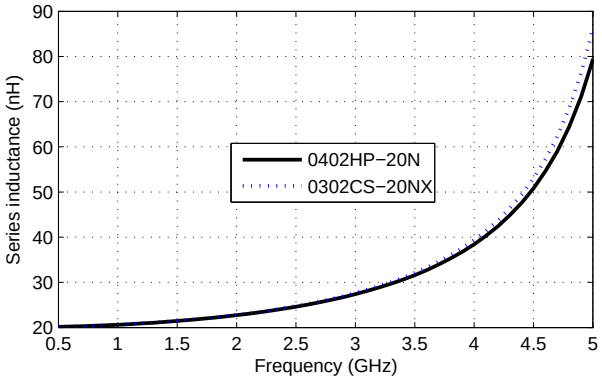

Figure 83: Comparison of the calculated $L(f)$ for both chip inductors

Since the characteristics of the equivalent series resistance and inductance of the chip inductor changes dramatically with increasing frequency, when building the antenna simulation model, the values of the equivalent series resistance and inductance need to be selected at the expected resonant frequency. For example, if the antenna is designed to be resonant at 2.4 GHz and the chip inductor employed is Coilcraft 0402HP-20N, according to Figure 81, the equivalent inductance and series resistance of this chip inductor will be 24 nH and 5 Ω, respectively. Then, these values need to be introduced into the simulation model set-up by assigning a *RLC* boundary condition in the EM simulation software package, as shown in Figure 84.

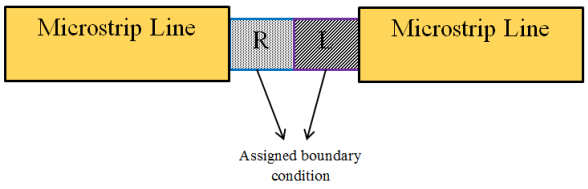

Figure 84: Simulation model of the chip inductor in the EM simulation environment

4.4 COMPACT PRINTED C-SHAPED MONOPOLE ANTENNA WITH CHIP INDUCTOR

4.4.1 *Motivation*

Compact multiband antenna design has attracted much research interests in recent years due to the rapid development of wireless communications and growing needs of small size wireless devices. Different approaches, reported in the literature, have been used to the design of compact antennas. In [69, 70], compact antenna designs have been achieved by either using stacked structures or integrating shorting walls on the radiation elements. In [71, 72], fractal geometries, which have the characteristics of intrinsic self-similarity, were used to design printed planar microstrip antennas with reduced size. In [73], the miniaturization of non-planar and planar dipole antennas using loop loading techniques has been reported. The loop loading, which works as a reactive loading, reduces the resonant frequency of dipole antennas. Moreover, metamaterials (MTM) inspired antennas have also attracted much research interests. There are several research works discussing the use of the unique characteristics of metamaterials to design epsilon negative (ENG) Zeroth-Order or Mu-Zero resonant antennas, infinite wavelength resonant antennas and metamaterial loading antennas [74, 75, 76]. In these work, the resonant frequency of such antennas are mainly dependent on the metamaterial unit cells instead of their physical size.

Recently, embedding capacitors or chip inductors into the printed antennas has also been studied. In [11], a compact loaded multiband PIFA was designed by connecting two parts of the antenna using a capacitor. In [13, 14], a chip inductor was embedded in the printed monopole antenna as a mean to achieve a small size design for wireless wide area network (WWAN) applications in mobile phones. One advantage of using chip inductors in antenna design is that it can effectively reduce the size of the antenna with little influence on its radiation performance. However, there is still not much research in this related field. Moreover, so far there has not any work that studies the characteristics and simulation model of the chip inductor in the field of antenna design.

In this work, the technique of introducing chip inductor into the antenna design is further investigated. The proposed antenna has a C-shaped geometry and its parameters including the location of the chip inductor were optimized in order to make it operate at the desired WLAN dual frequency band. The antenna is designed and simulated based on the methodology proposed in Section 4.3.

4.4.2 *Antenna Design*

The proposed printed monopole antenna has a C-shaped geometry. As will be presented later, by suitably choose the length of each arm, the antenna can be made to have two resonant frequencies. Figure 85 (a), (b) and (c) shows the top view, back view and side view of the proposed C-shaped monopole antenna. The antenna element is printed on the top side of the substrate while the ground plane is located at the bottom side. Behind the radiation elements, there is no ground. This antenna is designed on substrate Roger 4003 with thickness of 0.813 mm and relative permittivity of 3.38. The chip inductor, Coilcraft 0402HP series with inductance of 20nH, is embedded on the top of the C-shape element (see L_3 in Figure 85 (a)). The antenna occupies a space of 15mm $\times$ 8.6 mm and the total size of this antenna including the ground plane and feeding line is $15mm \times 35mm$. To achieve a better impedance match in both bands, the length and width of each branch of the antenna elements are optimized by performing numerical simulations in Ansoft HFSS. The values of the parameters shown in Figure 85 are given in Table 2, where w_2, w_3, w_4 and w_5 represent the corresponding width of each microstrip branch.

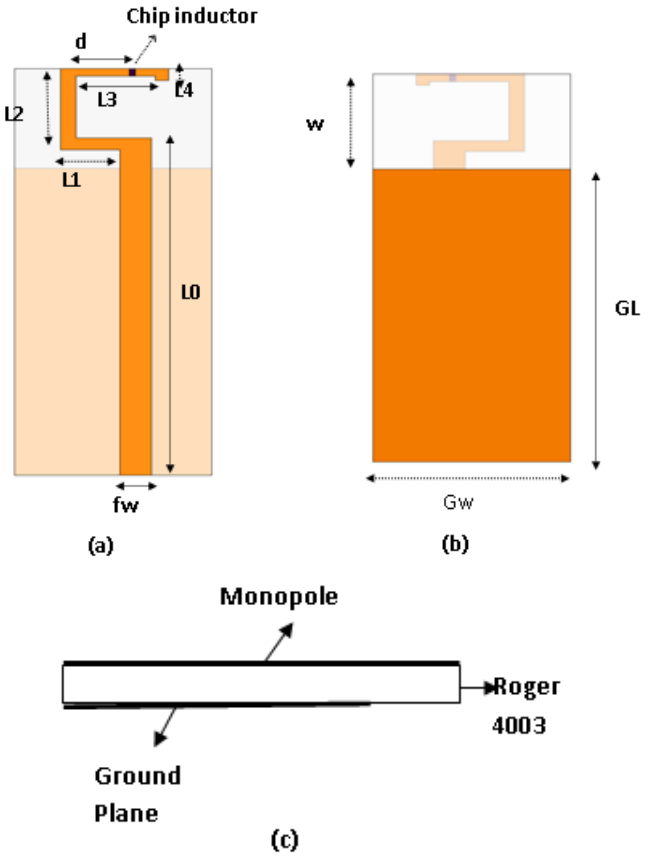

Figure 85: (a) Top view, (b) Back view and (c) Side view of the proposed C-shaped monopole antenna with embedded chip inductor

Table 2: Parameters of the proposed antenna

Parameter	Value (mm)
GL	26.4
Gw	15
w	8.6
fw	2.4
d	4
Lo	28
L1/w1	4.5 / 1
L2/w2	6 / 1.2
L3/w3	7 / 0.65
L4/w4	0.35 / 1

The simulation model of the chip inductor is built based on the studies from Section 4.3, which contains one series resistor and inductor. As in the simulation model, the values of the series resistance $R(f)$ and inductance $L(f)$ can only be constant; so they need to be calculated at one single frequency. The values at 2.4 GHz were selected because this lower resonant frequency is determined by both the overall length of the C-shaped structure and the chip inductor. Based on the calculation results using the equations suggested in Section 4.3, the chip inductor was modeled in Ansoft HFSS by assigning a RLC boundary condition with a series resistance of $5\,\Omega$ and a inductance of 24 nH.

4.4.3 *Simulated and Measured Results*

Figure 86 presents the simulated current distribution of the proposed C-shaped antenna at 2.4 and 5.2 GHz. From this figure, it can be seen that at the lower frequency band, there is a strong surface current on $L_1 + L_2 + L_3 + L_4$ and at the higher band, the current is mainly concentrated on $L_1 + L_2$. This means that the lower resonant frequency is related to the overall length of the antenna and the higher resonant frequency is mainly influenced by branch L_1 and L_2.

Figure 87 presents the simulated return loss of the proposed antenna with different lengths of L_3 or L_4 and Figure 88 shows the simulated return loss of the same antenna with different lengths of L_2. From these simulation results, it is found that changing the length of either L_3 and L_4 only influences the resonant frequency at the lower band. It is also observed that the length of L_2 has the same effect on the resonant frequencies at both lower and higher band. These findings are consistent with the conclusions derived from the observation of the current distributions on the antenna at its resonant frequen-

cies. The radiation performance of the proposed antenna with chip inductor embedded on different positions on the horizontal branch L_3 is also investigated. Figure 89 presents the simulated return loss of the antenna by changing the value of d as indicated in Figure 85. It is found that moving the chip inductor closer to the right end of the antenna element can increase the resonant frequency at the lower band while the resonant frequency at higher band decreases. With these findings, based on the design requirements, the frequency ratio of the proposed antenna can be tuned to the desired value.

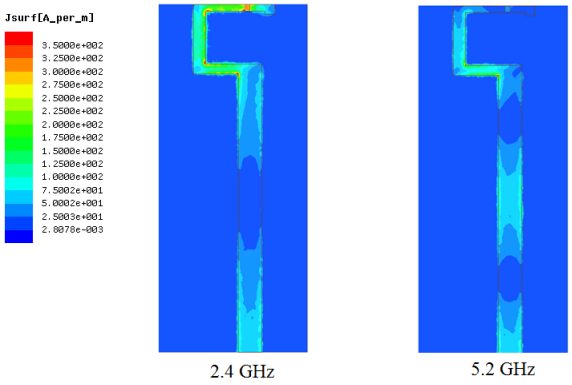

Figure 86: Simulated current distribution of the proposed C-shaped antenna at 2.4 GHz and 5.2 GHz

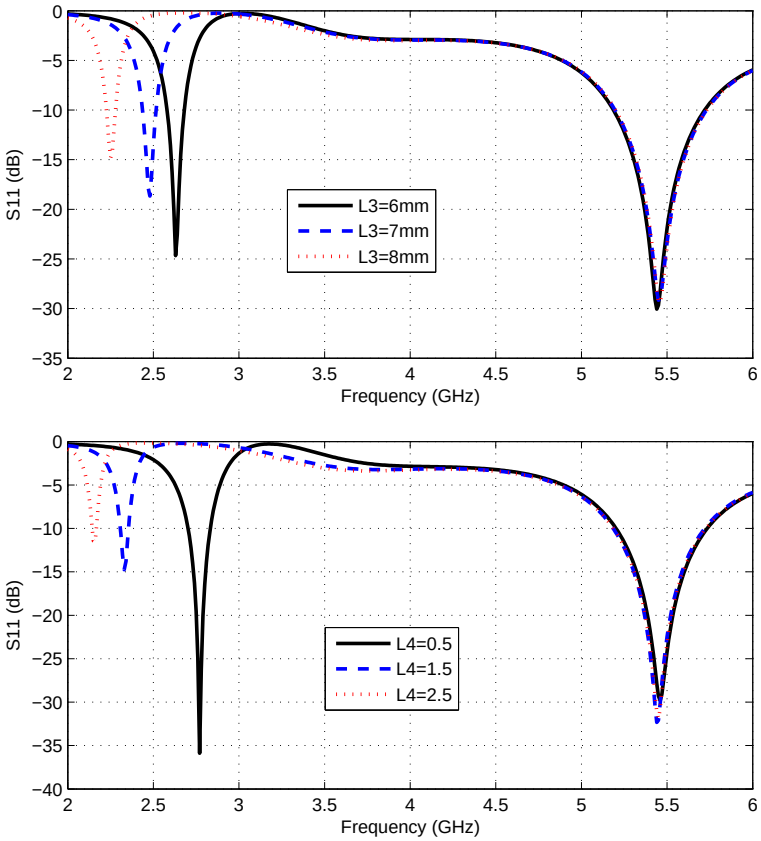

Figure 87: Simulated S11 of the proposed antenna with different length of L_3 and L_4

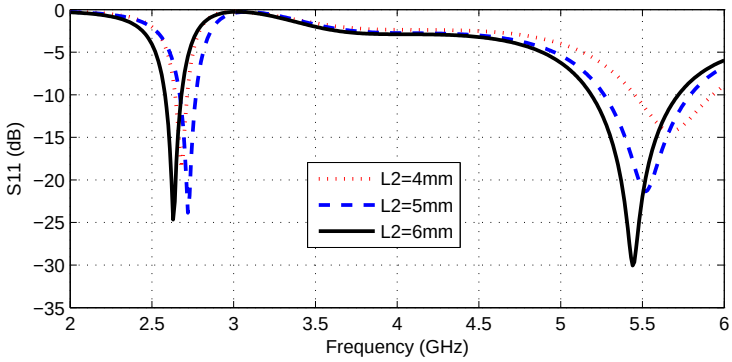

Figure 88: Simulated S11 of the proposed antenna with different length of L_2

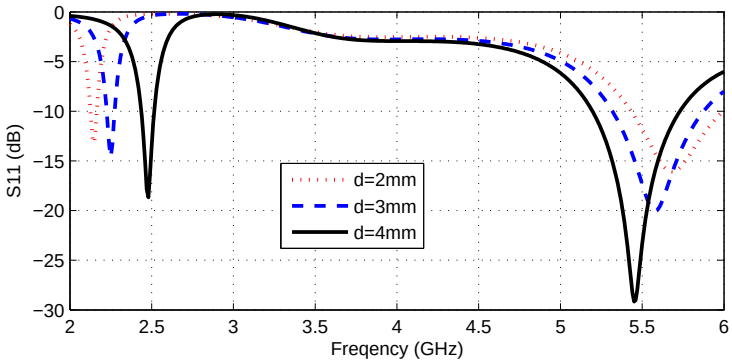

Figure 89: Simulated S11 of the proposed antenna with chip inductor in different locations on arm L_3

Figure 90 compares the simulated and measured return loss (S11) of the proposed monopole antenna. The experimental results show that the proposed antenna has a 10dB return loss bandwidth over 2.55-2.65 GHz and 5.1-5.3 GHz, which is close to our initial design objectives. As can be seen from this figure, there is some disagreement between the experimental and simulated results. The differences between the simulation and measurement results are attributed to the accuracy of the fabrication model and the errors introduced by soldering the chip inductor, which has a small size of only 1.12 mm $\times$ 0.66 mm, to the antenna element. However, from both simulated and measured results, it can be observed that the proposed monopole antenna clearly exhibits two operational bands (S11 < -10dB) at 2 and 5 GHz band. By proper adjustment of the relevant parameters of the antenna, it is possible to make this antenna operate at the desired frequencies for WLAN dual band application.

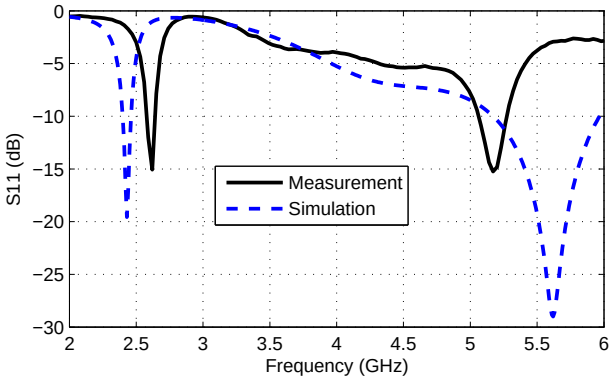

Figure 90: Comparison between the measured and simulated S11

In order to show the effectiveness of embedding the chip inductor in reducing the size of one monopole antenna, one antenna prototype that has exactly the same dimensions as the proposed antenna except that there is no chip inductor in the antenna, was fabricated. Figure 91

compares the measured return loss of the two antennas: the proposed antenna with chip inductor and the one without the chip inductor. From Figure 91, it can be seen that without the chip inductor, the monopole antenna only resonates at 4.15 GHz. After adding the chip inductor, this antenna can be made to resonate at 2.6 GHz, which is a frequency reduction of more than 37%. Moreover, another resonant frequency at 5.2 GHz is also observed.

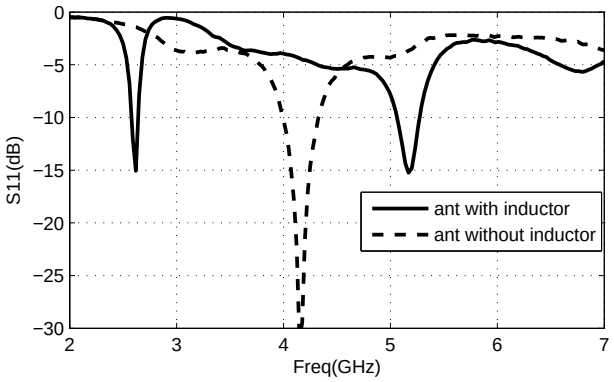

Figure 91: Comparison of the measured S11 between the proposed antenna with and without the chip inductor

It is shown in Figure 89 that the position of the chip inductor has a great effect on both of the resonant frequencies. Therefore, it is suspected that the disagreement between the simulated and measured return loss (Figure 90) might due to the accuracy of the placement of the chip inductor. This assumption has been justified by the EM simulation, in which the position (parameter d) of the chip inductor was moved by 0.5mm. Figure 92 compares the original simulation, the new simulation and the measured return loss. It is observed that with the new simulation model, at the lower frequency band there is a good agreement between the simulated and measured results.

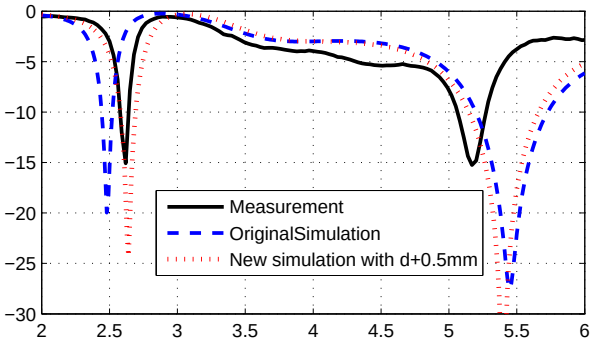

Figure 92: Comparison of the return loss with new simulation model and measured result

However, at the higher band, there is still a big difference between the simulation and measurement results. This is due to the fact that as discussed in Section 4.3, the equivalent series inductance and resistance of the chip inductor varies with frequency. In the proposed simulation model, the values assigned to the chip inductor simulation model (Figure 84) were calculated at the lower resonant frequency as the chip inductor has more impact on the lower band. In this proposed antenna structure, the current paths at each resonant frequency are not independent: they both share the section $L_1 + L_2$. For the higher resonant frequency, the chip inductor behaves as a high resistance loading. This means that the chip inductor can actually influence both resonant frequencies, which is the main reason for the inaccuracy in predicting the higher resonant frequency. In next study, Section 4.5, a multi-branch structure will be employed into the antenna design with the same chip inductor. As will be presented later, by making the current propagate independently at each resonant frequency, both resonant frequencies can be predicted accurately.

Figure 93 (a) and (b) shows the measured radiation patterns at both E-and H-plane of the proposed antenna at 2.55 and 5.2 GHz, respectively. At the higher band, this antenna radiates as a normal monopole antenna. However, at the lower band, this antenna does not have an omnidirectional radiation pattern and at its E-plane, the main beam has been tilted by around 30 degrees. This might due to the errors introduced by the measurement set up such as the reflections from the feeding cables with the fact the the proposed antenna has an electrically small size.

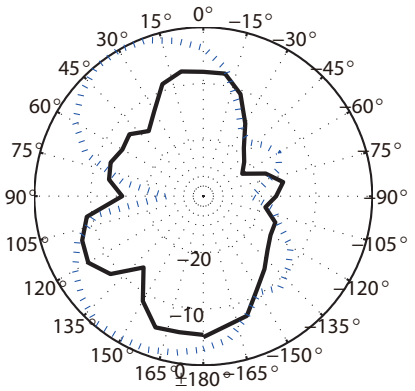

(a)

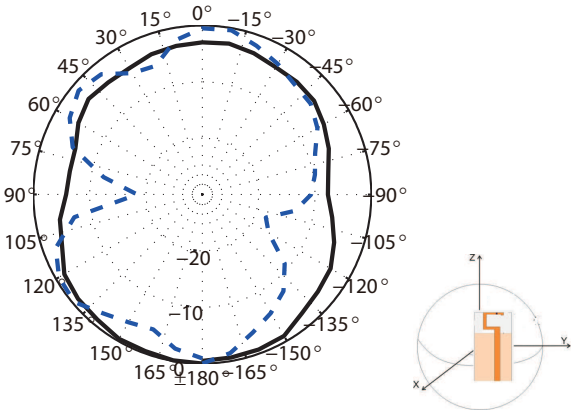

(b)

Figure 93: Measured radiation pattern at X-Y plane (solid line) and X-Z plane (dashed line) at (a) 2.55GHz and (b) 5.25GHz

Figure 94 (a) and (b) shows the simulated peak gain of the antenna at its lower and higher band, respectively. The simulation results show that the peak gain of the proposed antenna at 2.55 GHz is 2.2 dB while the peak gain at 5.25 GHz is 4.7 dB. From the simulation results, it is also found that the radiation efficiency at both bands is around 90% whilst the radiation efficiency of the antenna without the chip inductor is 98% at its resonant frequency. This means that introducing the chip inductor does not greatly influence the radiation efficiency of the original antenna.

Table 3 shows the calculated quality factor (Q) of the proposed antenna and its theoretical Q lower bound by using the equations suggested in Section 4.2. In this calculation, the frequency range was defined by the standard of VSWR 3:1. From Table 3, it can be seen that the proposed antenna has ka smaller than 0.5, which means that the antenna has an electrically small size. Compared to its Q factor lower bound calculated using Equation 99, the proposed antenna exhibits a quality factor close to it.

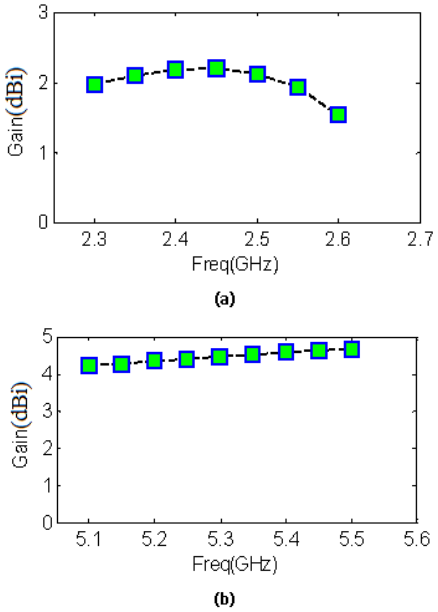

Figure 94: Simulated peak gain of the proposed antenna

Table 3: Calculated Q factor of the proposed antenna

	Proposed Antenna
Frequency (GHz)	2.6
Size ($W_{mm} \times L_{mm}$)	15×8.6
a (mm)	8.65
ka	0.47
Simulated Radiation efficiency (%)	90
Q_{lb}	10.5
3:1 VSWR bandwidth (%)	4.96
Antenna Q	23.3

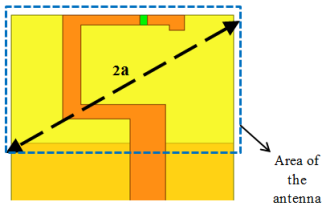

4.4.4 *Conclusion*

In this study, one chip inductor has been embedded into a printed C-shape monopole antenna to design an electrically small antenna for dual-band WLAN applications. With the chip inductor, the size of the antenna was reduced whilst the antenna still maintains good radiation characteristics. Meanwhile, after adding the chip inductor,

the higher mode of the original antenna can also be brought down to a lower frequency, which makes the proposed antenna be able to resonate at the dual frequency bands and simultaneously have a compact size. The measurement and simulation results show that the proposed C-shaped monopole antenna can operate at 2.55-2.65 GHz and 5.1-5.3 GHz with peak gain of 2.2 and 4.7 dBi, respectively. Moreover, according to the simulation results, the radiation efficiency of this antenna at both bands is around 90%.

4.5 COMPACT PRINTED MULTI-ARM MONOPOLE ANTENNA WITH CHIP INDUCTOR FOR WLAN

4.5.1 *Motivation*

In this work, one compact printed monopole antenna with a chip inductor for dual band WLAN is presented. Whereas the antenna presented in Section 4.4 has one arm, the antenna proposed in this section employs a two-armed structure. It is shown in Section 4.3 that the characteristics of the equivalent series resistance and inductance of the chip inductor changes dramatically with increasing frequency, which make it difficult to predict accurately the resonant frequency of the multiband antenna by doing EM simulations. As shown in Section 4.4, the simulation result does not agree well at the higher frequency band. To overcome this problem, a design technique is proposed whereby the antenna structure exhibits independent current paths for each resonant frequency and the inductor is placed in one of the arms to decrease the resonant length of the fundamental mode.

The simplified circuit structure of the chip inductor, which has been proposed in Section 4.3, was introduced into the EM simulation model by assigning a RLC boundary condition. The values of the chip inductor equivalent model are calculated at the lower resonant frequency. With the design strategy that uses the chip inductor to influence only the lower frequency band whilst the other frequency band is created by an independent radiation element, a good agreement between the simulated and measured return loss was reached. The measurement results show that the proposed monopole antenna has a VSWR 2:1 bandwidth over 2.41-2.49 GHz and 5.2-5.6 GHz with omnidirectional radiation patterns. The simulation results indicate that the proposed antenna has a directivity around 1.5 dB in both bands with relatively high radiation efficiency.

4.5.2 *Antenna Structure*

The previous section has shown that the characteristics of the simple RL equivalent circuit of the chip inductor changes considerably at higher frequencies. This promotes the need of using a multi-branch

antenna structure to design a dual band WLAN antenna and only embed the chip inductor in the branch corresponding to the lower resonant frequency at 2.4 GHz. In this way, the resonant frequencies of the antenna are introduced by two relatively independent current paths and the behavior of the chip inductor will not affect significantly the operation in the higher band at 5.2 GHz. In the antenna simulation model, the equivalent inductance and series resistance of the chip inductor were then calculated at 2.4 GHz, and are 24 nH and 5 Ω, respectively.

Figure 95 shows the layout of the proposed printed monopole antenna. This antenna has a two-armed structure and for such monopole antenna the resonant frequency can be created by letting the overall length of each arm approximately to be a quarter of its effective wavelength on the substrate. The chip inductor is embedded in the middle of the left arm and generally speaking, the higher the value of the inductance, the lower the resonant frequency that can be achieved. However, increasing the inductance will also reduce the bandwidth and radiation efficiency of the antenna, which is the reason why a chip inductor with a higher inductance is not chosen in this study. This antenna was printed on a Roger 4003 substrate with relative permittivity of 3.38 and thickness of 0.813 mm. The antenna and ground plane were printed on different sides of the substrate and there is no copper below the antenna section. The area of this antenna is only 10 mm × 10.5 mm, which is only $0.08\lambda_{2.4\text{GHz}} \times 0.084\lambda_{2.4\text{GHz}}$, where $\lambda_{2.4\text{GHz}}$ represents the free space wavelength at 2.4 GHz. The higher band of the antenna is determined by the overall length $L_4 + L_5$, which is approximately a quarter of a wavelength at 5.3 GHz. With the chip inductor, the overall length of $L_1 + L_2 + L_3$, which determines the lower band resonant frequency, is only 12.5 mm. This value is smaller than the length required for conventional monopole antennas. After adding the chip inductor, the resonant frequencies of the lower and higher band can be tuned by respectively changing the length of the arm L_3 and L_5, as demonstrated in the next section. By optimizing the length and width of each arm, this antenna is tuned to resonate at the desired frequencies. The values of the parameters are given in Figure 96, where w_1, w_2, w_3, w_4 and w_5 represent the width of each microstrip branch.

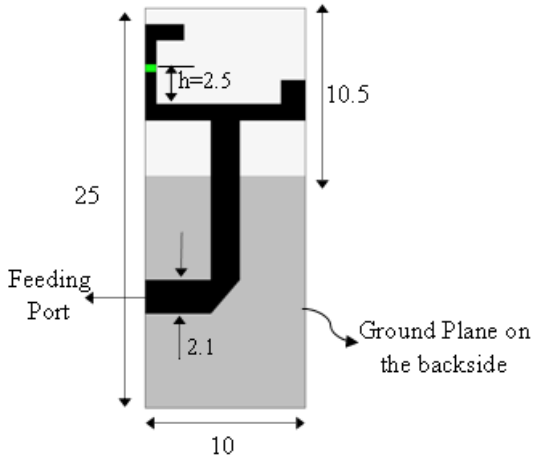

Figure 95: The top view of the proposed multi-arm monopole antenna

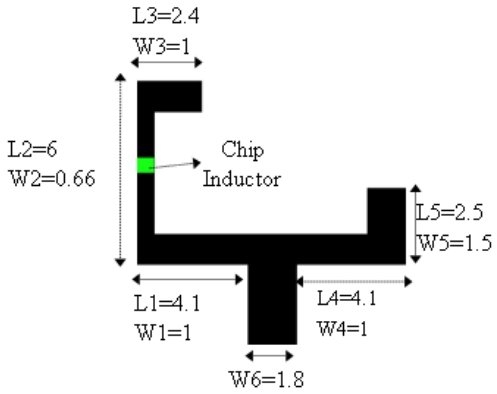

Figure 96: Detailed view of the antenna radiation element with dimensions

4.5.3 *Simulated and Measured Results*

The proposed two-armed monopole antenna was fabricated and the return loss was measured using Agilent PNA E8363B. Figure 97 presents the comparison between the simulated and measured return loss of the antenna. The dashed line represents the simulation results of using the proposed simulation model of the inductor whereas the results based on a simple inductor of nominal value equal to 20 nH are represented by the dotted line. It can be seen that the use of a simple inductor model fails to predict accurately the operation frequency of the antenna. Using the proposed method, there is a good agreement between the measurement and simulation results of the return loss except for the amplitude of the S11 at the higher band. This is due to the fact that in the simulation model, the values of the equivalent series inductance and resistance are chosen at 2.4 GHz. At higher resonant frequency, as shown in Figure 81, the chip inductor acts as a high impedance resistor, which influences the real part of the input impedance of the antenna and as a consequence, the impedance

matching of the antenna at higher band is degraded. However, this just causes a deviation in the amplitude of the return loss while the central frequency of the higher band is still predicted accurately. Measurement results show that the proposed monopole antenna has a -10 dB bandwidth over 2.41-2.49 GHz and 5.2-5.6 GHz.

As stated before, the resonant frequencies of this two-armed antenna can be tuned by respectively varying the length of L_3 and L_5. Some parametrical studies have been conducted and Figure 98-99 show the simulated return loss of the antenna with different values for L_3 and L_5. It can be seen that the length L_3 only influences the resonant frequency of the lower band whereas L_5 only has effect on the higher resonant frequency. Figure 100 shows the simulated return loss with the chip inductor located in different positions. It is found that the position of the inductor only has a major influence on the lower band. For fabrication considerations, the chip inductor was mounted near the middle of the vertical arm (L_2). In general, the design method involves the adjustment of the length L_3 and L_5 after insertion of the chip inductor. The same design method can be applied to tune the resonant frequencies of the antenna with different substrates.

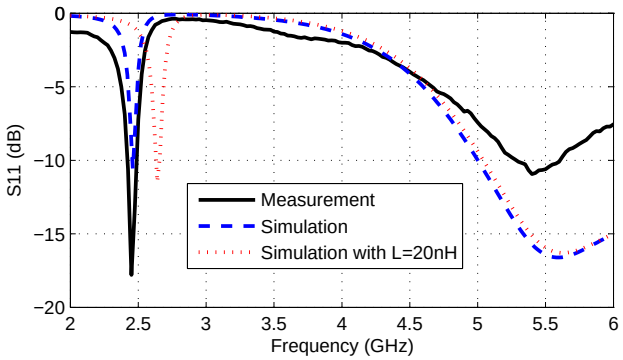

Figure 97: Comparison between the simulated and measured S11 of the proposed antenna

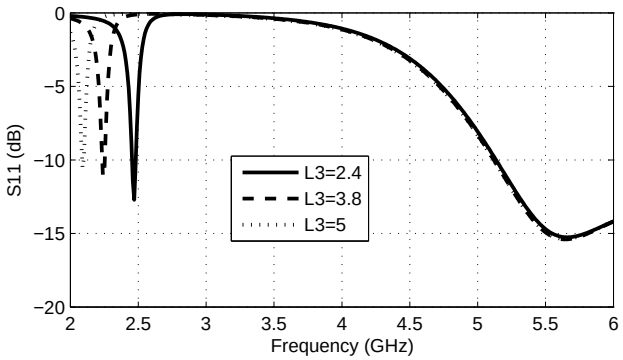

Figure 98: Simulated S11 of the proposed antenna with different length of L_3

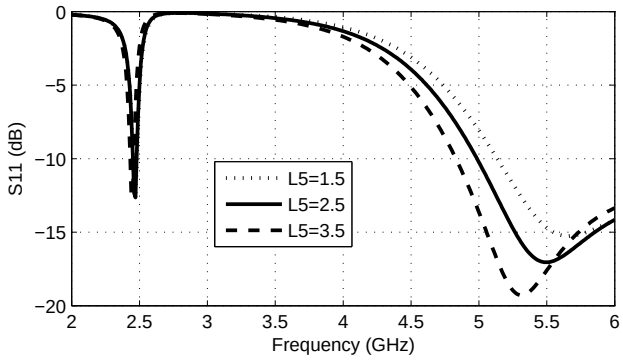

Figure 99: Simulated S11 of the proposed antenna with different length of L_5

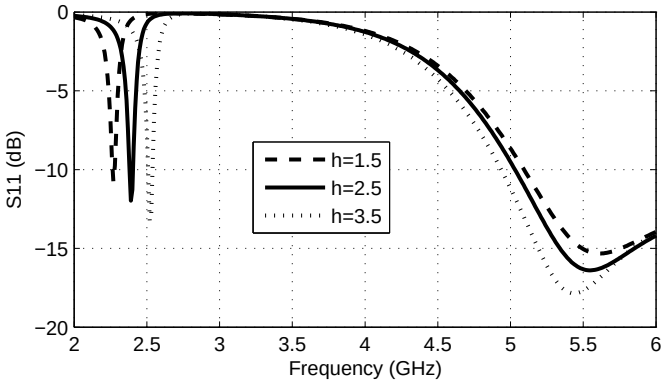

Figure 100: Simulated S11 of the proposed antenna with chip inductor in different positions

Figure 101 shows the simulated surface current distribution of the proposed antenna at each resonant frequency. It can be seen that at 2.4 and 5.3 GHz, the current is mainly concentrated on the left and right branch, respectively.

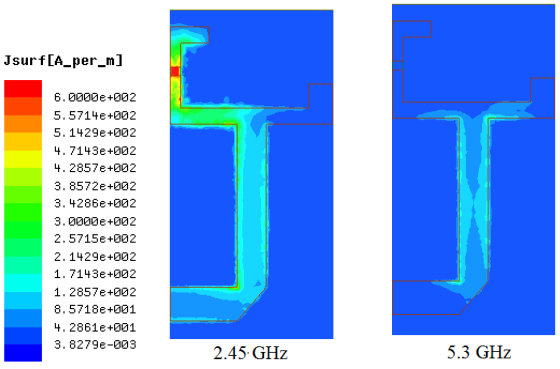

Figure 101: Simulated surface current distribution of the proposed antenna at 2.45 GHz (left) and 5.3 GHz (right)

Figure 102 (a) and (b) present the measured radiation patterns of the two-armed monopole antenna at 2.45 and 5.3 GHz. It can be observed that the antenna has omnidirectional radiation patterns as a typical monopole antenna.

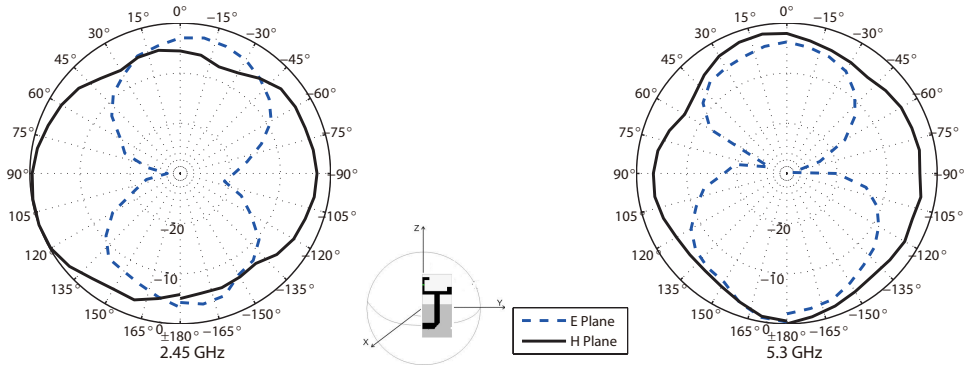

Figure 102: Measured E-plane (X-Z Plane) and H-plane (X-Y plane) radiation patterns of the proposed antenna at 2.45 GHz and 5.3 GHz

The simulated results of the peak directivity and radiation efficiency of the proposed monopole antenna at its lower and higher operation bands are shown in Figure 103 (a) and (b), respectively. It is found that the antenna exhibits a directivity of around 1.5 dB at the lower band and 1.8 dB at the higher band. However, at the lower band the radiation efficiency is around 70%, which is lower than the value at the higher band. This is due to the loss of the resistance inside the chip inductor, which also can be explained as a trade-off between the antenna size reduction and radiation performance. It is also observed that at the lower band, the C-shaped monopole antenna presented in Section 4.4 has radiation efficiency 20% higher than this two-armed monopole antenna. The reason is that in the latter design, the chip inductor was embedded at the position more close to the antenna feeding line, where the surface current is much stronger, as can be seen from Figure 86 and 101. Introducing the chip inductor to the position with higher surface current can lead to more frequency reduction for the antenna; however, the loss from chip inductor increases as well. This explains why the two-armed monopole antenna presented in this study has lower radiation efficiency but more compact size than the C-shaped monopole antenna presented in last section.

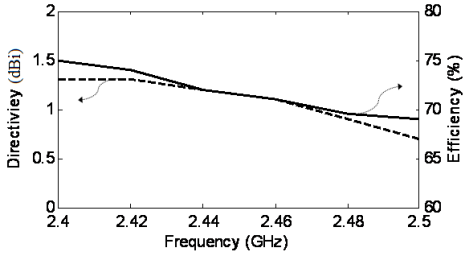

(a)

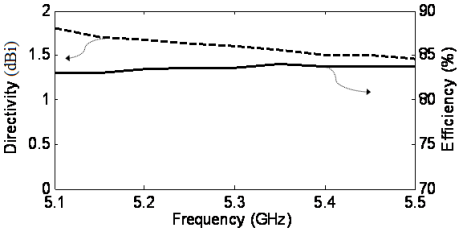

(b)

Figure 103: Simulated peak directivity and radiation efficiency of the proposed antenna at: (a)2.4 GHz band; (b)5.2 GHz band

The quality factor (Q) and electrical size (ka) of the proposed monopole antenna was also studied. The Q factor is calculated following the analysis in Section 4.2. Table 4 shows the calculated results of the proposed monopole antenna. From Table 4, it can be seen that the antenna has ka smaller than 0.5 and has a quality factor very close to its theoretical lower bound.

Table 4: Summary of performance of the proposed printed monopole antenna

Properties	Proposed Antenna
Frequency (GHz)	2.45
Size ($W_{mm} \times L_{mm}$)	10×10.5
a (mm)	7.25
ka	0.37
Radiation efficiency (%)	72
Q_{lb}	15.9
3:1 VSWR bandwidth (%)	5.10
Antenna Q	22.6

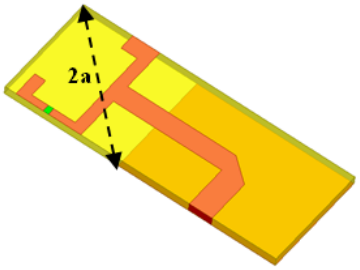

4.5.4 *Conclusion*

In this work, one printed two-armed monopole antenna with an embedded chip inductor has been proposed. This antenna has a compact overall size and can operate at WLAN dual frequency bands (2.4/5.2 GHz). A procedure for including a chip inductor in the design of a compact multiband antenna has been presented. The dual band monopole antenna has been implemented and characterized. The simulation results for the return loss are in good agreement with the measurement. Measurements of the radiation pattern of the antenna were conducted and the measurement results indicate that it exhibits an omnidirectional radiation characteristic as a monopole antenna. By performing a theoretical calculation, it is found that the proposed two-armed antenna structure has an electrically small size and a quality factor close to its theoretical lower bound.

4.6 SUMMARY OF THE CHAPTER

The approach adopted in this chapter is to introduce a chip inductor into the antenna structure for the purpose of antenna size reduction. One challenge of this technique is how to build an appropriate simulation model for the chip inductor during the antenna modeling. This

issue has been solved by investigating the equivalent circuit structure of the chip inductor and simplifying it into a series circuit structure with only one series inductor and series resistor. Based on this study, a design procedure of how to introduce the chip inductor to design a multiband antenna has been proposed. Then, two electrically small antennas for dual band WLAN applications are presented. It is important to point out that although greatly size reduction has been achieved, but there is some reduction in the antenna bandwidth as well as the radiation efficiency especially at the lower resonant frequencies. The following is the list of publications resulted from the work presented in this chapter:

1. Qi Luo; J. R. Pereira and H.M. Salgado. Compact printed monopole antenna with chip inductor for WLAN. *IEEE Antennas and Wireless Propagation Letters*, 10:880-883, September 2011.

2. Qi Luo; Jose Pereira and Henrique Salgado. Compact Printed C-shaped Monopole Antenna With Chip Inductor. In *Proceedings of IEEE International Symposium on Antennas and Propagation*, Washington, USA, July 2011.

5

PRINTED MONOPOLE ANTENNA FOR MULTIBAND MOBILE PHONE APPLICATIONS

5.1 INTRODUCTION

After successfully applying the chip inductor to design two electrically small antennas for dual band WLAN applications and given the need for multiband operation of current mobile devices, it is decided to further investigate this technique to design a compact multiband printed monopole antenna that can operate at multiple frequency bands for a mobile handset.

This chapter is organized as follows. Section 5.2 presents the motivation of this work and the structure of the proposed multiband monopole antenna is depicted in Section 5.3. Then, Section 5.4 presents both the simulated and measured results of the antenna including the return loss and radiation patterns. In this section, the radiation performances of the antenna when it is placed in the plastic housing or with ground planes of different lengths have also been investigated. The radiation performance and the SAR level of the antenna when it is placed in close proximity to the human head are studied in Section 5.5. A brief summary of this chapter is presented in Section 5.6.

5.2 MOTIVATION

The rapid growth in mobile communications increases the needs of designing multiband internal antennas for mobile terminals. Meanwhile, it is also desirable to design such antennas as compact as possible. Planar Invert-F Antenna (PIFA) is one type of conventional antennas that has been widely employed in mobile phones. In [77, 78], two coupled-fed compact multiband PIFAs for wireless wide area networks (WWAN) were proposed for internal mobile phone antenna applications. The size reduction of these two antennas was achieved by shorting the antenna to the ground and bending the antenna structure. Printed monopole slot antennas and printed loop antennas have also been widely studied for multiband internal mobile phones. In [79, 80], two folded monopole slot antennas that can cover the penta-band WWAN operation were proposed for clam-shell mobile phones. These two antennas were designed by making several slots on the top of the ground plane. In [81, 82, 83], printed half-wavelength and meandered loop antenna were proposed for the design of multiband antenna for mobile handsets. However, all of these antennas have

operating bands only covering GSM850/900 and DCS/PCS/UMTS bands, which not enough for nowadays wireless communications.

To make the antenna resonant at additional bands including Wireless LAN, one novel PIFA structure combining shorted parasitic patches, capacitive loads and slots was designed to support both quad-band mobile communication and dual-band wireless local area network (WLAN) operations [84]. Although this antenna can operate at several bands, it is extremely difficult to fabricate due to its complex structure. In [85], multiband operation including the WWAN and WLAN 2.4 GHz was achieved by cutting slots of different lengths at the edge of the system ground plane of the mobile phone. An even more operation bands including GSM/DCS/PCS/UMTS/WLAN/WiMAX were achieved by cutting the loop-like slot on the top of the ground plane and shorting it to the ground plane [86]. However, shorting the antenna to the ground makes the resonant frequencies of the antenna vulnerable to the length of the ground plane and the ground plane size used in [86] is smaller than the size of the system ground plane for a mobile phone. Other techniques have also been developed to design compact multiband antennas for wireless communications. In [87], a multiband antenna that can support WWAN and 2.4 GHz WLAN frequency bands was realized by using a switchable feed and ground. In [88], a small size multiband antenna for wireless mobile system is designed based on double negative (DNG) zeroth order resonator (ZOR). However, it is noticed that these antennas have rather complex structures and they are quite difficult to fabricate. In [13], a chip inductor was embedded in the printed monopole antenna, which resulted in a compact antenna for mobile handset application.

In this work, it aims to continue the studies presented in last chapter and implement the chip inductor technique to design a multi-frequency antenna that can cover most of the required frequency bands for mobile communications. Meanwhile, the antenna proposed has a planar structure and is easy to fabricate, which overcomes most of the shortcomings of previous designs.

5.3 ANTENNA STRUCTURE

Having in mind the limitations of the antennas developed and reported in previous work, this study aims to explore further multiband monopole antennas design with low complexity and suitable for mobile phone applications. From the work presented in the previous chapter, it is concluded that a multi-branch monopole antenna including a chip inductor for size reduction would be a feasible method. In this work, an antenna with multi-branch structure and is capable of resonating at five frequencies is presented. Figure 104 shows the structure of the proposed antenna and the main dimensions of the antenna elements are given in Figure 105. The antenna element is

printed on the top side of the substrate while the ground plane is located at the bottom side. Behind the monopole antenna, there is no ground. The chip inductor, of series Coilcraft 0402HP with an inductance of 20 nH, is embedded between the branch A and B as shown in Figure 105. This antenna has a multi-branch structure, each of which determines different resonant frequencies. The lowest resonant frequency, 960 MHz, is determined by both the inductance of the chip inductor and the overall length of branch A and B. Although the chip inductor can also influence the resonant frequency at 1800 MHz to some extent, this resonance is mainly determined by the length of branch A. The overall length of branch D and the length of branch E determines the resonant frequencies at 2.4 and 5.2 GHz, respectively. The frequency band at 3.8 GHz is related to the length of branch C and the width of branch A.

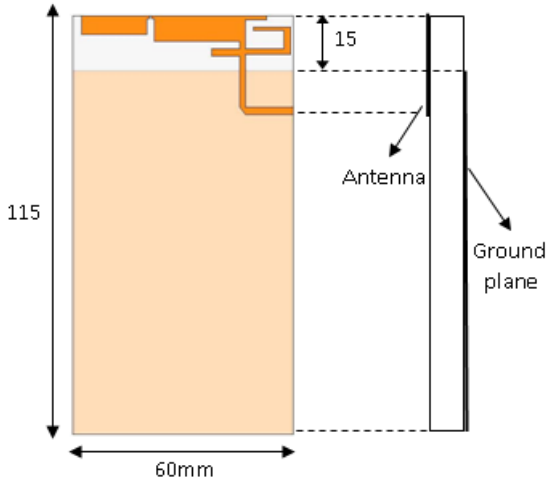

Figure 104: Top and side view of the proposed multiband antenna

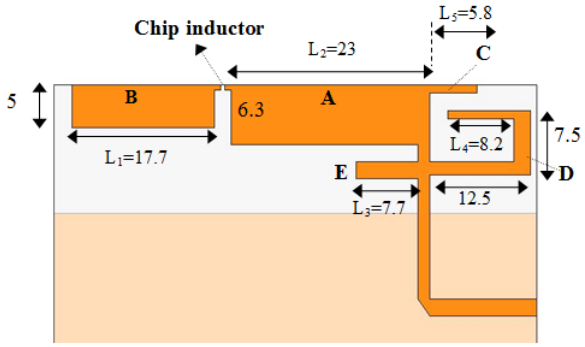

Figure 105: The main dimensions of the proposed antenna

This antenna is printed on the inexpensive substrate FR4 (relative permittivity of 4.4) with thickness of 0.8 mm and size 100 mm × 60 mm, which is a reasonable circuit board size for a PDA or smart phone device. To achieve better impedance matching at each band,

the length and width of each branch of the antenna were optimized by doing numerical simulations in Ansoft HFSS. In the simulation set-up, the model of the chip inductor is built based on the studies presented in Chapter 5. As stated before, the chip inductor mainly influences the first two lower frequency bands. In these two lower frequency bands, the value of the chip inductor is more critical in determining the lowest resonant frequency; as a result, in the simulation set-up, the equivalent inductance and series resistance of the chip inductor model were calculated at 960 MHz, and are 20.6 nH and 2 Ω, respectively.

5.4 SIMULATED AND MEASURED RESULTS

Figure 106 shows the measured and simulated return loss of the proposed antenna. This antenna was measured using the network analyzer Agilent PNA E8363B. It can be observed that there is a good agreement between the measurement and simulation results. The experiment result shows that the proposed antenna has 3:1 VSWR bandwidth covering 860-1060 MHz, 1710-2067 MHz, 2360-2500 MHz, 3250-4625 MHz, 5080-5410 MHz, which includes almost all the required frequency bands for GSM900 (890-960MHz), DCS (1710-1880MHz), PCS (1850-1990MHz), UMTS (1920-2170MHz), WLAN dual band (2400-2484/5150-5350MHz) and WiMAX (3400-3600MHz) operations.

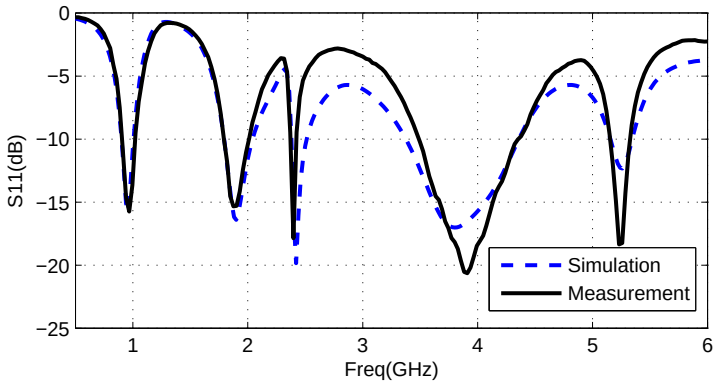

Figure 106: The comparison between measured and simulated S11 of the proposed antenna

Figure 107 presents the comparison of the simulated return loss between the proposed antenna with and without the embedded the chip inductor. It is found that without the chip inductor, at the lowest frequency band the antenna can only resonate at around 1.1 GHz. After introducing the chip inductor, this resonant frequency reduces to 960 MHz and also brings down other higher modes to become resonant at 1.8 GHz. It is also observed that the chip inductor has little influence on the resonant frequencies at 2.4 and 5.2 GHz.

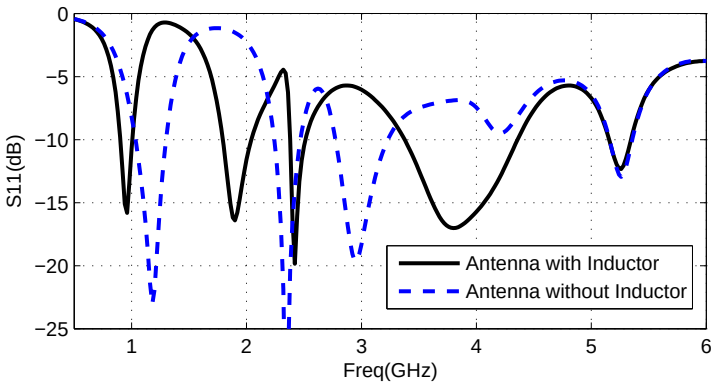

Figure 107: The comparison between the simulated S11 of the proposed antenna with and without the chip inductor

Figure 108 shows the simulated surface current distribution of the proposed antenna at each operation frequency. It is observed that at 960 MHz, there is a strong current on branches A and B. At 1800 and 1900 MHz, the current is mainly distributed on branch B. It is also clear that branches D and E are responsible for the resonant frequency at 2.4 and 5.2 GHz, respectively. Regarding the resonance at 3.8 GHz, it is mainly determined by branch C and the coupling between branch C and D.

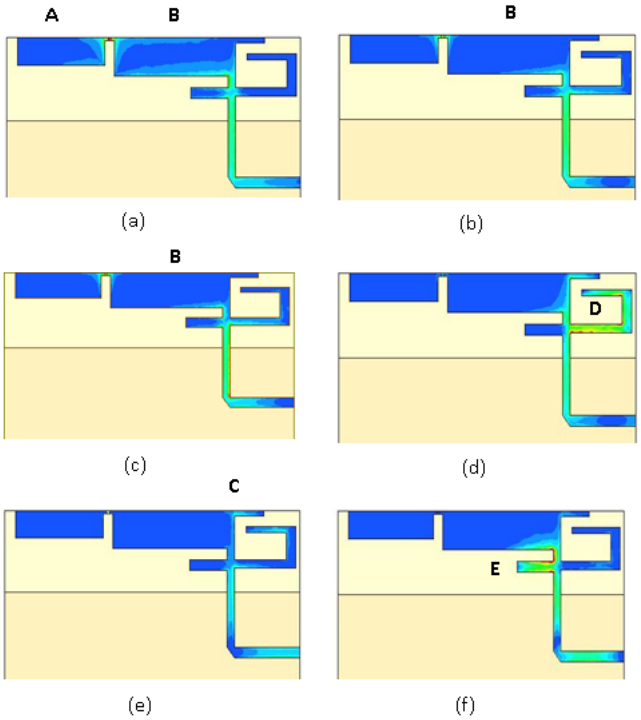

Figure 108: The simulated current distribution of the proposed antenna at: (a) 960 MHz; (b)1800 MHz; (c)1900 MHz; (d)2.4 GHz; (e)3.8 GHz and (f)5.25 GHz. The stronger current is represented by lighter colors

From the results shown in Figure 108, it is observed that the proposed antenna exhibits relatively independent current paths at each resonant frequency, which implies that the resonant frequencies can be tuned selectively independent of each other. To further prove this, parametrical studies were conducted to study the influence of some important parameters on the operational frequency bands of the proposed antenna. The parameters that were chosen in this study were L_1, L_2, L_3, L_4 and L_5 as labeled in Figure 105 and the simulation results are presented in Figure 109 to Figure 113. From these results, it is observed that upon varying the lengths L_1, L_2 and L_3, the resonant frequency at 960 MHz, 1.8 GHz and 5.2 GHz band can be tuned with little influence on the rest of the resonances. Changing the length L_4, the central frequency at 2.4 GHz can be adjust with small effect on the operation band at 3.8 GHz, which is partially determined by the mutual coupling between branch C and D. Similar findings can be observed when the length of L_5 is allowed to vary.

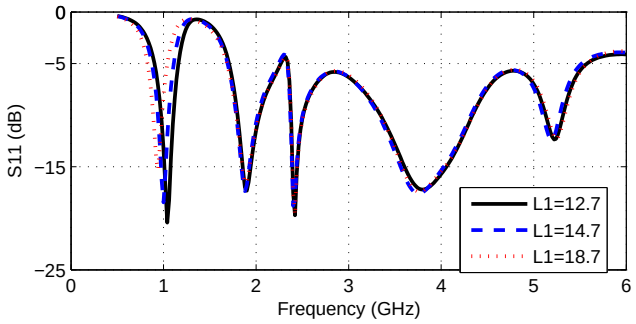

Figure 109: Simulated S11 of the proposed antenna when changing the length of L_1

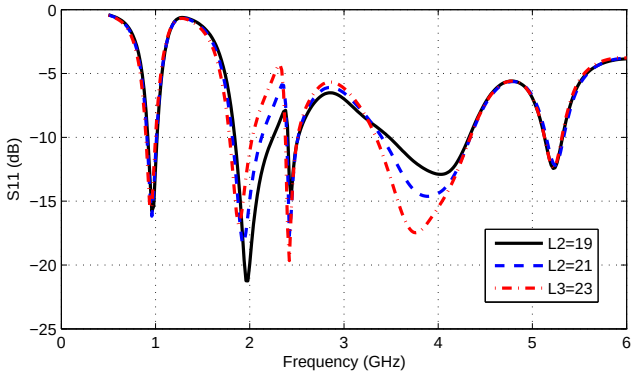

Figure 110: Simulated S11 of the proposed antenna when changing the length of L_2

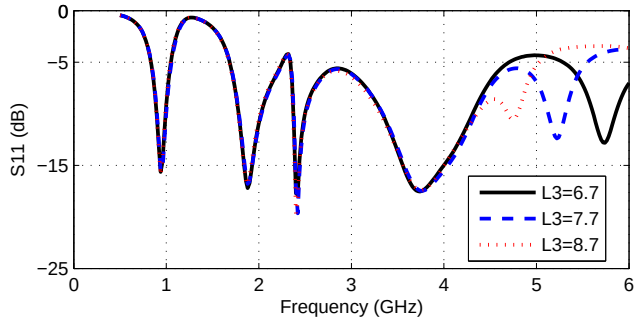

Figure 111: Simulated S11 of the proposed antenna when changing the length of L_3

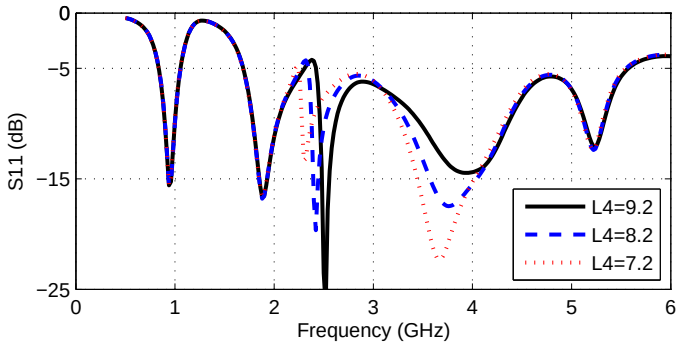

Figure 112: Simulated S11 of the proposed antenna when changing the length of L_4

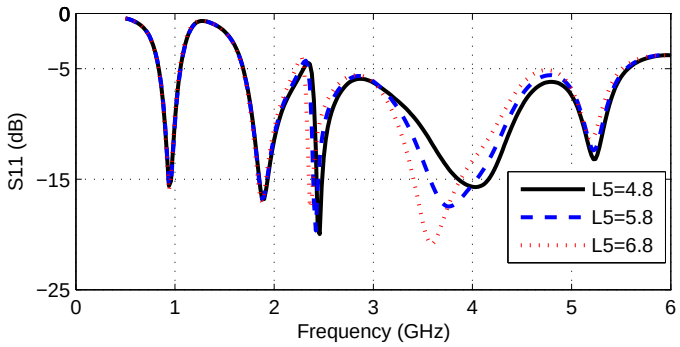

Figure 113: Simulated S11 of the proposed antenna when changing the length of L_5

Besides being a completely planar structure, another advantage of the proposed antenna is that the size of the ground plane has little influence to its resonant characteristics compared to the designs that short the antenna structure to the ground plane. The proposed monopole antenna with different length of ground plane has also been investigated. Figure 114 shows the simulated return loss of the proposed antenna with ground planes of different lengths. It was found that when decreasing the length of the ground plane, at the

desired frequency bands the proposed antenna only exhibits small frequency shifts and some changes on the amplitude of the return loss.

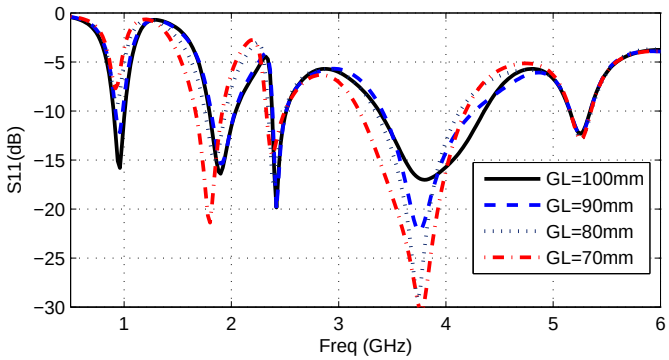

Figure 114: Simulated S11of the proposed antenna with different length of ground planes

The scenario in which the antenna is put into the center of a plastic housing box was also studied in this work. In this simulation model, the wall of the plastic housing is 1 mm thick, 14mm high and has dielectric permittivity of 3.5. The simulation results (Figure 115) indicate that compared to the case when the antenna is radiating in free space, within the plastic housing there is almost no influence on the return loss of the proposed antenna except for small frequency shift at the 3.8 GHz band.

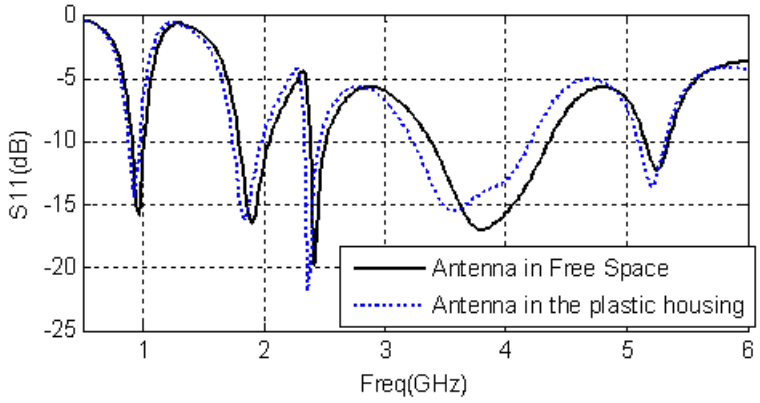

Figure 115: Comparison of the simulated S11 of the proposed multiband antenna when placed in a plastic housing and in free space

The measured radiation patterns of the proposed antenna in free space are presented in Figure 116. It is found that at all the desired frequencies the proposed antenna has radiation patterns similar to a typical monopole antenna, which normally has omnidirectional radiation patterns. The simulation results also suggest that the antenna has moderate gain and efficiency at its operation frequency bands. Ta-

ble 5 summarizes the peak gain and radiation efficiency at the desired frequencies.

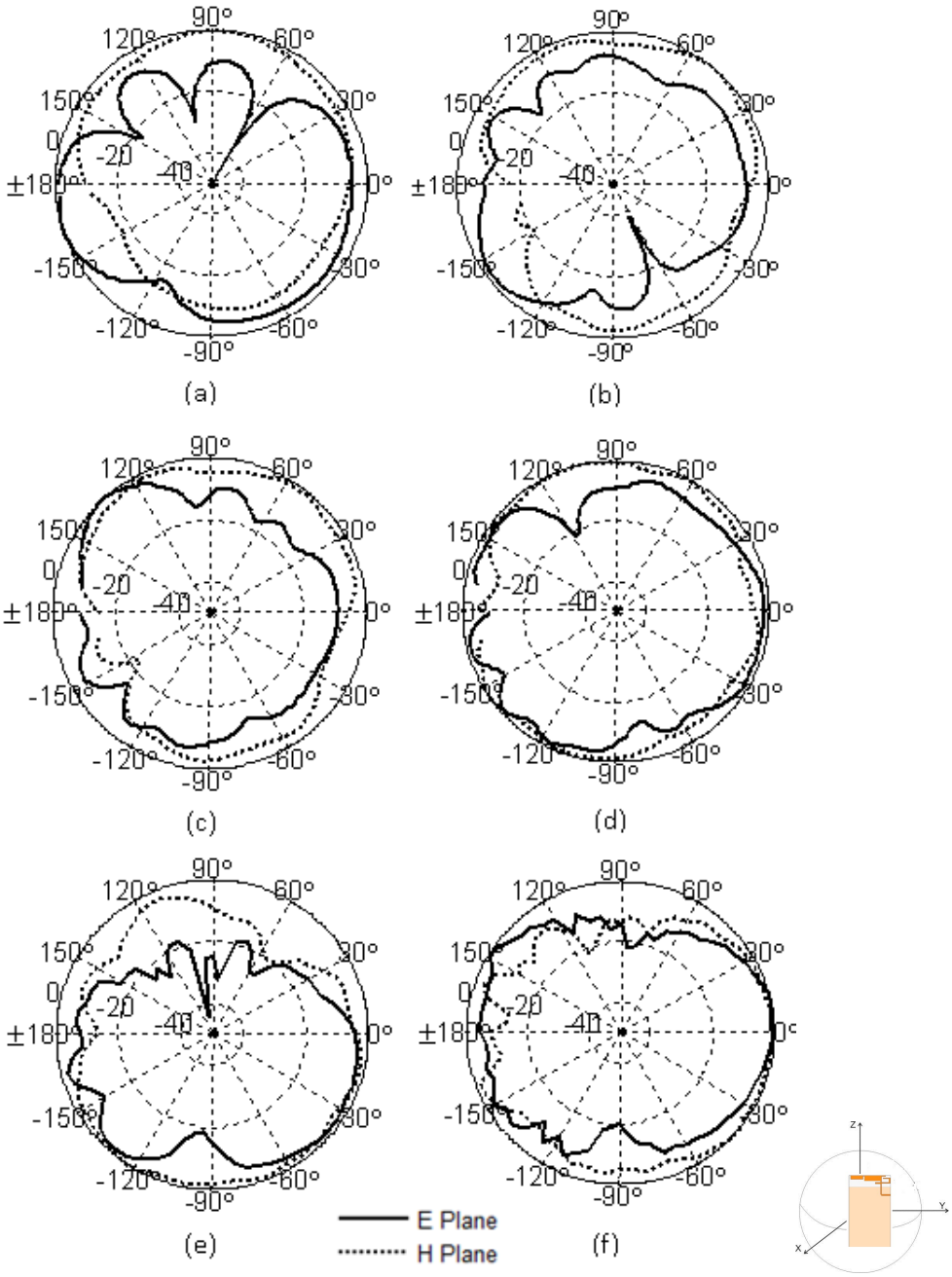

Figure 116: Measured E-plane (X-Z Plane) and H-plane (X-Y plane) radiation patterns of the proposed multiband antenna at: (a) 960MHz; (b) 1800MHz; (c) 1900MHz; (d) 2.4GHz; (e) 3.5GHz; (f) 5.2GHz.

Table 5: Simulated Peak gain and radiation efficiency of the proposed antenna at each frequency band

Frequency(GHz)	Simulated Peak Gain(dBi) / Radiation Efficiency
0.96	1.5 (93.7%)
1.8	2.6 (91.9%)
1.9	2.5 (92.2%)
2.4	2.7 (77.3%)
3.5	2.8 (86.8%)
5.2	1.7 (67.9%)

5.5 ANTENNA IN CLOSE PROXIMITY TO HUMAN HEAD

Normally, mobile phones are to be placed in close proximity to the human body, particularly the head. Therefore, this motivated the need to investigate the influence of the human head on the antenna performance and to study the Specific Absorption Ratio (SAR) of the proposed antenna. To simplify the simulation model and save the simulation time, a simple model of the human head is used instead of using a sophisticated one. The simplified model of the human head was built based on the one suggested in [89]. In this model, the skeleton of the head is modeled as a 'bowl' with radius of 111.5 mm and permittivity of 4.6. The tissue inside the brain is modeled by a uniform liquid with permittivity of 42.9. It is assumed that the antenna is printed at the bottom of the PCB board of the mobile phone device and the antenna is placed at a distance of 10 mm away from the head phantom. This simulation model is implemented in HFSS and is presented in Figure 117.

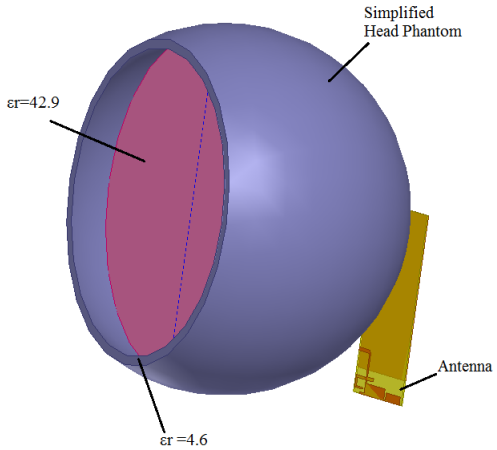

Figure 117: The simulation model of the proposed antenna with the human head

Figure 118 presents the comparison of the simulated return loss between the antenna placed close to the head phantom and in the free space. It is observed that in the situation shown in Figure 117, there is little influence on the resonant frequency of the antenna except some small frequency shifts on the 3.5 and 5.2 GHz bands.

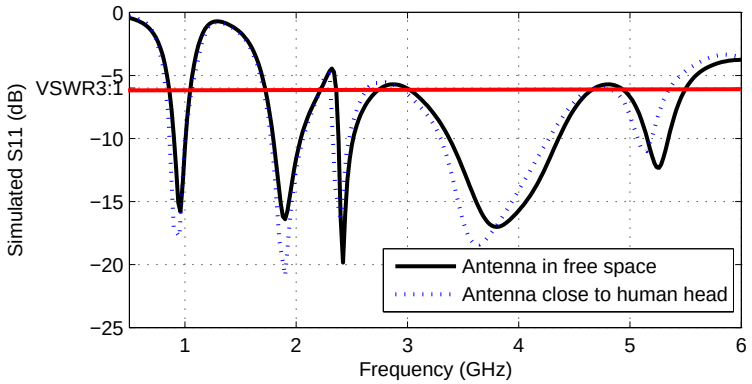

Figure 118: Comparison of the simulated S11 between the antenna with the head phantom and in the free space

Figure 119 shows the simulated radiation patterns of the proposed antenna when it is placed close to the human head. It can be seen that due to the existence of the human head, part of the waves are reflected and the antenna exhibits more directional radiation patterns towards the free space. Table 6 summarizes the comparison between the peak gain and radiation efficiency at each resonant frequency in free space and in closely distance to the human head. It can be found that the radiation efficiency of the antenna decreases when the antenna is placed close proximity to the head.

Table 6: Simulated Peak gain of the proposed antenna at each frequency band

Frequency(GHz)	Simulated Peak Gain(dBi): with head (in free space)	Simulated Radiation Efficiency: with head (in free space)
0.96	1.5 (1.5)	61% (93.7%)
1.8	5.0 (2.6)	73% (91.9%)
2.4	3.7 (2.7)	70% (77.3%)
3.5	4.4 (2.8)	80% (86.8%)
5.2	3.7 (1.7)	48% (67.9%)

The Specific Absorption Ratio is also analyzed with this simulation model. The simulated SAR distribution on the phantom head for the proposed antenna at 960 MHz is shown in Figure 120. The simulation result indicates that with the antenna placed in the location suggested

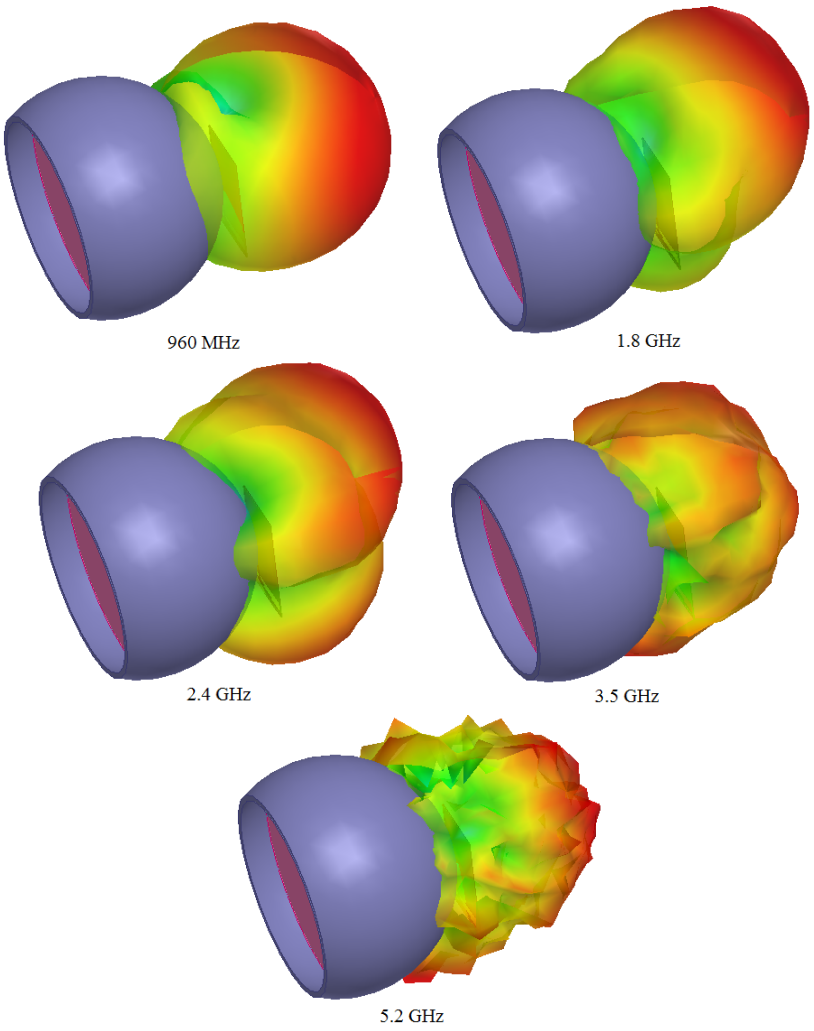

Figure 119: Simulated 3D radiation pattern of the proposed antenna with the human head phantom

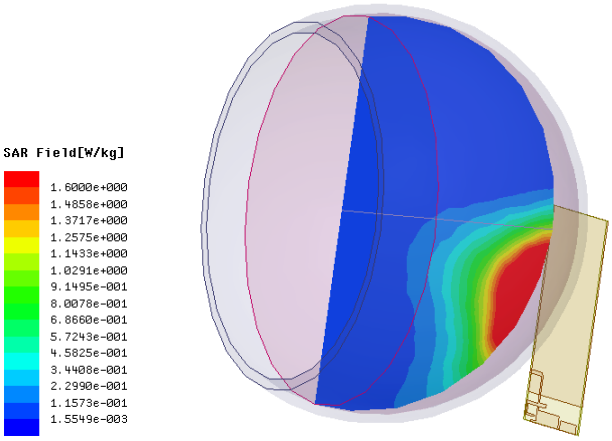

Figure 120: Simulated SAR distribution on the head phantom for the proposed antenna at 960 MHz

in Figure 117, the SAR value for 1 gram head tissue is 1.4 W/Kg, which meets the released SAR limitation of 1.6 W/Kg. It is expected that the SAR value in reality will be smaller than the simulated one due to the adding of the case for the mobile phones.

5.6 SUMMARY OF THE CHAPTER

In this work, a multiband printed monopole antenna for mobile communications is presented. This antenna has a simple planar structure with compact size and covers all the required frequency bands for GSM, DCS, PCS, UMTS dual band WLAN and WiMAX operations. The size reduction of the proposed antenna is achieved by introducing one chip inductor and the resonant frequencies of the proposed antenna can be tuned independently. The simulation results indicate that the proposed antenna has promising radiation efficiency and gain at each required frequency band.

The case when the antenna is put into a plastic housing, and the impact of the size of the ground plane were also studied. Additionally, the operation of the antenna in close distance to the human head has also been investigated. The simulation results show that the proposed antenna exhibits a stable frequency response in each case and have a SAR level that meets the corresponding regulation.

6

COMPACT PRINTED MONOPOLE ANTENNA ARRAY

6.1 INTRODUCTION

Multiple-Input-Multiple-Output (MIMO) techniques enable a wireless device to transmit or receive data with higher data rate. The recently announced IEEE 802.11n and Long Term Evolution (LTE) standard requires the wireless LAN devices and mobile devices to support MIMO. The use of antenna arrays can improve the diversity performance of the antenna, which in turn increases the channel capacity by reducing the fading, suppressing both the random frequency modulation and co-channel interference.

The biggest challenge to design a compact antenna array is how to maintain a good isolation between antennas that are closely spaced. To have good space diversity, traditionally the space between each antenna elements is required to be approximately half of the wavelength. However, for most of the commercial wireless devices, it is impossible to follow this rule due to the size constraints. The objective of this chapter is to explore solutions to design compact antenna arrays. The methodology adopted in this study is to employ the 'neutralizing technique'. Before introducing this technique, in Section 6.2, the criterions that are used to evaluate the performance of a MIMO antenna system are introduced. Then, in Section 6.3, one compact inverted-L antenna array for WLAN USB dongle using the neutralizing technique is presented followed by the summary of the chapter given in Section 6.4.

6.2 PERFORMANCE ANALYSIS OF MIMO ANTENNAS

The performance of a MIMO antenna system can be evaluated by two criterions, envelope correlation coefficient and total multi-port return loss. The definition of these two concepts as well as a brief mathematical derivation will be introduced in following sections.

6.2.1 *Envelope Correlation Coefficient*

One important parameter for evaluating the diversity performance of an antenna array is the envelope correlation coefficient. It is shown in [90] that by modeling the antenna as an open circuit, the correlation coefficient of two antennas is:

$$\rho_{0jk} = \frac{E\left\{(V_{0j} - \tilde{V_{0j}})(V_{0k} - \tilde{V_{0k}})^*\right\}}{\left[E\left\{(V_{0j} - \tilde{V_{0j}})^2\right\} E\left\{\left[(V_{0k} - \tilde{V_{0k}})^2\right]^*\right\}\right]^{1/2}} \tag{109}$$

with:

$$V_{0k}(t) = \iint E_k(\Omega) \cdot h(\Omega, t)\, d\Omega \tag{110}$$

$$V_{0j}(t) = \iint E_j(\Omega) \cdot h(\Omega, t)\, d\Omega \tag{111}$$

where j and k is the antenna number, V_{0k} and V_{0j} represent the open circuit voltage for the kth and jth element, respectively. E is the antenna pattern vector, h is the source vector and Ω is the solid angle. The asterisk means complex conjugate and the swung dash represents the time average over the same interval. The envelope correlation coefficient ρ_e is defined as:

$$\rho_e \approx |\rho|^2 \tag{112}$$

Therefore, by integrating the expression given in Equation 109 over the sphere surround the antennas, the envelope correlation coefficient of a two antenna array can be derived as [91]:

$$\rho_e = \frac{|\iint_{4\pi}[\overrightarrow{F_1}(\theta,\phi) \cdot \overrightarrow{F_2}(\theta,\phi)]d\Omega|^2}{\iint_{4\pi}|\overrightarrow{F_1}(\theta,\phi)|^2 d\Omega \cdot \iint_{4\pi}|\overrightarrow{F_2}(\theta,\phi)|^2 d\Omega} \tag{113}$$

where $\overrightarrow{F_i}(\theta,\phi)$ is the field radiation pattern of the antenna system when antenna i is excited. Generally speaking, the lower the envelope correlation coefficient is, the better the diversity of the antenna array. According to [90], in practical cases the required values of the envelope correlation coefficient for the base station is ρ_e<0.7 and for the mobile devices is ρ_e<0.5. However, using Formula 113 to calculate the envelope correlation coefficient, one needs to know the radiation patterns of the antenna and then solve a complicated integration. One simplified solution was proposed in [91], in which it is found that if the antennas exhibit high radiation efficiency and the receiving antennas are in isotropic signal environments, the envelope correlation can be approximated by using only the S-parameters instead of computing the radiation patterns of the antenna system:

$$\rho_e = \frac{|S_{11}^* S_{12} + S_{21}^* S_{22}|^2}{(1 - (|S_{11}|^2 + |S_{21}|^2)) \cdot (1 - (|S_{22}|^2 + |S_{12}|^2))} \tag{114}$$

This method has been adopted by many researchers. However, this method is based on the assumption that the antennas are lossless. This is not true in a practical situation: there are always losses associated with one antenna such as conduction loss and antenna mismatch loss. In order to refine the method proposed in [91], the radiation ef-

ficiency has been included in the calculation of the correlation coefficient by taking into account the total radiated powers of the antennas, which can be written as [92]:

$$P_{rad,1} = (1 - |S_{11}|^2 - |S_{21}|^2)\eta_1 \tag{115}$$

$$P_{rad,2} = (1 - |S_{22}|^2 - |S_{12}|^2)\eta_2 \tag{116}$$

where η_1 and η_2 are the radiation efficiencies of antenna 1 and antenna 2. Then, the internal loss of these two antennas can be expressed as:

$$P_{loss,1} = (1 - |S_{11}|^2 - |S_{21}|^2)(1 - \eta_1) \tag{117}$$

$$P_{loss,2} = (1 - |S_{22}|^2 - |S_{12}|^2)(1 - \eta_2) \tag{118}$$

Dividing the total S-matrix into two components, one S-matrix for the antenna ports and one for the radiation functions, introducing the losses into the S-matrix and applying the orthogonally requirement, which is a requirement for zero correlation between two columns in an S-matrix, the following expression can be derived:

$$0 = S_{11}S_{12}^* + S_{21}S_{22}^* + \rho_{rec}\sqrt{P_{rad,1}P_{rad,2}} + \rho_{loss}\sqrt{P_{loss,1}P_{loss,2}} \tag{119}$$

where ρ_{rec} and ρ_{loss} are the normalized complex correlation coefficient of the radiation patterns and the internal losses, respectively. These two terms are defined for the purpose of making them correspond to the generalized S-parameters. Substituting Equation 115 - 118 into Equation 119 gives:

$$\begin{aligned} 0 = & \frac{S_{11}S_{12}^* + S_{21}S_{22}^*}{(\sqrt{1-|S_{11}|^2-|S_{21}|^2})(\sqrt{1-|S_{22}|^2-|S_{12}|^2})} \\ & + \rho_{rec}\sqrt{\eta_1\eta_2} + \rho_{loss}\sqrt{(1-\eta_1)(1-\eta_2)} \end{aligned} \tag{120}$$

Assume that $\rho_{loss} = 1$, which means that the internal loss of the antenna has reached the maximum value and is the worst case, it can be seen that the following inequality should be satisfied:

$$\frac{S_{11}S_{12}^* + S_{21}S_{22}^*}{(\sqrt{1 - |S_{11}|^2 - |S_{21}|^2})(\sqrt{1 - |S_{22}|^2 - |S_{12}|^2})\eta_1\eta_2} + \rho_{rec} \leqslant \sqrt{(\frac{1}{\eta_1} - 1)(\frac{1}{\eta_2} - 1)} \tag{121}$$

Therefore, the maximum and minimum values of the correlation coefficients can be expressed as:

$$|\rho_{rec}|_{max,min} = |\rho_{rec,0}| \pm \sqrt{(\frac{1}{\eta_1} - 1)(\frac{1}{\eta_2} - 1)} \tag{122}$$

where

$$\frac{S_{11}S_{12}^{*}+S_{21}S_{22}^{*}}{(\sqrt{1-|S_{11}|^{2}-|S_{21}|^{2}})(\sqrt{1-|S_{22}|^{2}-|S_{12}|^{2}})\eta_{1}\eta_{2}}=|\rho_{rec,0}| \tag{123}$$

From the Equation 122, it can be seen that the second part in the right side of the equation represents an uncertainty of the calculated correlation coefficient. This uncertainty is a function of the radiation efficiency of the two antennas and has been calculated by [92], and is plotted in the following Figure 121.

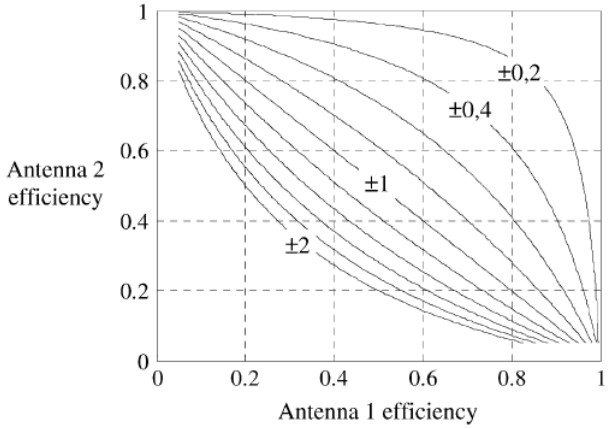

Figure 121: The uncertainly of the calculated correlation coefficient

6.2.2 *Multi-Port Return Loss*

Another approach to evaluate the reasonable operation bandwidth of a MIMO antenna system is to use the Total Multi-Port Return Loss (TMRL), which was recently proposed in [93]. Unlike the previous method that calculates the diversity of the antenna array, this method aims to find out the frequency band(s) in which the antenna array can operate properly using only the S-parameters. The advantage of this method is that it provides a straightforward way to obtain the bandwidth of a multi-port antenna system compared to the conventional method, which needs to consider the impedance match and isolation separately. The TMRL is defined by:

$$TMRL(dB)=-20\log_{10}(\Gamma_{total}) \tag{124}$$

where

$$\Gamma_{total}=\sqrt{\frac{1}{N}\sum_{m,n=1}^{N}|s_{mn}|^{2}} \tag{125}$$

The m, n is the antenna number and N is the total number of the antennas in the array.

6.3 INVERTED-L ANTENNAS ARRAY IN A WIRELESS USB DONGLE FOR MIMO APPLICATION

6.3.1 *Motivation*

Designing a WLAN antenna for an USB dongle requires techniques for antenna miniaturization as the available volume left for antenna is quite small compared to the wavelength at the required resonant frequency. As an example, in [94] a USB memory size antenna for 2.4 GHz Wireless LAN (WLAN) was achieved by using folded trapezoidal antenna. In Chapter 4, a printed monopole antenna for dual band WLAN was designed by combining a fractal geometry with meander line.

In an USB dongle, the available volume for mounting the antennas is typically around $10 \times 17 \times 5\, mm^3$. With respect to design antennas array for USB dongles, it is a challenge task to improve the isolation between each antenna element, since the antennas have to be placed in close space. In [95], a dual band two antennas array was proposed. This antenna consists of an L-shape patch and a via trace connecting the via to the ground. To reach the expected performance, it needs precise fabrication and the experimental result shows that the isolation of this antenna array at 2.4 GHz is less than 9 dB. In [96], a MIMO antenna array for mobile WiMAX (3.5 GHz) was presented. This antenna has a 3D structure and the high isolation was achieved by using a common T-shaped ground plane. The disadvantages of this antenna array are that it is difficult to fabricate and the size of the ground plane can have a great effect on the radiation performance of the antenna due to the shorting structure. Regarding the design of compact planar antenna arrays for WLAN 5.8 GHz on a USB dongle, research has shown that there are few publications in this area, which is the main motivation behind this work.

Recently, a new method named *Neutralization Techniques* has been proposed [17]. Using this method, the isolation of two Planar Inverted-F Antennas (PIFAs) can be improved through neutralizing the current of two antennas without the need of adding extra space for antenna design. So far, this method has only been applied in the design of PIFA antennas and there are few studies investigating the use of the neutralization technique. In this work, we further investigate this technique in the design of an Inverted-L antenna (ILA) array.

6.3.2 *Antenna Design*

In this study, it is decided to employ an Inverted-L antenna structure due to its ease of integration in the overall product design. Figure 122 shows the structure of a classic ILA. The ILA can be viewed as a bent monopole antenna and the total length of the inverted-L, $L_1 + L_2$, needs to be approximately one quarter of wavelength at the resonant frequency of interest. However, the challenge for this work is that the two antennas need to be closely located in a small area of an USB dongle. Generally the available volume for mounting the antennas is around $10 \times 17 \times 5\,\text{mm}^3$, as shown in Figure 123.

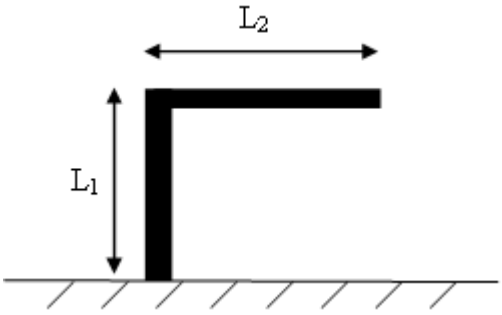

Figure 122: The structure of a typical Inverted-L antenna

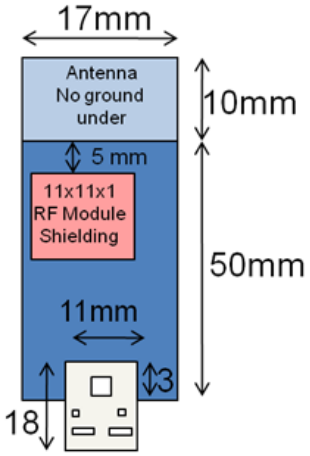

Figure 123: The layout of the WLAN USB dongle

The first attempt in designing a compact ILAs array led to the structure shown in Figure 124. This antenna array has two equal ILAs that are located within a small distance on the PCB board of the USB dongle. Based on the concept proposed in [17], a neutralizing line is added between these two antenna elements to increase the isolation. The length of the neutralizing line is critical in deciding the frequency band where the isolation between the two antenna port can be improved. Increasing the length of the neutralizing line can make the

antenna array has good isolation at lower frequency band. According to [17], the location of the neutralizing line needs to be chosen at place where the surface current is maximum (minimum E field) and the length of it needs to be approximately a quarter wavelength.

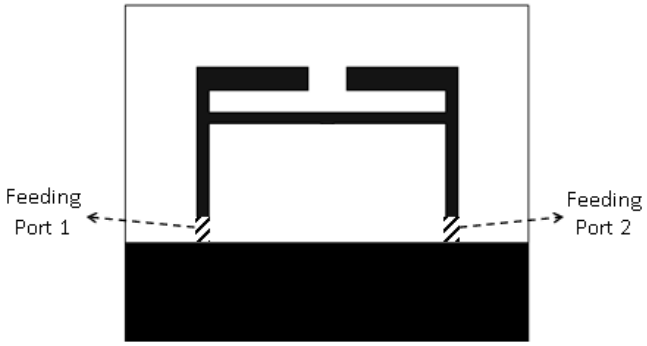

Figure 124: The structure of the antenna array with neutralizing line

As will be presented later, this antenna structure exhibits poor impedance matching at the desired frequency. The low input impedance of the ILA antenna is in fact one of its disadvantages [97]. The typical method employed to solve this problem for a ILA is to short the antenna element to the ground plane and change the feeding position, which in turn increases the input impedance of the antenna. Then the antenna becomes an Inverted-F antenna (IFA), whose input impedance is easier to be matched. However, shorting the antenna to the ground plane will increase the impact of the ground plane size to the radiation performance of the antenna. When connecting the USB dongle to a PC, for example, the equivalent size of the ground plane for the antenna is extended. In this scenario, the antenna may fail to operate at the desired frequency band. Moreover, the isolation between the antennas may also be influenced by shorting them to a common ground plane. Therefore, in this work, we address this limitation without resorting to short the antenna to the ground. Instead, the technique proposed in this study improves the impedance matching of the antenna array by including one vertical stub in the middle of the neutralizing line as described. From the aspect of antenna array, where the isolation between the antennas is of concern, adding this stub has little influence on the isolation between the two antennas as the isolation is mainly controlled by the length, width and position of the horizontal neutralizing line. Meanwhile, for the single antenna itself, as shown in Figure 125, the equivalent antenna structure is one bent monopole with an L-shape stub, which functions as an impedance transformer.

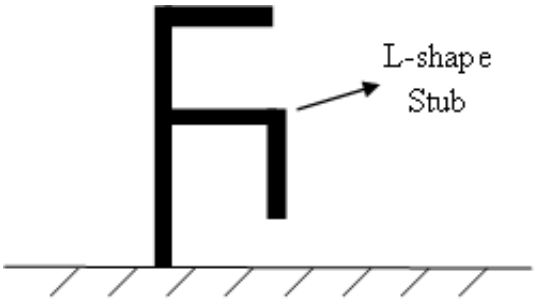

Figure 125: ILA with a L-shape stub

In this way, the use of the neutralizing technique has been further extended to improve the impedance matching of each antenna. Figure 126 presents the final structure of the proposed ILAs array and the key parameters are given in Table 7, where w_1, w_2, and w_3 corresponds to the width of L_1, L_2 and L_3, respectively. The proposed antenna antenna is designed on 0.8 mm thick FR4 with relative permittivity of 4.4 and loss tangent of 0.02. The distance between the two feeding points is $0.15\lambda_{5.8GHz}$ and the gap (d_1) between these two antennas is only $0.02\lambda_{5.8GHz}$, where $\lambda_{5.8GHz}$ represents the free space wavelength at 5.8 GHz.

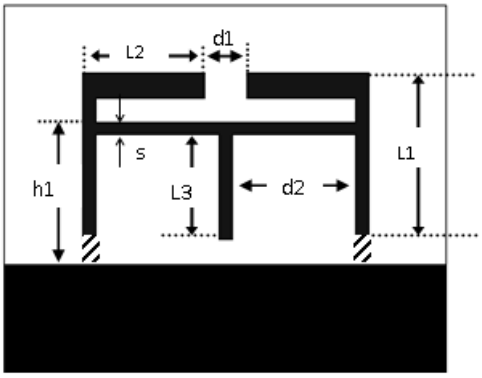

Figure 126: The structure of the proposed antenna array

Table 7: Values of the parameters

Parameter Name	Value (mm)
L_1/W_1	6.65/0.7
L_2/W_2	4/1.1
L_3/W_3	4.1/0.8
h_1	5.1
d_1	1.2
d_2	3.5
s	0.4

6.3.3 *Simulated and Measured Results*

The fabricated prototype of the proposed antenna array is shown in Figure 127. Two semi-flexible cables were used to feed port 1 and port 2 of the antenna array.

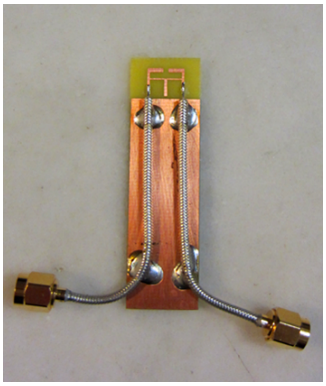

(a) Top view

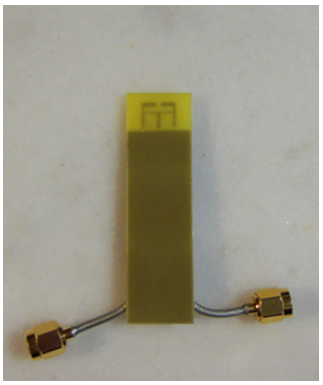

(b) Back view

Figure 127: Photo of the fabricated ILA array

Figure 128 shows the measured return loss and isolation of the proposed antenna array. The measurement results suggest that the proposed ILA array has a 10 dB return loss bandwidth from 5.7 to more than 6 GHz, which is more than the specification required for the WLAN 5.8 GHz frequency band of interest (5.725 to 5.875 GHz). This makes the proposed antenna more robust during product integration, such as proximity to other components and within the product enclosure, thus providing some margin against proximity effects which can lead to some frequency shifts. It is also found that the isolation between the two antennas is always better than 10 dB from 5.5 to 6.0 GHz and within the desired WLAN operation band, an isolation of 12 dB or more is obtained. It is observed that there is some frequency differences (less than 100 MHz) between the measured return losses of the two ports of the antenna array. This is due to the fabrication accuracy and soldering of the feeding cable, which results in the asymmetrical response of the two antenna elements.

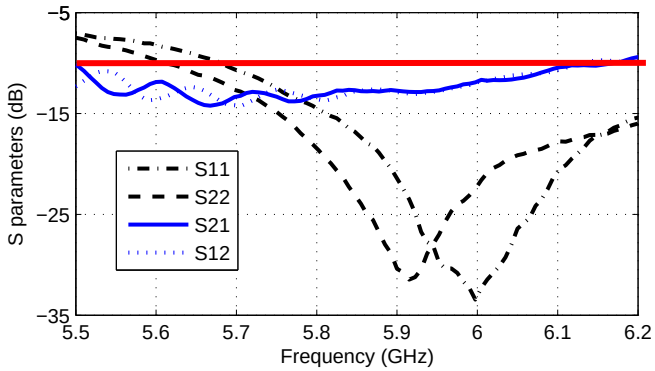

Figure 128: Measured scattering parameters of the ILAs array

Figure 129 (a) and (b) compares the simulated and measured return loss as well as isolation of the proposed antenna array, respectively. There is some frequency shifts between the simulated and measured return loss at both ports especially for the measured S11. This is mainly due to the fabrication accuracy. It is also noticed that the measured return loss has wider bandwidth than the simulated results and the measured isolation between antennas is 2 dB better than the simulated results. The possible explanation is that the fabricated prototype has more losses (e.g. conductor loss) than the simulation model.

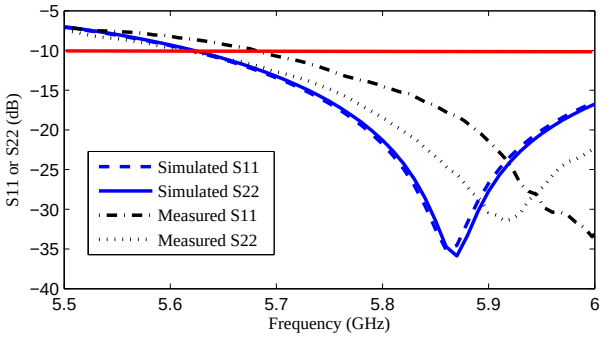

(a) Comparison of the simulated and measured S11 and S22

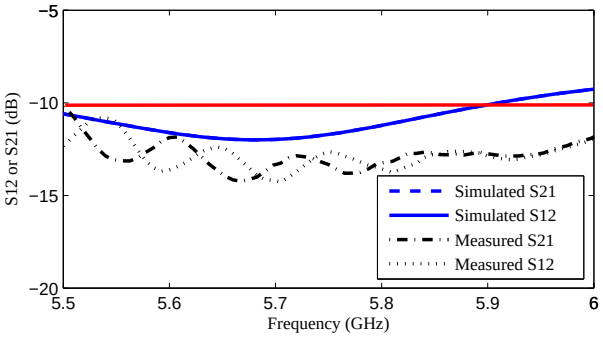

(b) Comparison the simulated and measured S21 and S12

Figure 129: Comparison the simulated and measured return loss and isolation of the proposed antenna array

Figure 130 presents the simulated surface current distribution of the proposed antenna array at 5.8 GHz. It can be seen that at the resonant frequency, when one antenna (Port 2 is excited) is resonating, little current flows back to the port of other antenna (Port 1). Instead, the current is concentrated on the radiating antenna itself and the neutralizing line as well as the top section of the second antenna.

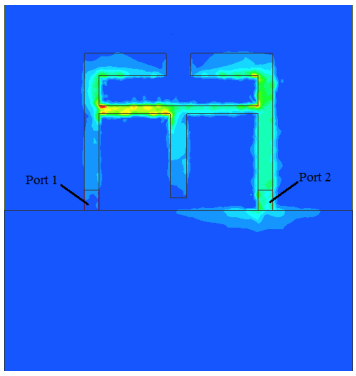

Figure 130: Simulated surface current distribution of the antenna array when Port 2 is excited

Figure 131 presents the simulated return loss of the proposed antenna array with and without the vertical stub on the neutralizing line. The improvement of the return loss with the existence of the stub is obvious whilst there is little change on the isolation between the two antennas at the desired frequency band, where the isolation is always higher than 10 dB.

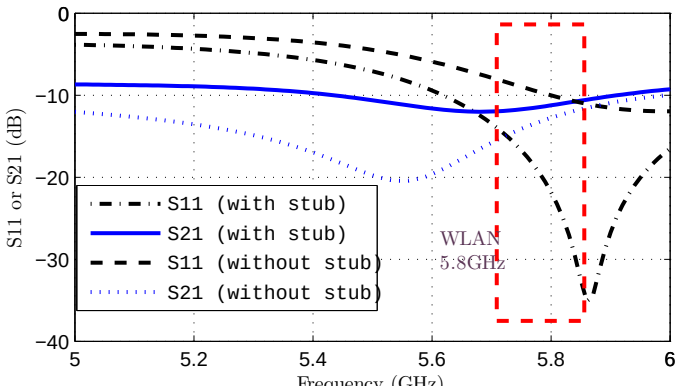

Figure 131: Comparison of the simulated S11 and S21 of the proposed antenna array with and without the vertical stub on the neutralizing line

Figure 132 compares the simulated and measured radiation patterns of the proposed antenna array at 5.8 GHz. During the measurement, the Port 1 was connected to the network analyzer whilst the Port 2 was connected to a 50 Ohm broadband load. There are some disagreements between the simulated and measured results, which is

mainly due to the measurement set up. Comparing to a calibrated antenna, the measured results indicate that the proposed antenna array exhibits a maximum gain around 2.5 dBi at 5.8 GHz.

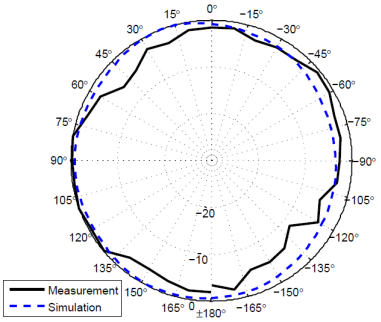

(a) H Plane (X-Y Plane)

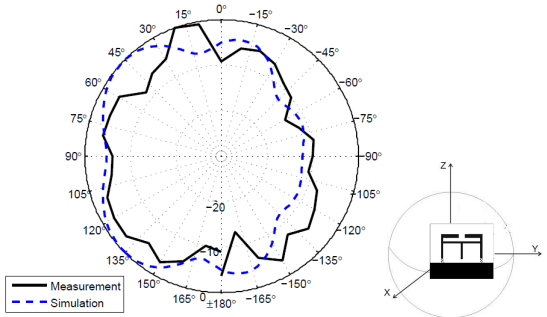

(b) E Plane (X-Z Plane)

Figure 132: Comparison between the simulated and measured radiation patterns of the proposed ILAs array

6.3.4 *MIMO Performance Analysis*

The MIMO performance of the proposed antenna array is analyzed using the envelope correlation coefficient and total multi-port return loss, which have been described in the beginning of this chapter. Figure 133 presents the calculated envelope correlation coefficient of the proposed antenna array. It can be seen that at the desired frequency band, the antenna array has an envelope correlation coefficient less than -40 dB, which is very promising. From simulation results, the radiation efficiency of the proposed antenna array at 5.8 GHz is 91%. Therefore, from equation of the uncertainty (Equation 122) presented in Section 6.2, the calculated correlation coefficient can be estimated to be less than 0.1.

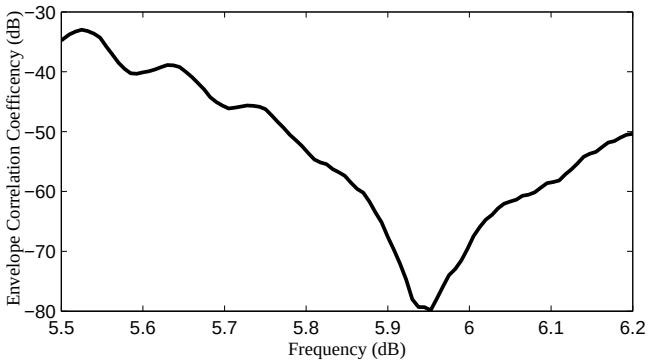

Figure 133: Calculated envelope correlation coefficient of the proposed antenna array

Figure 134 presents the calculated TMRL of the proposed antenna array. It is shown that the ILAs array has a 10 dB TMRL bandwidth from 5.7 to 6.1 GHz, which confirms the MIMO operation bandwidth of the proposed antenna array.

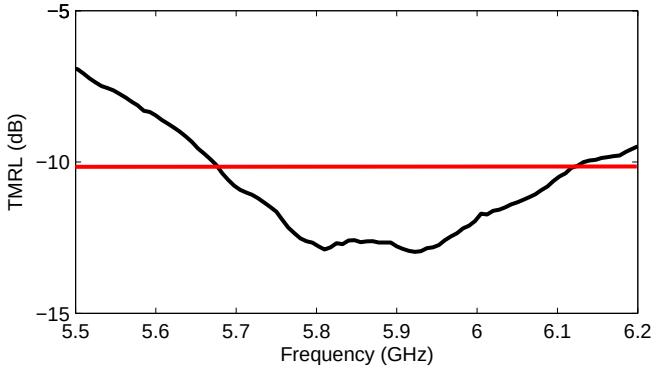

Figure 134: Calculated TMRL of the proposed antenna array

6.3.5 *Conclusion*

In this work, a compact Inverted-L antennas array has been designed for a wireless USB dongle for WLAN 5.8 GHz applications. The two antenna elements are closely spaced and the high isolation between them is achieved by utilizing the neutralization technique. This technique has been further extended to provide impedance matching. One vertical stub is added to the neutralizing line, which improves the impedance matching of both antennas whereas the isolation between the antennas is maintained at an acceptable level.

6.4 SUMMARY OF THE CHAPTER

In this chapter, two criterions that can be used to evaluate the performance of a MIMO antenna system, envelope correlation coefficient

and total multi-port return loss, are introduced. Then, one compact size inverted-L antenna array is proposed for the WLAN 5.8 GHz application. The antennas are closely spaced and the main methodology used to increase the isolation of the two antennas is to employ the 'neutralizing technique'. This technique was firstly proposed to design the single band PIFA array and in this work, it has been innovatively used in the design of printed ILA antenna array. Moreover, in the proposed antenna array, the neutralizing line was also used for the purpose of impedance matching. The measurement results show that the proposed antenna array has a wide operational frequency bandwidth and isolation better than 10 dB over the frequency band of interest.

The work presented in this chapter will be published in:

1. Q. Luo; C. Quigley; J. Pereira and H. M Salgado. Inverted-L Antennas Array in a Wireless USB Dongle for MIMO Application. *In Proceedings of 6th European Conference on Antennas and Propagation (EuCAP)*, Prague, Czech Republic, March 2012.

Part III

RECONFIGURABLE ANTENNA DESIGN

7

TUNABLE MULTIBAND ANTENNA WITH AN ACTIVE ARTIFICIAL MAGNETIC CONDUCTOR GROUND PLANE

7.1 INTRODUCTION

An important topic addressed in this thesis work is to explore innovative method to design reconfigurable antennas, which has attracted much research interests. In this work, the methodology adopted is to employ an active Artificial Magnetic Conductor (AMC) as the ground plane of the antenna and frequency tuning of the antenna is achieved by controlling the reflection phase of the ground plane.

This chapter is organized as follows. The concept and analytical model of the artificial magnetic conductor is introduced in Section 7.2. Then, a detailed description of the proposed reconfigurable antenna with the active AMC ground plane is presented in Section 7.3. Finally, the summary of this chapter is given in Section 7.4.

7.2 THE ARTIFICIAL MAGNETIC CONDUCTOR

The artificial magnetic conductor (AMC), which is also referred as High Impedance Surface (HIS), can provide zero reflection phase for the incident waves as a Perfect Magnetic Conductor (PMC) at certain frequencies. One of the classic methods for analyzing the artificial magnetic conductor is to use the resonant cavity model [98]. This method considers the AMC as a resonant cavity (Figure 135) formed by a ground plane and a partially reflected surface (PRS).

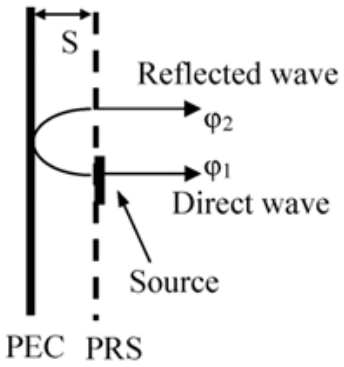

Figure 135: Cavity model for the Artificial Magnetic Conductor

Assuming that there is a source outside of this cavity, the phase shift of the reflected wave compared to the incident wave is mainly

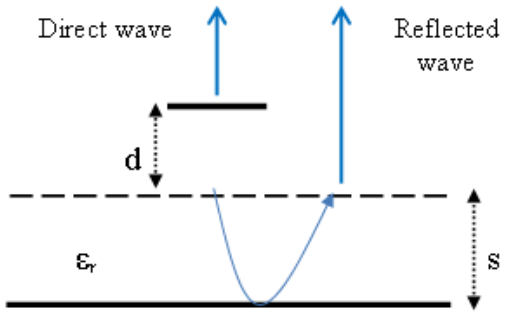

Figure 136: The propagation model when the source is located at a distance of d from the AMC

introduced by the ground plane, the propagation path and the phase shift brought by the PRS. In order to satisfy the resonant condition of the cavity, at the desired frequency the phase differences of these two transmitted waves need to be zero. According to [98], this condition is written as:

$$\phi_2 - \phi_1 = 2\phi_T - \frac{2\pi}{\lambda} \times 2S - \pi = 2N\pi, \qquad N = 0, 1, 2 \ldots \tag{126}$$

where ϕ_T is the phase shift from the PRS and S is the distance between the perfect electrical conductor and the PRS. Under this condition, the cavity behaves as a perfect magnetic conductor with normal incidence angle. In [98], it is assumed that the source is at the same level of the PRS and all the wave propagates in free space. However, in practice the source, take an dipole antenna as an example, need to be located at a small distance above the AMC that always consists of certain periodical structure on a dielectric material (Figure 136).

Therefore, in this case, the formula needs to be revised as:

$$\phi_2 - \phi_1 = 2\phi_T - \frac{2\pi}{\lambda_0} \times 2d - \frac{2\pi}{\lambda_e} \times 2S - \pi = 2N\pi, \qquad N = 0, 1, 2 \ldots \tag{127}$$

where d is the distance between the radiation source and PRS, λ_0 is the free space wavelength and λ_e is the effective wavelength in dielectric materials and equals to:

$$\lambda_e = \frac{\lambda_0}{\sqrt{\epsilon_r}} \tag{128}$$

The ϵ_r represents the permittivity of the substrate. If the transmission coefficient of the PRS is known, the maximum boresight directivity of the antenna can be optimized by calculating the distance between the antenna and the AMC ground plane. To calculate the reflection coefficient of a plane wave incident to the AMC ground plane, it is necessary to calculated the impedance of the AMC, which is a

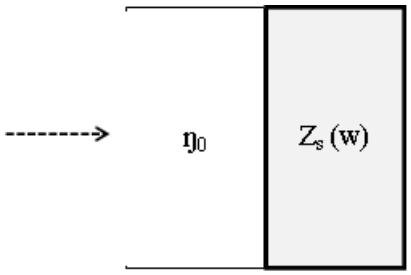

Figure 137: The plane wave with normal incident angle propagates towards the AMC with impedance of $Z_s(w)$

complex value as a function of the frequency. Assume the impedance of the AMC is $Z_s(w)$, by using the boundary condition of the wave propagation between two different medias, as demonstrated in Figure 137, the reflection coefficient can be calculated by:

$$\Gamma(w) = \frac{Z_s(w) - \eta_0}{Z_s(w) + \eta_0} \tag{129}$$

where η_0 is the impedance of the free space. At the frequency where the impedance of the AMC, $Z_s(w)$, is infinite or much larger than η_0, the reflection coefficient $\Gamma(w) = 1$. This frequency is the resonant frequency of the AMC, at which the AMC structure behaves as a PMC.

The circuit model of the AMC has been investigated by several researchers, aiming at deriving the impedance ($Z_s(w)$) of the AMC by means of the equivalent circuit structure. For an AMC that is constituted by square patches array as shown in Figure 138, the AMC can be modeled by a transmission line network with the gap between adjacent unit cells represented by a T-network [99]. Another way to investigate the AMC is to model it as a parallel connection of the series resonant grid and a metal-backed dielectric slab [100].

Assume the impedance of the series resonant grid is Z_g and a metal-backed dielectric slab is Z_d, the the impedance of the AMC satisfies:

$$Z_{inp}^{-1} = Z_g^{-1} + Z_d^{-1} \tag{130}$$

Figure 139 presents the effective surface impedance model of the AMC structure proposed in [100]. The L_d represents the inductance of the metal-backed dielectric slab, L_g is the metal grid inductance. The C_{ga}, C_{gd} and C_f represents the gap capacitance of the grid, the capacitance from the electric flux in the dielectric region and the fringing capacitance, respectively. By solving this equivalent circuit structure, the surface impedance of the AMC structure can be calculated:

$$Z_{inp} = Z_g \| Z_d = \frac{jwL_d(1 - w^2 L_g(C_{ga} + C_{gd} + C_f))}{1 - w^2(C_{ga} + C_{gd} + C_f)(L_g + L_d)} \tag{131}$$

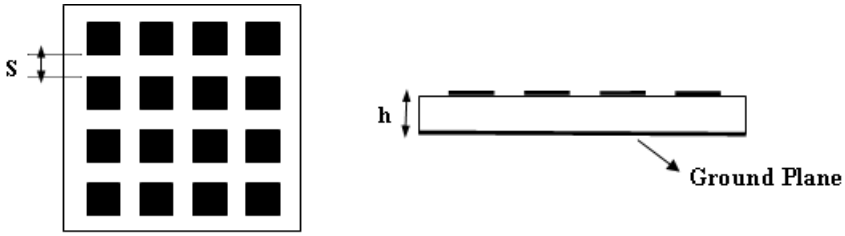

(a) Top and Side view of the AMC with planar square patch

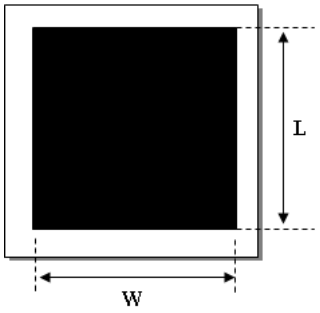

(b) The unit cell of the AMC surface

Figure 138: Artificial Magnetic Conductor with square patch arrays

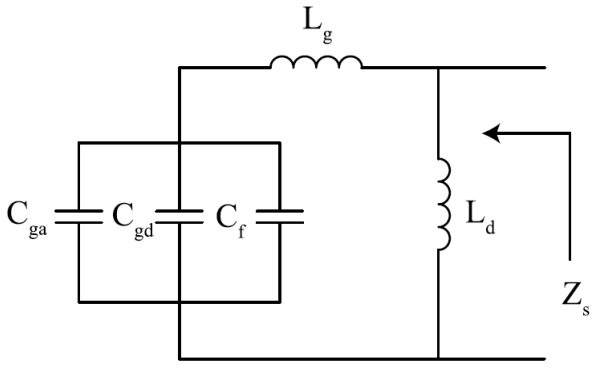

Figure 139: The effective surface impedance model of the AMC structure

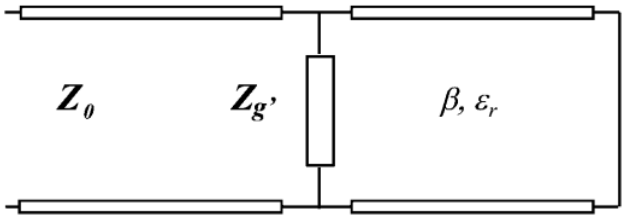

Figure 140: The transmission line model of the AMC as a parallel connection of the PRS and a metal-backed dielectric slab

The resonant frequency, at which the surface impedance of the AMC can reach infinite, can be found by letting the dominator of Equation 131 equal zero. Then, the resonant frequency of f_r can be found:

$$f_r = \left(2\pi\sqrt{((C_{ga} + C_{gd} + C_f)(L_g + L_d))}\right)^{-1} \tag{132}$$

However, these studies has two limitations. Firstly, it can only be applied to AMC with square patch unit cells. Secondly, it is based on the assumption that the plane wave has a normal incident angle. To solve the second limitation, in [101], the reflection and transmission coefficient of the AMC with a geometry of rectangular patch arrays with different plane wave incident angles has been investigated. In that study , the AMC was also analyzed using the transmission line model and the impedance of the AMC surface is also calculated by separating it into a parallel connection of the grid impedance of the PRS ($Z_g^{'}$) and a metal-backed dielectric slab as shown in Figure 140.

Therefore, the impedance of the AMC were also calculated by using the expression shown in Equation 130. In this study, the grid impedance and the impedance of the grounded dielectric layer were calculated in the circumstance of TE and TM polarized incident wave with oblique angle. Reference [101] derives the expression for the impedance of the AMC for the TM and TE wave of θ incident angle as:

$$Z_{p,inp}^{TM} = \frac{j\omega\mu\frac{\tan(\beta h)}{\beta}\cos^2(\theta)}{1 - 2k_{eff}\alpha\frac{\tan(\beta h)}{\beta}\cos^2(\theta)} \tag{133}$$

$$Z_{p,inp}^{TE} = \frac{j\omega\mu\frac{\tan(\beta h)}{\beta}}{1 - 2k_{eff}\alpha\frac{\tan(\beta h)}{\beta}(1 - \frac{1}{\epsilon_r+1}\sin^2\theta)} \tag{134}$$

with:

$$\alpha = \frac{k_{eff}D}{\pi} ln(\frac{1}{\sin\frac{\pi w}{2D}}) \tag{135}$$

$$k_{eff} = k_0\sqrt{\epsilon_{eff}} \tag{136}$$

$$\beta = \sqrt{k^2 - k_t^2} \tag{137}$$

where k is the wave number in the substrate material and k_t is the tangential wave number component imposed by the incident wave. It is known that the impedance of the TE and TM waves are:

$$Z_0^{TE} = \frac{\eta_0}{\cos\theta} \tag{138}$$

$$Z_0^{TM} = \eta_0 \cos\theta \tag{139}$$

Therefore, the reflection coefficient of the TE and TM wave with different incident angle can be calculated from:

$$\Gamma_{TE}(w) = \frac{Z_s^{TE}(w) - Z_0^{TE}}{Z_s^{TE}(w) + Z_0^{TE}} \tag{140}$$

$$\Gamma_{TM}(w) = \frac{Z_s^{TM}(w) - Z_0^{TM}}{Z_s^{TM}(w) + Z_0^{TM}} \tag{141}$$

The formulas developed by [101] can provide a good prediction of the reflection coefficient of the AMC with an arbitrary polarization and incident angle. However, this method is again limited to the AMC with square patch structures as was the case of the theoretical model proposed by [99]. For certain specific geometries, such as Jerusalem Cross based AMC, the estimation of its characteristics was investigated in [102]. However, regarding the AMC with more complex surface patterns, with which the AMC can be designed for operating at lower frequencies or multiple frequencies with a reduced size, currently there is no general model that can be applied. Therefore, the most common technique to design compact size AMC structure is to based on the analysis of general characteristics of AMCs and performing EM simulations using FDTD or FEM methods to get more accurate results.

7.3 RECONFIGURABLE ANTENNA WITH ACTIVE AMC

7.3.1 *Motivation*

Reconfiguration of antenna provides the possibility of designing antennas of more compact size whilst operating in several frequency bands. One of the most common methods to make an antenna reconfigurable is to change the electrical length or impedance matching of the antenna by directly adding some RF switches such as PIN diode or MEMS (Micro-electromechanical Systems) switches on the radiation element. In [103], a coplanar antenna that can operate from 4.9 to 5.4 GHz was achieved by adding a varactor between the square patch and the surrounding ground plane. Upon using a large num-

ber of MEMS, a reconfigurable pixel-patch antenna design that can change its operating frequency and radiation pattern as well as polarization, is presented in [104]. Instead of using a large number of MEMS, in [105, 106] the antennas were designed by mounting the MEMS switches on certain key parts of the radiation element and by changing the status of them, the resonant frequencies or the radiation pattern can be reconfigured. However, it is necessary to point out that adding RF switches directly on the antenna element requires including extra lumped elements such as capacitors and inductors for the purpose AC/DC isolation, which will influence the radiation performance of the antenna.

Recently, researchers found that when using a reconfigurable artificial magnetic conductors as the ground plane for one antenna, it can to some degree control the resonant frequency of the overall antenna system [29, 30, 31]. By doing this, there is no need to include extra lumped elements on the antenna, which could improve the radiation efficiency of the antenna and simplify the fabrication process. However, currently there is not much work been done in this area, which requires further investigation.

7.3.2 *The Design of Active AMC Ground Plane*

Artificial magnetic conductors, due to its unique characteristic, which is to provide in-phase reflection phase over certain frequency band(s), have been widely used in low profile antenna designs. Figure 141 shows the structure of an AMC that consists of periodic square shaped unit cells on top of one substrate backed by a perfect electric conductor (PEC) ground plane. This type of structure only provides in-phase reflection over a single frequency band.

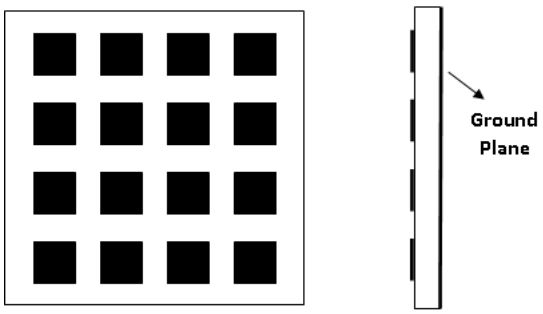

Figure 141: Top and side view of the AMC ground plane

In this study, it is found that if RF switches, such as PIN diodes or MEMS switches are used to connect adjacent unit cells, a group of four unit cells can be aggregated to behave like a larger size unit cell as illustrated in Figure 142. Using this technique, the operation frequency of an AMC can be tuned to a much lower frequency band.

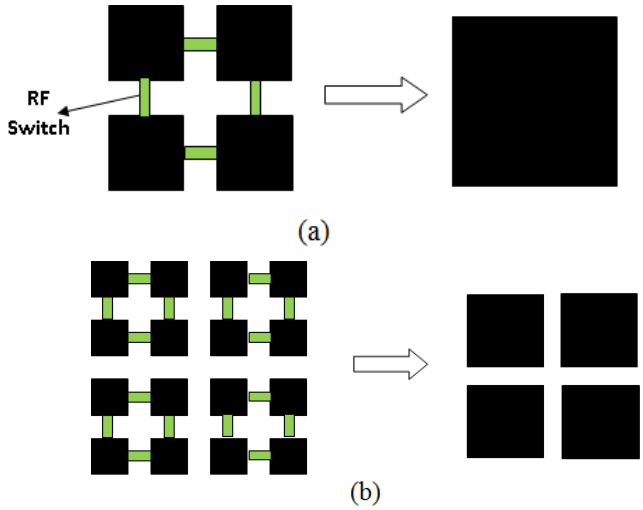

Figure 142: (a): Demonstration of four unit cells aggregated to one larger unit cell; (b): Demonstration of 4×4 unit cells aggregated to 2×2 unit cells of equivalent size

Figure 143 presents the simulated reflection phases of the AMC when the RF switches are 'ON' and 'OFF'. The AMC were designed on substrate FR4 with thickness of 1.6 mm and relative permittivity 4.4. The unit cell of AMC is a $10 \times 10\,\text{mm}^2$ square patch and the gap between adjacent unit cells is 2 mm. When all the switches are turned OFF, the AMC has a central frequency (the frequency that has 0 degree reflection phase) at 5.8 GHz. When the switches are turned ON, this frequency shifts to 2.4 GHz, a change of over 50%. Using this simple technique, an active AMC ground plane can be implemented.

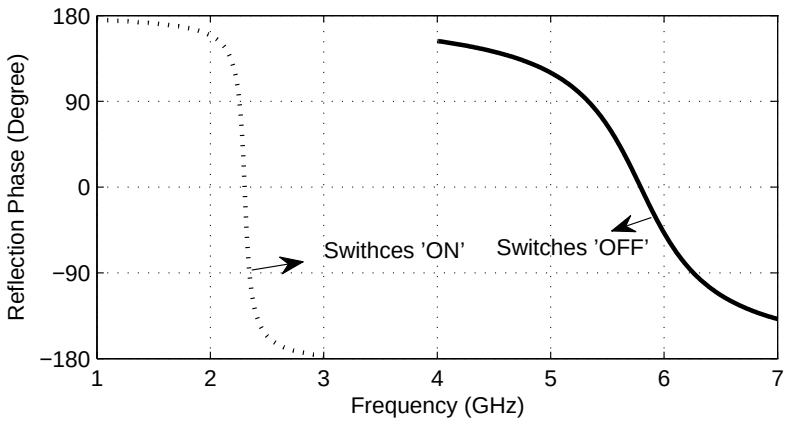

Figure 143: Reflection phase when the switches on the AMC surface are ON (dotted line) and OFF (solid line); the results are exported from HFSS

7.3.3 *Design of Tunable Antenna on Active AMC Ground Plane*

In the first stage of this work, one coplanar patch antenna is placed above the AMC ground plane (with all switches 'OFF') at the height (h) of only 2 mm, which is less than $0.05\lambda_{2.4GHz}$, where λ is the free space wavelength. The distance between the coplanar antenna and AMC ground plane is decided by doing a parametrical sweep and then looking for the minimum height where the antenna can exhibit a good return loss. Figure 144 (a) shows the top view of the coplanar patch antenna. This antenna is designed on substrate Roger 4003 with thickness of 0.813 mm and relative permittivity (ε_r) 3.38. This antenna has a size of $50 \times 50\,mm^2$ and the simulation shows that it can resonate at 3.4 GHz and 5.9 GHz. Figure 144 (b) shows the side view of the overall structure when the coplanar patch antenna is placed above the AMC ground plane. The overall thickness of the proposed antenna structure is 4.4 mm.

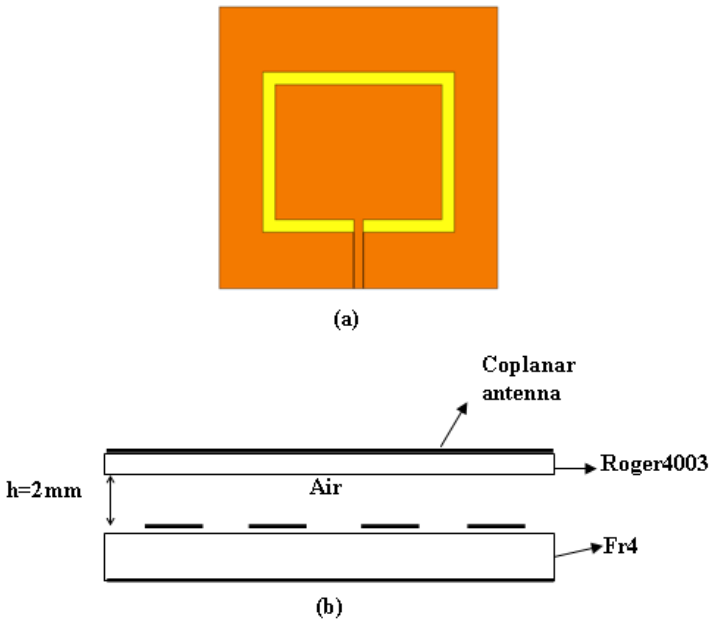

Figure 144: (a) Top view of the coplanar patch antenna; (b) side view of the coplanar patch antenna 2 mm above the AMC

It is observed that besides achieving a low profile antenna, it is also possible to tune the antenna to operate in multibands by exciting the AMC ground plane to act as another resonant element. Furthermore, if the AMC ground plane is reconfigured as shown in Figure 142, the antenna can resonate at another two frequencies, which turns the original coplanar antenna into a quarter-band antenna. To simplify the fabrication process, two AMC ground plane prototypes have been fabricated: one with classic square type unit cells to mimic the case when the RF switches are in the 'OFF' state (Figure 145 (a)) and one with a narrow microstrip line of width 1.5 mm between the adjacent

unit cells to mimic the case when the RF switches are in the 'ON' state (Figure 145 (b)). The AMC ground planes are fabricated on substrate Fr4 with thickness of 1.6 mm with size of $50 \times 50\,\text{mm}^2$.

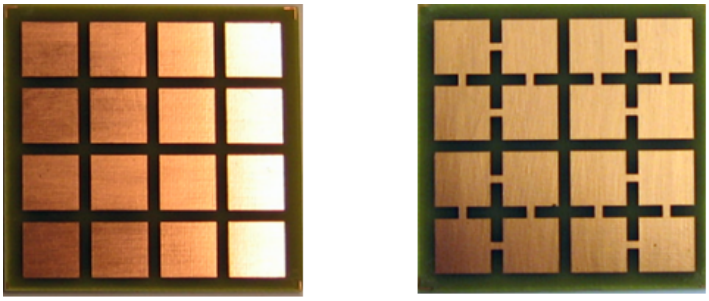

Figure 145: Top view of the two fabricated AMC ground plane that mimic the case when the switches on the AMC surface are perfectly switched (a)'OFF' and (b) 'ON'.

7.3.4 *Simulated and Measured Results*

Figure 146 (a) and (b) presents the simulated and measured return loss of the coplanar patch antenna, respectively. Dashed line represents the original antenna in free space and the solid line corresponding to the case when the antenna is placed 2 mm above the AMC ground plane with all the switches in the 'OFF' state (see Figure 145 (a)).

From both the experimental and simulated results, it is found that at the 5 GHz band even for a distance of only 2 mm between the coplanar antenna and the AMC ground plane, the antenna still exhibits a good return loss in the upper band with a central frequency of 5.9 GHz and a bandwidth of more than 9%. Moreover, one more resonant frequency at 4.5 GHz with 13% bandwidth is also observed. This is brought by the AMC ground plane: the coplanar antenna couples some energy to the AMC which in turn becomes resonant, behaving similarly to a stacked antenna. It is also observed that in the free space, the coplanar antenna can also resonate at 3.4 GHz; however, this operational band is diminished when it was placed at a small distance above the AMC ground plane due to the fact that the AMC ground plane only has in-phase reflection phase at 5.8 GHz band (Figure 143).

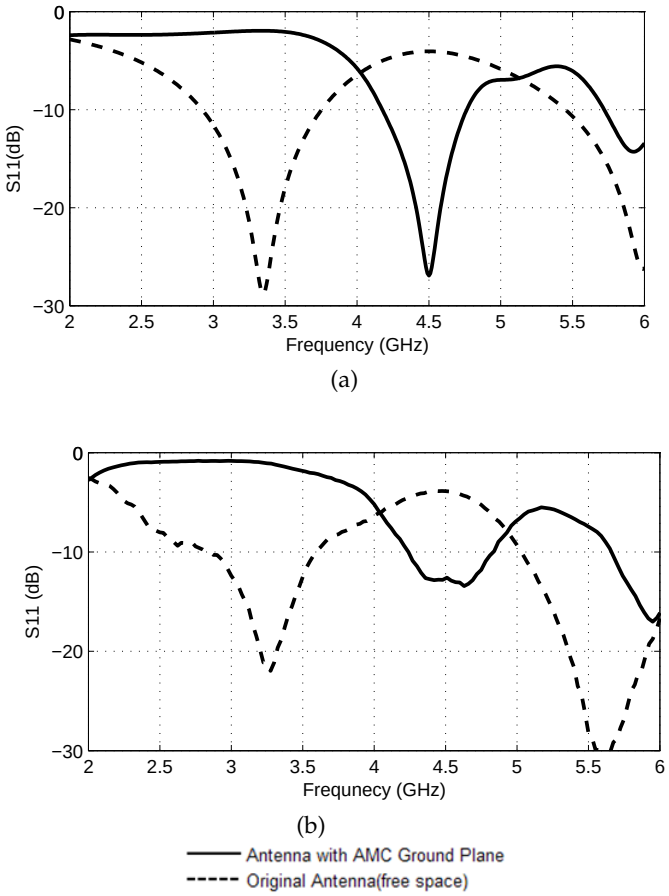

Figure 146: (a) Simulated and (b) Measured S11 of coplanar antenna in free space and with the AMC ground plane when the RF switches are OFF

The next step is to consider the RF switches to be in the 'ON' state (Figure 145 (b)). Figure 147 (a) and (b) compare the return loss when the switches are in the 'ON' and 'OFF' state, for both the simulated and measured results. The measurement results indicate that when all the switches are turned ON, the resonant frequency f_1 decreased from 5.9 to 5 GHz, which is due to the tuning of AMC ground plane. Meanwhile, the resonant frequency f_2 reduced to 2.4 GHz, which is caused by increasing the equivalent size of AMC's unit cells (see Figure 142). These results show that after adequately optimizing the dimensions of both the coplanar patch antenna and AMC, it is possible to make this antenna resonant at two other useful frequency bands by changing the states of the switches. The differences between the simulation and experimental results might be caused by fabrication error and uncertainties of the exact permittivity of the substrate.

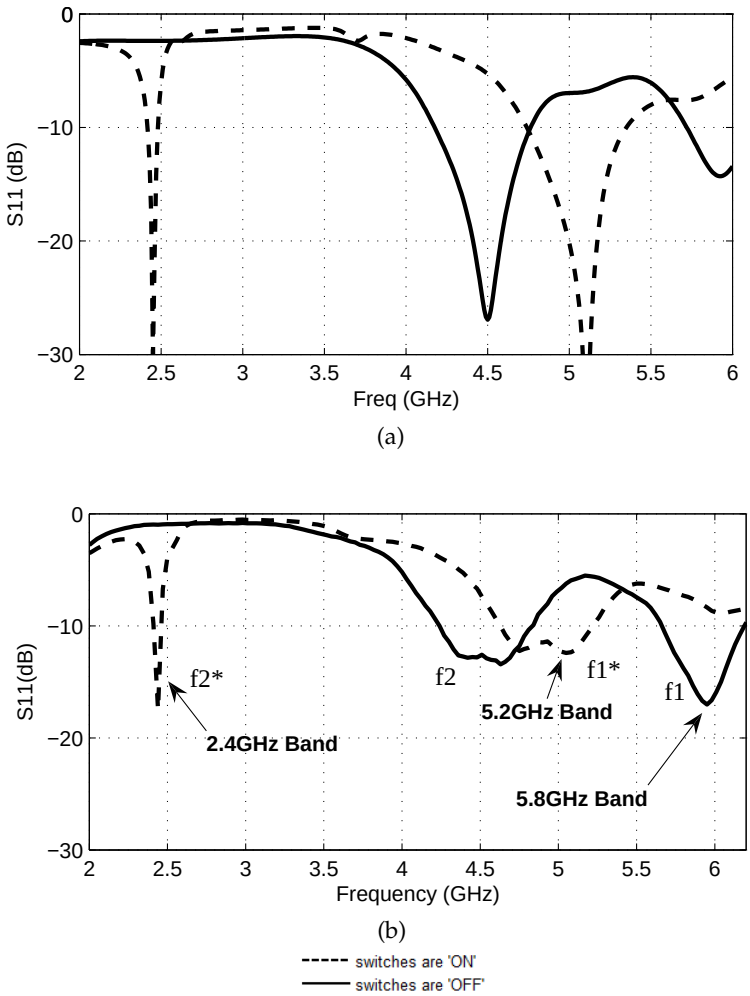

Figure 147: (a) Simulated and (b) Measured S11 of the proposed reconfigurable coplanar antenna when the RF switches are in 'ON' (dash line) and 'OFF' (solid line) state.

Figure 148 (a) and (b) present the measured radiation patterns of the proposed antenna at 2.4 and 5.2 GHz when all the RF switches are switched ON while Figure 148 (c) and (d) show the measured radiation patterns of the proposed antenna at 4.5 and 5.9 GHz when all the RF switches are in 'OFF' states. Table 8 briefly summarizes the radiation characteristics of the proposed antenna. It is found that at 2.4 GHz, the antenna has the lowest radiation efficiency, which is only 61%. Since resonance at this frequency is induced by the excitement of the AMC surface, the low efficiency might be caused by the high coupling between each AMC unit cells and energy dissipation on the AMC. At all other operation frequencies, the antenna shows good radiation efficiency (>86%) and gain (3.8 dBi)

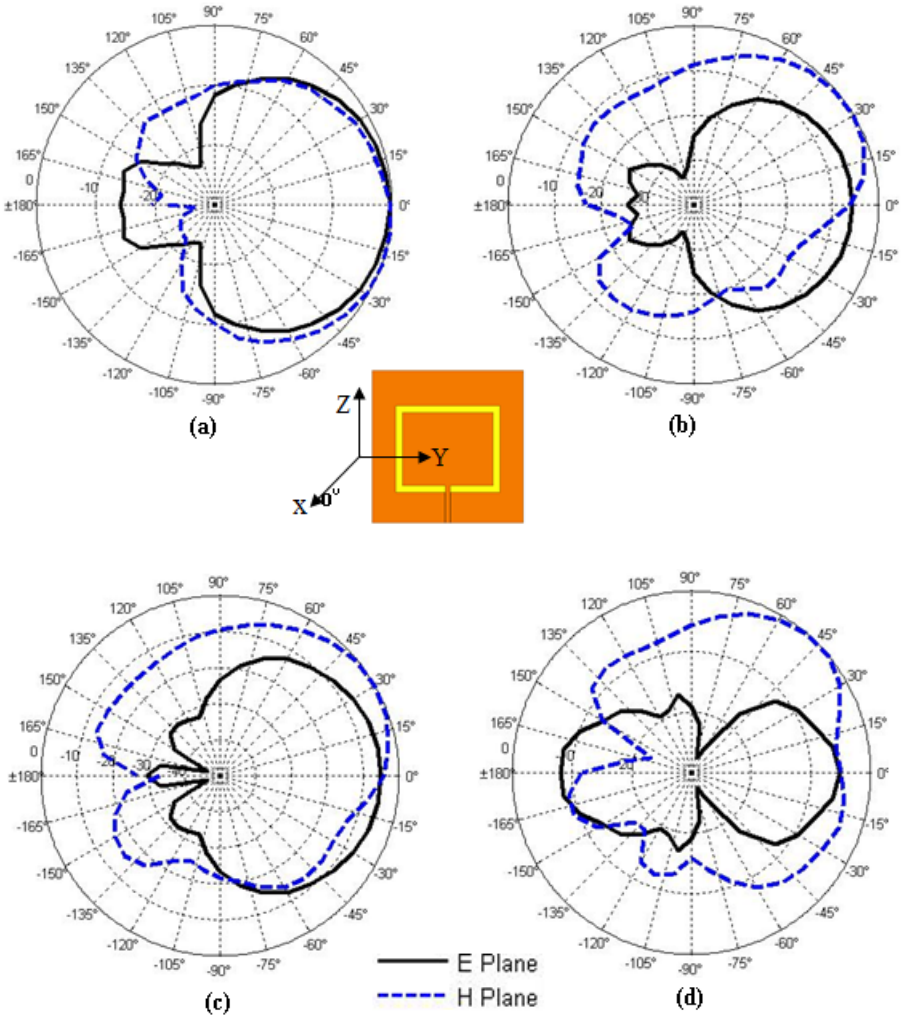

Figure 148: Measured E-plane (X-Z Plane) and H-plane (X-Y plane) radiation patterns at: (a) 2.42 GHz, (b) 5.2 GHz, (c) 4.5 GHz and (d) 5.9 GHz

Table 8: Summary of the radiation characteristics of the proposed antenna

Frequency (GHz)	Measured Bandwidth (GHz)	Simulated Maximum Gain (dB)	Simulated Radiation efficiency
2.4*	2.41-2.46	0.5	61%
4.5#	4.24-4.84	4.1	93%
5.1*	4.63-5.26	5.5	94%
5.9#	5.65-6.19	3.8	86%

* switches are in 'ON' states
# switches are in 'OFF' states

7.3.5 *Conclusion*

In this work, a new tunable coplanar patch antenna with an active AMC ground plane has been presented. It is shown that by using the AMC as the ground plane, not only one can design a low profile coplanar antenna, but also can turn the antenna to have an added functionality which is a tunable multiband operation characteristic. With the active AMC ground plane that can be reconfigured by switching ON/OFF the RF switches, experimental results show that this proposed AMC coplanar antenna can operate at four different bands: 2.41-2.46 GHz, 4.24-4.84 GHz, 4.63-5.26 GHz and 5.65-6.19 GHz. These include almost the entire required bands for WLAN 802.11a/b/g applications. Future work, besides further optimizing the overall antenna performance, involves mounting the RF switches on the surface of AMC and evaluating the influence of the RF switches on the performance of the AMC comparing it to the ideal case.

7.4 SUMMARY OF THE CHAPTER

The reconfigurable antenna presented in this chapter is based on the concept of active AMC ground plane. Artificial magnetic conductors, due to its unique characteristic, which is to provide in-phase reflection phase over certain frequency band(s), have been widely used in low profile antenna designs. Some analytical methods that can be used to analyzing the AMC structure are presented in the beginning of this chapter. For AMC with complex geometries, using numerical methods is required. Our investigations indicate that an antenna (in this study, one coplanar antenna is chosen) with different AMC ground plane can exhibit different resonant frequencies. Therefore, based on these findings, it is decided to mount RF switches on the surface of the AMC that consists of periodic square elements to make it be reconfigurable. By optimizing the dimensions of the AMC and the distance between the AMC and coplanar antenna, the resonant frequency of the coplanar antenna can be reconfigured by using such an active AMC ground plane, whose reflection phase is controlled by the states of the RF switches. Moreover, it is also observed that additional resonant frequency can be created by using the coplanar antenna as a main radiator and the AMC as a coupled element, which behave similar to an antenna of stacked structure.

It is important to point out that in both studies the RF switches are substituted by a short microstrip line to mimic that case that the switches are 'ON' and a small gap to mimic the case that the switches are perfectly 'OFF'. This simplifies the fabrication process; however, it ignores the additional losses introduced by the RF switches, which need to be further investigated in future works. This work has been published in:

1. Q. Luo; J.R. Pereira and H.M. Salgado. Tunable Multiband Antenna With An Active Artificial Magnetic Conductor Ground Plane. In *Proceedings of European Microwave Conference (EuMC)*, Paris, France, October 2010.

8

RECONFIGURABLE DUAL-BAND MONOPOLE ANTENNA ARRAY WITH HIGH ISOLATION

8.1 INTRODUCTION

In Chapter 7, one compact inverted-L antenna array for WLAN 5.8 GHz application has been designed by employing the neutralizing technique. In this chapter, the neutralizing technique is further developed to be applied on a dual band antenna array. The proposed antenna array contains two C-shaped monopoles with a neutralizing line, on which two RF switches were integrated, connecting two arms of the antenna elements. It is demonstrated that by introducing these two RF switches and changing the 'ON' or 'OFF' states of both switches, this compact two C-shaped printed monopoles array can be optimized to separately operate at WLAN 2.4/5.2 GHz band with high isolation. The two antenna elements are closely spaced at a distance of only $0.09\lambda_{2.4GHz}$ and the measurement results indicate that the proposed antenna array has a 10 dB return loss bandwidth that covers the required frequencies for dual-band WLAN applications with an isolation higher than 20 dB over the lower operation band when the RF switches are turned on, and an isolation better than 17 dB at the higher operation band when the switches are turned off. The MIMO performance of the proposed antenna array was analyzed using the envelope correlation coefficient and the total multi-port return loss, which shows that the proposed antenna array has a good diversity and MIMO operational bandwidth at the desired frequency bands.

The antenna design procedure was divided into two stages. At the first stage, two dual band printed monopoles were put in close space to form a compact antenna array. Since the Neutralization Technique can only be used to increase the isolation at singe frequency band, it was decided to implement this method to reach a good isolation between the two antennas at the lower resonant frequency band. This part of work is described in Section 9.3. Then, at the second stage, the objective was to explore possible solutions to improve the isolation at the higher frequency band, which is presented in Section 8.4.

8.2 MOTIVATION

Designing compact printed monopole arrays to support Multiple-Input-Multiple-Output (MIMO) techniques is a challenging work as it is difficult to achieve high isolation between each radiation elements

when they are closely spaced. The existent proposed methods, such as the use of metallic Electromagnetic Band Gap structures on the substrate of the antennas [15] or the Defect Ground System [16] on the ground plane, although they can effectively improve the isolation between two closely space antennas, they are difficult to integrate into the overall system. So far, there are few studies addressing compact multi-band MIMO antenna array designs. In [95], a dual band two antenna array was proposed for USB dongle application. This antenna consists of an L-shape patch and a via trace connecting the via to the ground. Besides the complicated fabrication process, the experimental result provided in [95] shows that the isolation of the antenna array at 2.4 GHz is less than 9 dB. A printed coplanar two-antenna element for 2.4/5 GHz WLAN operation in a MIMO system was presented in [107]. This design employed two single band antennas, which were independently located at the two ends of the PCB board, to realize the dual band operation and high isolation between each other. However, this design is not a real MIMO antenna array as it only contains two single band antennas, each of which resonates at different resonant frequency.

The *Neutralization Techniques* recently proposed in [17] has been successfully applied to the design of a compact ILA array for single band WLAN application in Chapter 7. The neutralizing technique provides an alternative feasible solution to design compact MIMO antenna arrays within limited space. Using this method, the isolation of two antennas could be improved through neutralizing the current of two antennas without the need for adding extra space for antenna design. However, this technique has only be applied to the design of antenna arrays operating at single frequency band and there are not much studies investigating it. Therefore, in this work, it aims to further investigate this technique and apply it to the dual band printed monopole antenna design.

8.3 SINGLE BAND COMPACT ANTENNA ARRAY FOR WLAN 2.4 GHZ

8.3.1 *Antenna Structure*

As described before, the design procedure involves two stages. At the first stage, two printed monopole antennas were put in close space to form a compact antenna array. The geometry of the proposed printed C-shaped monopole antenna array with high isolation at 2.4 GHz band is shown in Figure 149. This antenna is designed on substrate Roger 4003 with thickness of 0.813 mm and relative permittivity of 3.38. The antenna element is printed on one side of the substrate while the ground plane is located at the other side. Figure 149 (a), (b) and (c) present the top, back and side view of the pro-

posed monopole array, respectively. The width of the microstrip line is 1.12 mm and the total length of the C-shape is 36.5 mm. The two C-shaped monopoles are located symmetrically at the left and right side of the substrate and the distance between the two feeding lines is only 11.8 mm, which is around $0.09\lambda_{2.4GHz}$, where $\lambda_{2.4GHz}$ represents the free space wavelength at 2.4 GHz. There is a 0.5 mm wide shorting line connecting the two arms of the monopoles, which takes the role of neutralizing the currents from two monopole antennas to increase their isolation.

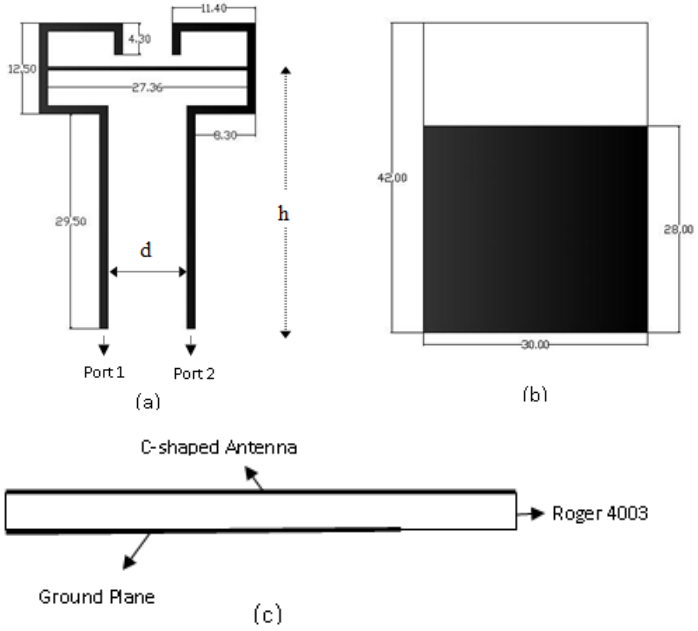

Figure 149: (a)Top view, (b)back view and (c) side view of the proposed antenna array

It is found that the resonant frequency at 2.4 GHz is mainly determined by the total length of the C-shape radiation element. By suitably selecting the total length of the C-shape, the desired resonant frequency can be achieved. Actually this printed monopole antenna can also resonate at another higher frequency; however, at this stage, it only aims to make this antenna array operate properly at the lower band. The operation at the higher band was ignored at this stage but will be investigated in the next stage. The isolation at the desired frequency band is determined by the length of the neutralizing line and its position. According to [17], the neutralizing line should be placed at the position where is surface current is strong (to minimize the influence of the neutralizing line to the original resonant frequency) and the length of it should be approximately a quarter wavelength. Therefore, it can be concluded that after introducing the neutralizing line, in order to achieve the optimum performance in terms of both return loss and isolation at the frequency band of in-

terest, the position and length of the neutralizing line as well as the length of the monopole antenna need to be optimized. The design strategy adopted in this study is to fix the length of the neutralizing line (approximately a quarter wavelength) and looking for the suitable position for it. Some parametrical studies of the location of the neutralizing line have been performed, which will be presented later. More specifically, the dimensions of the ground plane and the width of the shorting line were kept fixed, then the distance h (relatively location on the vertical arms of the C-shaped antenna) was adjusted to find out how this parameter can influence the performance of the proposed antenna array.

8.3.2 *Simulated and Measured Results*

Figure 150 presents the simulated $S11$ and $S12$ of the antenna array with different values for the parameter h. It is observed that increasing the value of h, the central frequency of both the $S11$ and $S12$ of this antenna array also increases. It is also found that the value of h is more critical in determining the isolation at the desired frequency band. Based on these simulation results, the value of h is chosen to be 33 mm. All of the optimization process was carried out by doing numerical simulations in Ansoft HFSS.

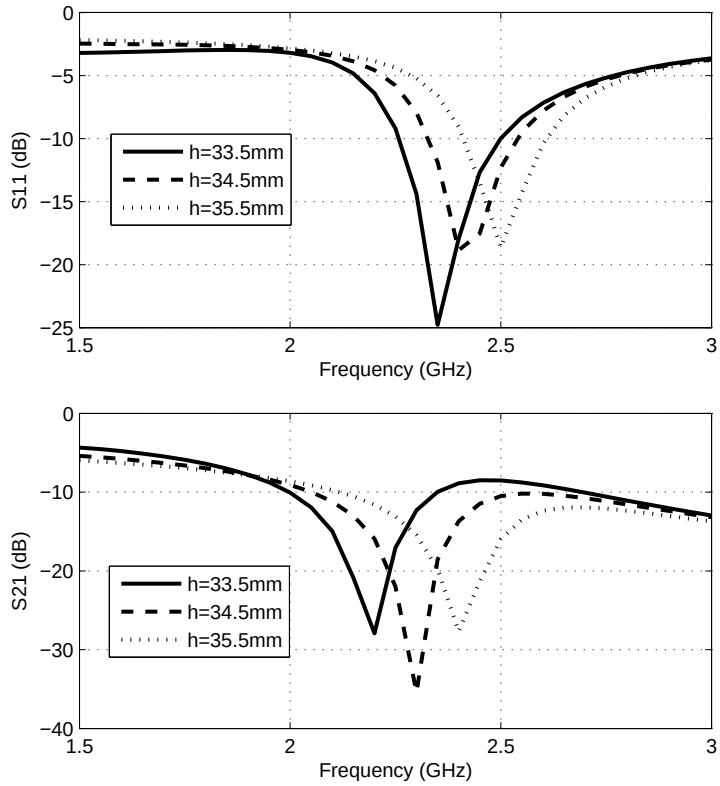

Figure 150: The influence of the location of the neutralizing line to the S11 and S21 for several value of h

Figure 151 (a) and (b) present the simulated surface current distribution of the proposed antenna array with and without the neutralizing line at 2.4 GHz, respectively. It can be seen that with the existence of the neutralizing line, most of the current concentrates on the neutralizing line instead of flowing to the other port, which increases the isolation between the two ports. Therefore, it is expected that the radiation efficiency of the proposed antenna (Figure 151 (a)) should be higher than the one shown in Figure 151 (b) since less energy is lost due to the antenna coupling. This has been confirmed by the simulation results given by HFSS, which predict an efficiency of 96% for the antenna in Figure 151 (a) and an efficiency of 92% in Figure 151 (b).

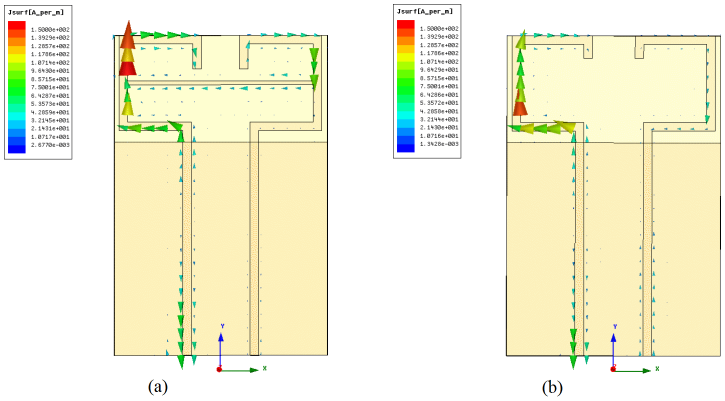

Figure 151: Simulated current distribution of the antenna array: (a) with the neutralizing line; and (b) without the neutralizing line

In order to verify the isolation improvement of the proposed antenna array, two antenna arrays, one with and one without the neutralizing line, have been fabricated and measured. Figure 152 shows the photos of the two fabricated prototypes and Figure 153 presents comparison of the measured isolation ($S21$) between them. It is observed that with the neutralizing line, there is a minimum 7 dB improvement on the isolation over the desired operation frequency band (2.41 to 2.49 GHz).

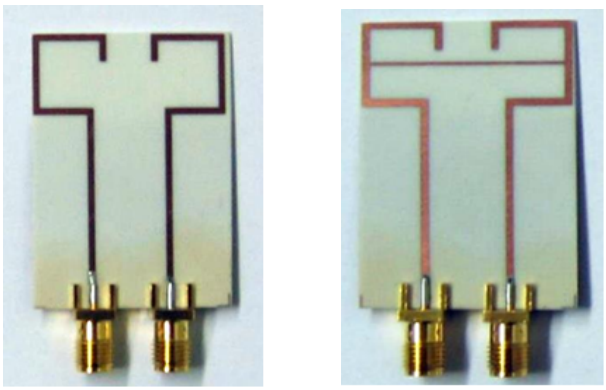

Figure 152: Photos of the fabricated prototypes

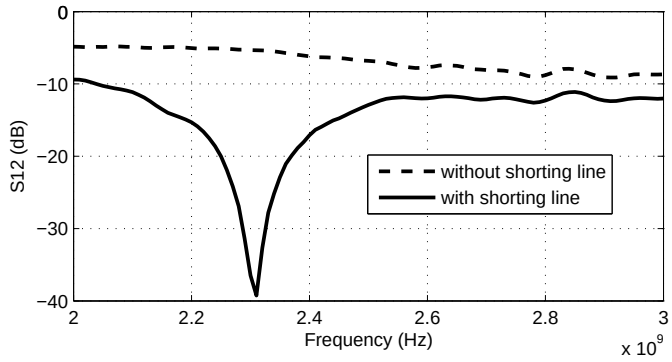

Figure 153: Measured S12 of the C-shaped antenna array with and without the neutralizing line

Figure 154 presents the comparison between the simulated and measured return loss (Figure 154 (a)) as well as the isolation (Figure 154 (b)) of the proposed antenna array.

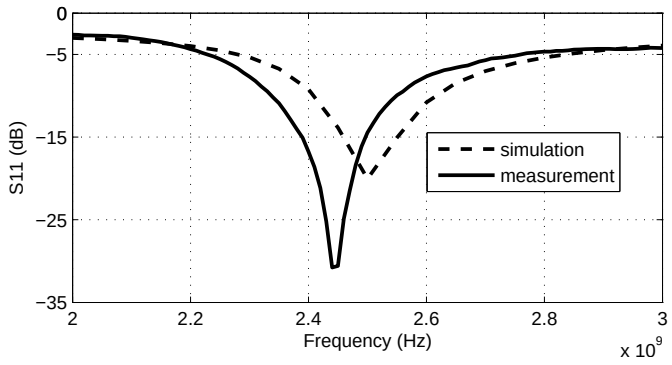

(a)

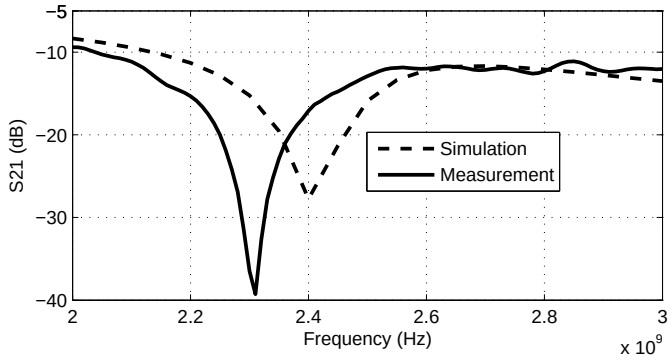

(b)

Figure 154: Comparison of the measured and simulated: (a) S11 and (b) S21 of the proposed C-shaped antenna array

There is some frequency shift (approximately 100 MHz) between the simulated and measured results for both $S11$ and $S21$. The observed frequency shift might be caused by the fabrication error, un-

certainties in the exact permittivity of the substrate and numerical errors in the EM simulation. However, these results confirm that within the interested band (2.41-2.49 GHz), the antenna exhibits good return loss (higher than 15 dB) while the isolation is always higher than 12 dB, which can be seen from the measured return loss and isolation plotted in Figure 155. These results show that the neutralization technique can be successfully implemented on printed monopole antennas and by doing some frequency tuning, it is possible to achieve higher isolation at the desired frequency band. Measurement results show that the proposed antenna array has monopole-like radiation patterns and gain, which is shown in Figure 156. The simulation results indicate that the proposed antenna array has radiation efficiency of 96% at 2.45 GHz.

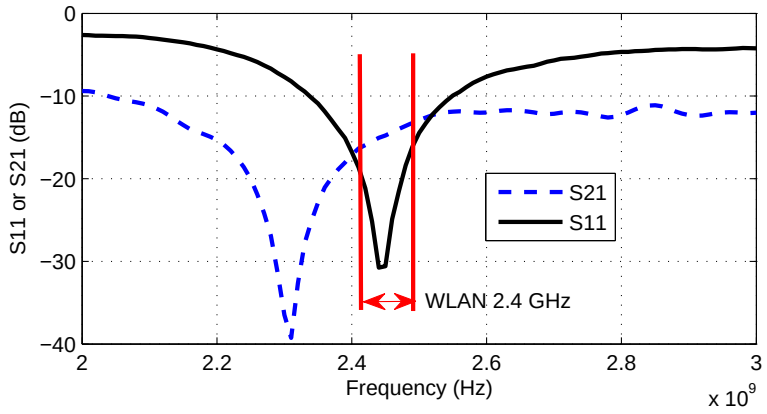

Figure 155: Measure S11 and S21 of the single band printed monopole antenna array at 2.4 GHz

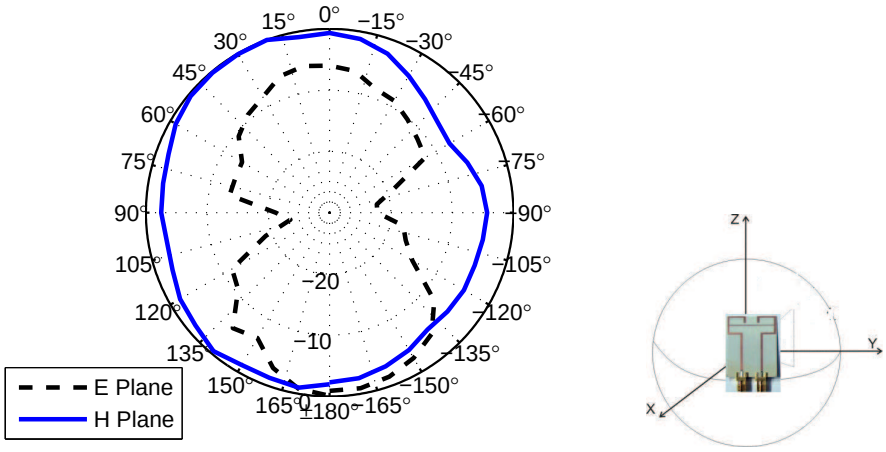

Figure 156: Measured radiation patterns at E plane (X-Z Plane) and H plane (X-Y Plane) of the proposed antenna array with port 1 excited and port 2 connected to a 50ohm load

8.4 RECONFIGURABLE DUAL-BAND MONOPOLE ARRAY WITH HIGH ISOLATION

8.4.1 *Antenna Structure*

At this stage, the neutralizing technique is further developed to work in the scenario of a dual band antennas array. It is clear that the length of the neutralizing line is critical in deciding the frequency band where the antennas have a good isolation. Therefore, in order to employ this technique at a higher frequency band, in our case is WLAN 5.2 GHz, it is necessary to find a way to 'shorten' the neutralizing line. To achieve this, based on the structure studied in Section 9.3, two RF switches were introduced on the neutralization line and by changing the 'ON' or 'OFF' status of the switches, this compact two C-shaped printed monopoles array can separately operate at WLAN 2.4/5.2GHz dual-band with high isolation. Figure 157 shows the structure of the neutralizing line with the RF switches.

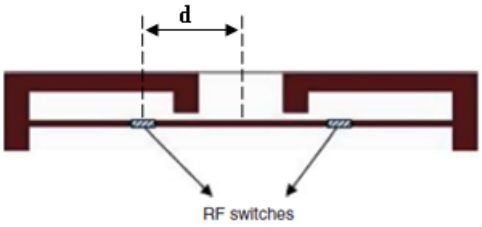

Figure 157: Neutralizing line with two RF switches

When the RF switches are turned on, the antenna array is equal to the one presented in Section 9.3 and the neutralizing line behaves as an inductor as demonstrated in Figure 158 (a). When the RF switches are turned off, the switches behave as two capacitors and the neutralizing line is equivalent to the one demonstrated in Figure 158 (b). In this configuration, the impedance of the capacitor is small at the higher frequencies and the currents can still be neutralized. In this analysis, the resistance of the microstrip line is omitted due to its small value.

In this design, the two C-shaped monopole antennas were printed on the inexpensive FR4 substrate with thickness of 0.8 mm and relative permittivity of 4.4. The dimensions of the antenna was optimized in order to let the antenna operate at 2.4 and 5.2 GHz with a different configuration. The width of the microstrip line is 1.53 mm and the dimensions of the antenna are given in Figure 159. As in the previous design, the antenna element is printed on one side of the substrate, whereas the ground plane is located at the other side. The two C-shaped monopoles are located symmetrically at the left and right side of the substrate. The distance between the two feeding lines is

kept at 10.3mm, which is less than $0.1\lambda_{2.4GHz}$, where λ represents the wavelength in free space. The printed C-shaped monopole can operate at two frequency bands. The first resonant frequency is defined by the total length ($L_1 + L_2 + L_3 + L_4$) of the C-shape, which is 35.6 mm, approximately a quarter wavelength at 2.4 GHz. The second resonant frequency is related to the length of L_3 and L_4, which has a total length of 15.6 mm and is approximately a quarter wavelength at 5.2 GHz.

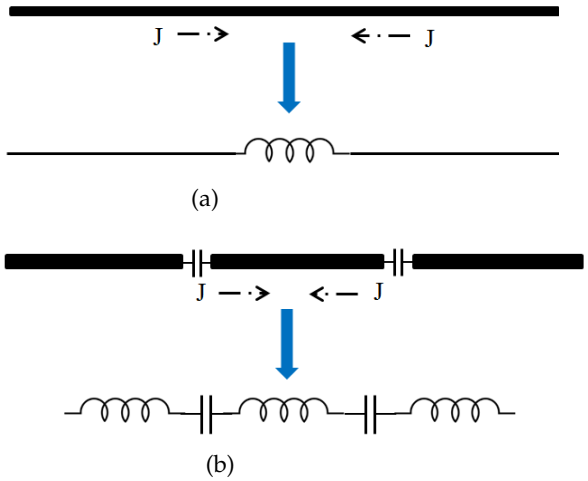

Figure 158: The equivalent circuit structure when: (a) the RF switches are turned ON and (b) the RF switches are turned OFF

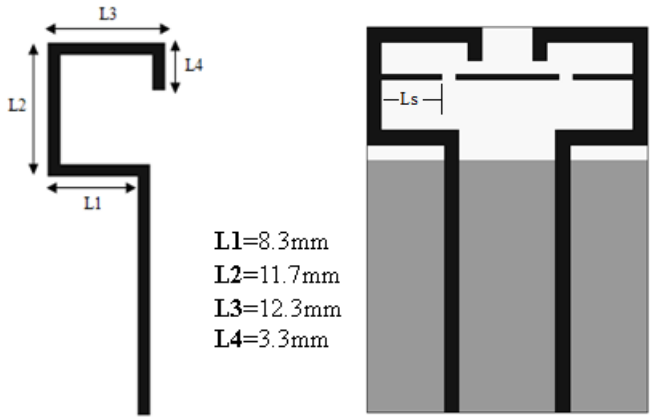

Figure 159: The dimensions of the proposed monopole antenna array. The two slots on the neutralizing line are the positions for RF switches

8.4.2 *Simulated and Measured Results*

In Section 9.3, it has been demonstrated that when using the neutralizing line, to achieve optimum performance in terms of both return loss and isolation, parametrical study of the location of the neutraliz-

ing line is required. In this study, as two RF switches are introduced, the locations of these switches also become critical in determining the operation frequency of the antenna array. Figure 160 shows the simulated return loss and isolation for this antenna array at 5 GHz band with different location of these two RF switches with switches in the 'OFF' state. The parameter d is labeled in Figure 157. As can be seen from these results, the location of the switches is more important in determining the resonant frequency at 5 GHz band while has less effect on the isolation: the isolation is always higher than 15 dB at the desired frequencies.

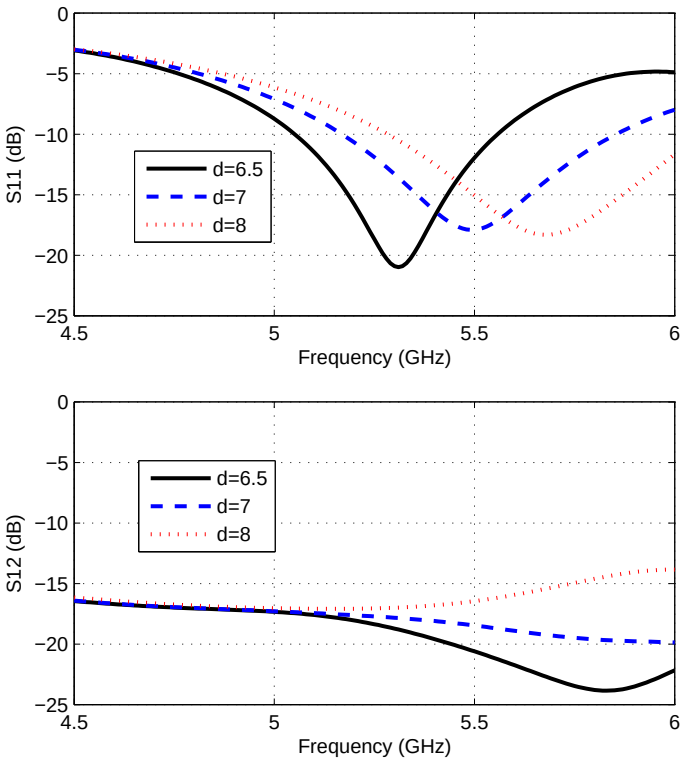

Figure 160: Simulated S11 and S12 of the antenna array with RF switches on different locations with switches in the 'OFF' state

Figure 161 shows the current distribution of the antenna at 2.4 GHz when the switches are turned 'ON' and at 5.25 GHz when the two switches are turned 'OFF'. The light color represents strong current. It is found that when both of the RF switches are turned on, at 2.4 GHz there is strong current on the neutralizing line, which is consistent to the findings in previous studies. When both the RF switches are turned off, the neutralizing line is equivalent to two parallel stubs, each of which connect to the vertical arm of the antenna elements. From the current distribution, it is observed that in this case, at 5.2 GHz the current is concentrated on the antenna and the horizontal stub. The position of the RF switches is selected by firstly choosing

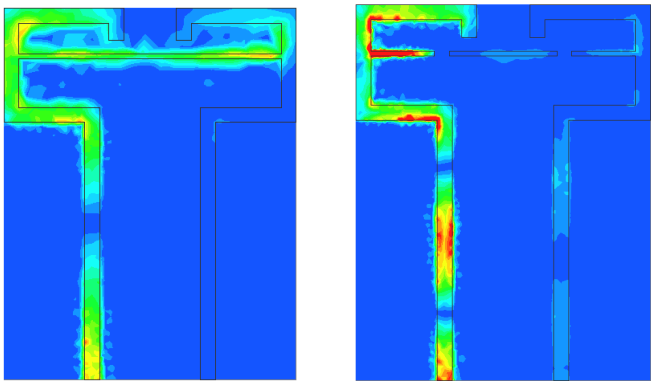

Figure 161: Current distribution at 2.4 GHz (right) when the RF switches are turned 'OFF' and 5.2 GHz (left) when the RF switches are turned 'ON'

the length of the parallel stub approximately a quarter of the effective wavelength at 5.2 GHz, which is:

$$\frac{\lambda_{eff,5.2GHz}}{4} = \frac{\lambda_{0,5.2GHz}}{4\sqrt{\epsilon_{eff}}} \tag{142}$$

while ϵ_{eff} can be calculated by [108]:

$$\epsilon_{eff} = \frac{\epsilon_r + 1}{2} + \frac{\epsilon_r - 1}{2}\left[\frac{1}{\sqrt{1 + 12\left(\frac{H}{W}\right)}} + 0.4(1 - \left(\frac{H}{W}\right))^2\right] \tag{143}$$

where H is the thickness of the substrate and W is width of the microstrip line. Therefore:

$$\frac{\lambda_{eff,5.2\,GHz}}{4} = \frac{\lambda_{0,5.2\,GHz}}{4\sqrt{\epsilon_{eff}}} = 9\,\text{mm} \tag{144}$$

This calculated result is an approximately value and it needs to be optimized through the numerical simulation in HFSS. Due to the adding capacitance from the RF switches, it is expected that the actual value of L_s should be smaller than the one calculated by using Equation 144. After optimization, the value d is chosen to be 6.25 mm, which is equivalent to the length of the stub L_s (see Figure 159) equal to 6.5 mm.

In order to simplify the fabrication process, two antenna prototypes are fabricated: one with a perfect shorting line connecting the two antenna elements to mimic the case that the RF switches are in 'ON' state and one with a shorting line that has two slots of 1.5 mm long on it to mimic the case when the RF switches are in the 'OFF' state (Figure 162).

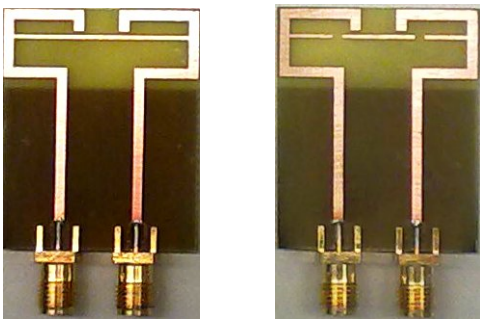

Figure 162: Fabricated two antenna array prototypes on FR4

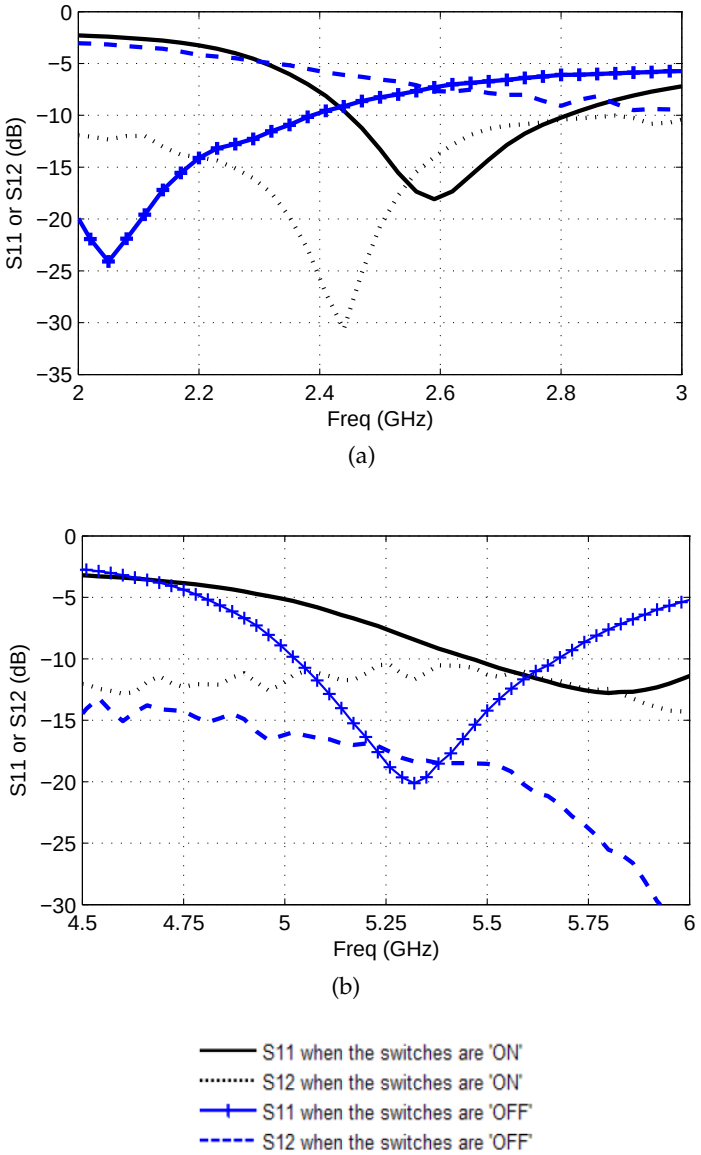

Figure 163: Measured S11 and S12 of the reconfigurable printed monopole array at: (a) 2.4 and (b) 5.2GHz when the switches are turned 'ON' and 'OFF'

Figure 163 shows the measurement return loss (*S*11) and isolation (*S*12) of these two antennas. It can be observed that when the two switches are ideally turned 'ON', the proposed antenna array has a -10 dB bandwidth of 2.44 to 2.55 GHz and isolation better than 20 dB within the desired WLAN 2.4 GHz operation band. Meanwhile, at the higher band the antenna resonates at around 5.75 GHz with a relatively low isolation. When the two switches are ideally turned 'OFF', at the higher band the proposed antenna array can resonate at 5.2 GHz band with a return loss of 20 dB and isolation higher than 17 dB. At this moment, the lower band of the antenna shifts to around 2.05 GHz and its corresponding isolation decreases to less than 5 dB.

Figure 164 presents the simulated 3D radiation patterns of the proposed antenna array at 2.4 GHz and at 5.3 GHz with either port excited. The port 1 is defined as the one in the left side while the port 2 is the right one. As shown in this figure, when different port is excited, the radiation pattern of the antenna array at both resonant frequencies shows different orientation, which contributes to the space diversity of this antenna array.

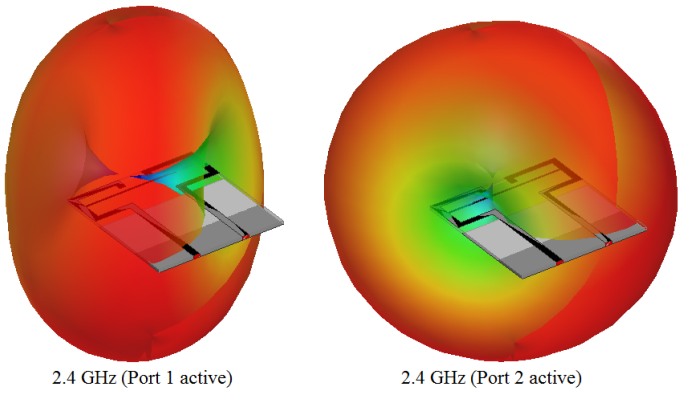

(a)

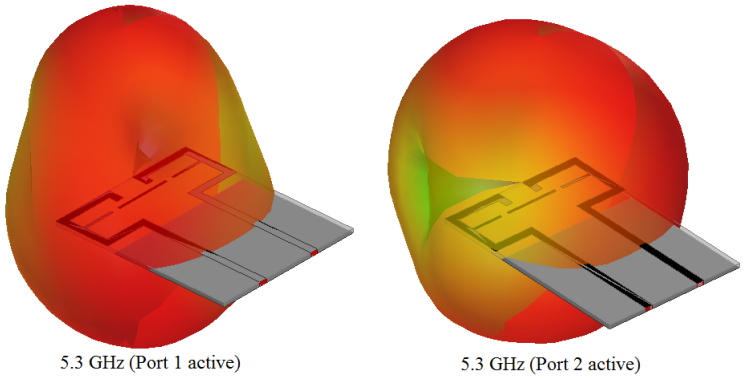

(b)

Figure 164: Simulated 3D radiation pattern of the proposed antenna array at 2.4 GHz and at 5.3 GHz

8.4.3 *MIMO Performance Analysis*

Envelope correlation coefficient is an important parameter to characterize the diversity gain of a MIMO system. Generally, a low envelope correlation always leads to high diversity gain. Usually measurements of the radiation pattern are needed to calculate this parameter. However, if the antenna shows high efficiency, as presented in Chapter 7, a simple formula, which just uses the S matrix, can be employed to derive the envelope correlation coefficient. The simulation results show that the proposed antenna array has radiation efficiency of 95% at 2.45 GHz and radiation efficiency of 89% at 5.3 GHz. Since the proposed antenna exhibits such high efficiency, the simplified formula suggested in Chapter 7 was adopted to calculate its envelope correlation coefficient, which is plotted in Figure 165. The calculated results show that at the desired operation bands the proposed antenna array has an envelope correlation coefficient less than -28 dB. For both antennas, the uncertainty of the calculated envelope correlation coefficient using the simplified equation is less than 0.05 at the lower band and 0.12 at the higher band.

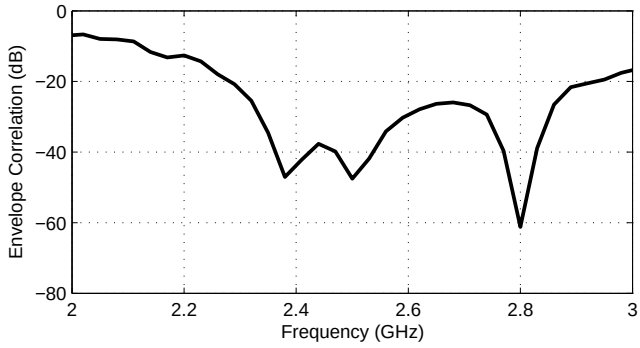

(a)

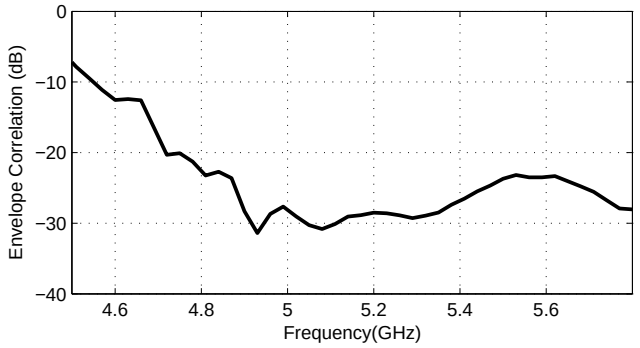

(b)

Figure 165: Calculated envelope correlation coefficient of proposed antenna array: (a) At 2.4 GHz when switches are 'ON'; (b) At 5.2 GHz when switches are 'OFF'

The feasible MIMO operation bandwidth of the proposed antenna array is also evaluated using the Total Multi-port Return Loss (TMRL) method, which is a straightforward approach to obtain the MIMO bandwidth of a multi-port antenna system. Figure 166 shows the calculated TMRL against the measured return loss of the dual band monopole array at 2.4 and 5.2 GHz by using the formulas given in Chapter 7. The calculated TMRL confirms that although the MIMO operation bandwidth of the proposed antenna array is narrower than the single port return loss (S11), it is still within the required frequency range for dual band WLAN application.

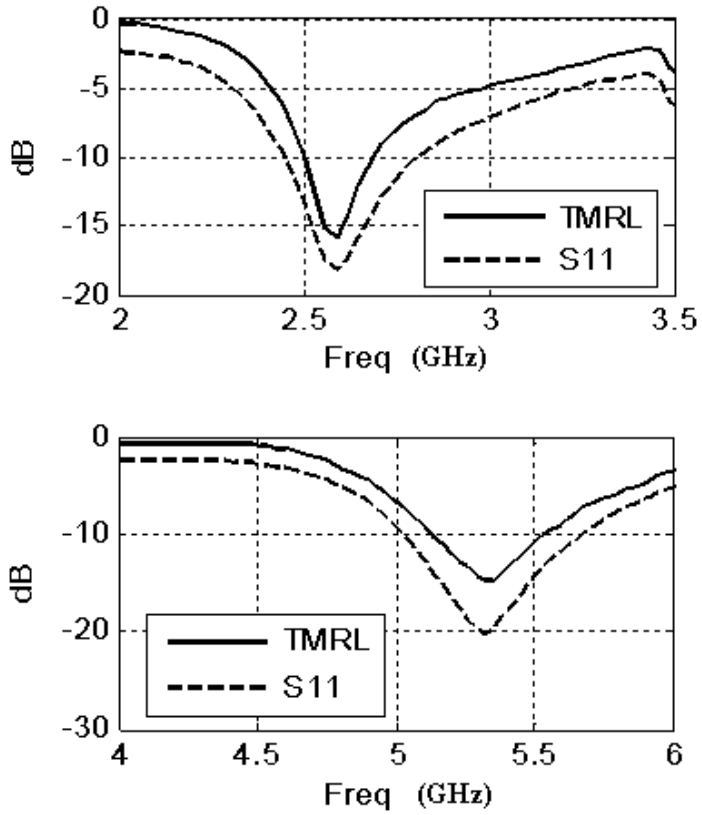

Figure 166: Calculated TMRL against the S11 of the proposed antenna array

8.5 SUMMARY OF THE CHAPTER

In this chapter, two compact monopole antenna arrays for WLAN applications are presented. The objective of this study is to further explore the neutralizing technique and apply it to the design of a dual band antenna array. To achieve this, the design procedure was divided into two stages. The first stage involves designing a C-shaped compact antenna array for the WLAN 2.4 GHz application. From the previous investigation presented in Chapter 5, it is known that this C-shaped antenna can be optimized to operate at dual frequency bands.

Therefore, the task for the second stage turns to investigate possible solutions to extend the neutralization technique to operate at dual frequency bands. The methodology employed to achieve high isolation at two frequency bands is to implement a reconfigurable neutralizing line: two RF switches were introduced on the neutralizing line. By changing the states of these two switches, the antenna array can respectively operate whist exhibit high isolation at each of the WLAN dual frequency band. Experimental results show that the proposed antenna can operate either at 2.4 or 5.2 GHz bands with isolation higher than 17 dB over the entire frequency bands of interest. Moreover, this antenna array also shows low envelope correlation at the required frequency bands, which leads to a good diversity gain. The feasible operational bandwidth of this MIMO antenna array was also analyzed using the TMRL method, which agrees well with the analysis using the envelope correlation coefficient.

The following is the list of publications resulted from the work presented in this chapter:

1. Qi Luo; H. M. Salgado and J. R. Pereira. Compact Printed Monopole Antenna Array for Dual Band WLAN Application. In *Proceedings of International Conference on Computer as a Tool (EUROCON)*, Lisbon, Portugal, November 2011.

2. Q. Luo; H.M. Salgado and J.R. Pereira. Printed C-shaped Monopole Antenna Array With High Isolation For MIMO Applications. In *Proceedings of IEEE Antennas and Propagation Society International Symposium*, Toronto, Canada, July 2010.

3. Q. Luo; J.R. Pereira and H.M. Salgado. Reconfigurable dual band C-shaped monopole antenna array with high isolation. *Electronics Letters*, 46(13):888-889, June 2010.

9 CONCLUSION AND FUTURE WORK

9.1 CONCLUSION

The main objective of this thesis work is to address the miniaturization of multi-frequency microstrip antennas and antenna arrays in the context of high data rate wireless communication. The size of one resonant antenna as well as the distance between each antenna element in an antenna array is proportional to its wavelength. As a result, the size reduction of the antenna or antenna array will inevitably lead to the lowering of the radiation performance of the antenna or antenna array. Therefore, it is always a trade-off between the volume of the antenna and its radiation properties.

The fundamental limitation established by Wheeler and Chu gives a clear guideline for the antenna design: the antenna can be designed to approach this limit but can never be smaller than that. The size reduction of the antennas that were presented in this thesis work is achieved by using fractal geometries or introducing lumped elements into the antenna radiation elements. The new designs presented are three multiband fractal monopole antennas, one fractal-based Inverted-L antenna (ILA) and one single feed fractal monopole antenna array. Moreover, two electrically small antennas for dual band WLAN and one compact antenna for multiband mobile communication that can cover almost the entire commercial available frequency bands (GSM, PCS, UMTS, WLAN and WiMAX) are also presented. The applications of these designs include PC card, USB dongles and mobile devices. The experiment and simulation results prove the effectiveness of the proposed methods in the aspect of antenna size reduction and multi-frequency operation.

The compact multiband antenna array was designed by further investigating the neutralization and employing reconfigurable techniques. The new designs presented in this thesis work include two compact size single band antenna arrays for the WLAN 2.4 GHz and WLAN 5.8 GHz application and one compact dual band compact monopole antennas array for dual band WLAN applications (2.4/5.2 GHz). In these designs, the antennas are closely spaced (less than 1/10th of the wavelength) and the antenna array proposed for the WLAN 5.8 GHz is compact enough to be included in a USB dongle. Another novel work is the design of a reconfigurable antenna based on the concept of active Artificial Magnetic Conductor ground plane. In this proposed antenna, the resonant frequency of the coplanar antenna can be reconfigured by using an active AMC ground plane

whose reflection phase is controlled by the status of the RF switches. Moreover, additional resonant frequencies were induced using the coplanar antenna as a main radiator and the AMC as a coupled element, which behave similar to an antenna of stacked structure.

The proposed antennas presented in this thesis work either have compact size or low profile with moderate bandwidth and high radiation efficiency. Furthermore, the antennas are completely planar, which makes them easy to be fabricated with low cost. It is important to point out that in the studies of reconfigurable antennas, the RF switches were substituted by a short microstrip line to mimic the case that the switches are 'ON' and a small gap to mimic the case that the switches are perfectly 'OFF'. This simplifies the fabrication process; however, it ignores the additional losses introduced by the RF switches, which need to be further investigated in future work.

9.2 FUTURE WORK

9.2.1 *Electrically Small Antenna with 3D structure*

The antenna is one of the most critical components in determining the performance of the communication system. Besides being capable of supporting multiband operation, it is also important that they have low profile, be compact, lightweight and easy to fabricate because of the industry requirements. Based on the definition from Wheeler and Chu, it can be referred that the fundamental limits of an antenna can be approached if the antenna has a structure that can better make use of the sphere that surrounds it. This means that in order to further reduce the size of the antenna, it is necessary to adopt a 3D structure. Although there exists many designs that bent the antenna structure to reduce the volume occupied by the antenna, it is believed that the miniaturization of such designs can still be improved. In this thesis work, all of the antennas are designed to have a simple planar structure with the consideration of easy fabrication. The techniques proposed in this thesis work can be utilized with the concept of 3D antenna design to further reduce the volume of the antennas. It is important to emphasize that there is always a trade-off between the antenna volume and its radiation performance. Figure 167 present two different electrically small antennas designed for the car key application at 868 MHz.

Both of these two antennas are designed for the remote car key under the Zigbee standard at 868 MHz. The antennas are designed on an inexpensive Fr4 substrate with dimensions of 10 mm $\times$ 10 mm. The thickness of the substrate is 1.6 mm for the first design and 0.8 mm for the second design. The main differences between these two designs is that the 1st antenna only uses a planar structure whilst the second design has a 3D wrapped structure. Figure 168 presents the

simulated return loss of both antennas. It can be seen that from the simulation results, both antennas have promising bandwidth at the desired frequency.

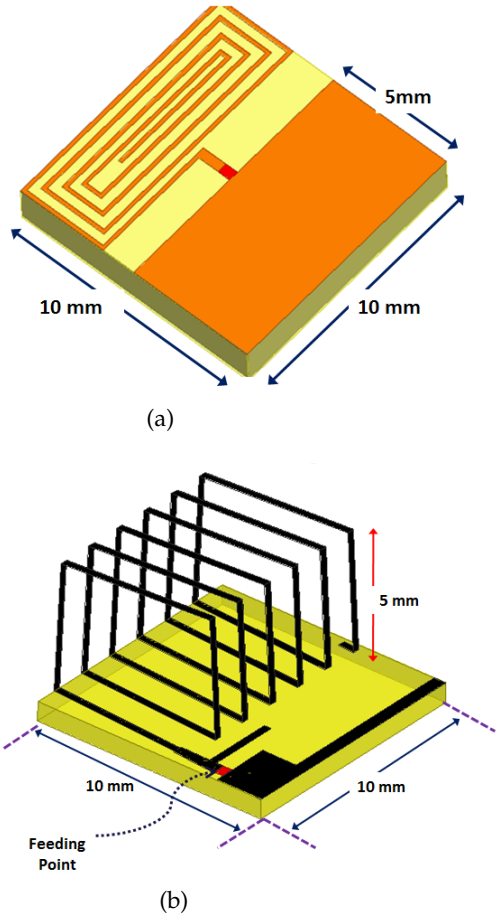

Figure 167: Two electrically small antennas designed for the car key application at 868 MHz. (a) Design 1, which has a planar structure; (b) Design 2, which has a 3D structure

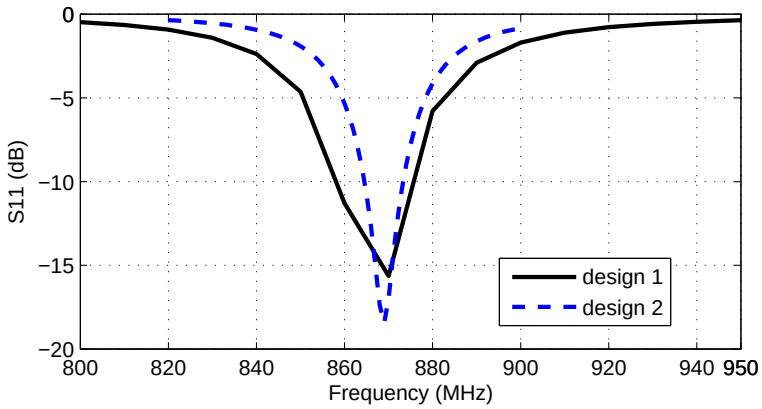

Figure 168: The simulated return loss of both proposed electrically small antennas

However, in the aspect of radiation efficiency, the simulation results show that for the 1st design, the radiation efficiency is only 1% whereas for the 2nd design the radiation efficiency can reach 16%. The trade-off between the antenna volume and antenna radiation performance as well as the advantage of using a 3D antenna structure is quite clear from this point. Table 9 presents the calculation of the quality factor of each antenna and its theoretical lower bound, which shows that the 2nd design has a quality factor very close to the Chu's limits. Therefore, in order to further reduce the size of the antenna whilst maintain its good radiation characteristics, employing antenna of 3D structure with acceptable fabrication complexity should be further investigated.

Table 9: The quality (Q) factor of the designed two antennas

	Antenna 1	Antenna 2
-10dB Bandwidth	20 MHz	9 MHz
Radiation Efficiency	1%	15.8%
Quality Factor (Q)	34	69
Q Lower Bound	4.9	59.6

9.2.2 *Multiband Compact MIMO Antenna Array*

Another field that needs to be further investigated in future is to design compact multiband MIMO antenna arrays. Both the 4G mobile network (LTE) and the recently announced IEEE 802.11n standard require the wireless devices to support MIMO. To place one antenna array on a portable device, it is important to keep the isolation between each antenna at a promising level. Take LTE system as an example, one of the suggested frequency bands in Europe is 900 MHz whilst in America it is required to have a lower band operating at 700 MHz. Given the fact that in a portable device the distance between each antenna element has to be relatively small compared to the wavelength at the desired frequency and since it is also desirable to have one antenna or antenna array that can operate at WLAN and WiMAX frequencies, it is important to be able to design very compact MIMO antennas array that can operate at six or even more frequency bands. This is a challenge that has not been solved yet.

To design such a compact antenna array for a portable device, the antenna element itself must be of compact size. In this thesis work, it has been proved that the use of either fractal geometry or chip inductor into the antenna design can result in multiband antennas with reduced or even electrically small size. Is it possible to employ these techniques into the compact antenna array design? In order to make

use of the available volume, it is necessary to 'wrap' the antennas to obtain a three-dimensional structure. As a result, it is necessary to assess the impact of bending the radiation element on a normal planar fractal antenna. Another solution that can be introduced into the antenna array design is to embed the chip inductors on the single radiation element, which has been studied in this thesis work and proved to be an effective method to reduce the size of one single antenna. With respect to improve the isolation between each antenna, especially at multiple frequency bands, more innovative techniques are required. It is shown that introducing the reconfigurable method to the neutralizing technique, a compact dual band antenna array with high isolation can be implemented. Is it possible to achieve high isolation at three or even more frequency bands by adding extra RF switches on the radiation element, feeding line or ground plane besides on the neutralizing line? Under this configuration, one frequency tunable antenna with a reconfigurable neutralizing line might be achieved after suitable optimization, including the location of the RF Switches, lumped elements and the input impedance matching at multiple resonant frequencies. This is one direction that is worth exploring both theoretically and experimentally.

To the date of writing this thesis, one of the first published designs of the multiband antenna array for LTE applications was presented in [109]. In that design, both antennas were located at the bottom of the PCB board and the distance between antennas is relatively small compared to the lowest resonant frequency, which is 700 MHz for LTE standard. There are two things needed to be highlight in this design. Firstly, the size reduction of both of the antennas were achieved by wrapping the resonant element to form a 3D structure and embedding one chip inductor on the antenna to induce the lowest resonant frequency. Secondly, the high isolation between the antennas was reached by adding one protruded ground plane. The results provided in [109] show that the proposed antenna array can perform LTE MIMO operation in the LTE700/ 2300/2500 bands. Although that this antenna array does not cover all the required LTE bands, it shows clearly that to achieve a compact multiband antenna array, different antenna and antenna array miniaturization techniques need to be implemented simultaneously.

Metamaterial inspired antenna is another interesting field that worth investigating further. Electromagnetic band gap (EBG) material and artificial magnetic conductor (AMC) have already been widely employed in the low profile antenna design with increased radiation performance. However, the use of periodic structures will lead to a relatively large overall volume, which is not suitable for antenna miniaturization. Therefore, future trends of using such artificial materials into the compact antenna design should employ less or single metamaterial cells to design double negative (DNG) zeroth order

resonator (ZOR), a subject which have attracted much research interest. Theoretically the size of one antenna designed using ZOR is not proportional to its corresponding wavelength, which can be advantageous to design antennas for low frequencies applications. It is also known that metamaterial can also be employed to suppress the propagation of surface waves, which is one of the first applications of such artificial materials. Then, using metamaterial inspired antenna to design compact antenna array with high isolation becomes another possible approach. The surface wave suppressing brought by the metamaterials has been widely studied; however, the operation of the metamaterial inspired antenna is still not well understood and requires to be further investigated. One key issue for the design of metamaterial inspired antenna array is how to make the operational frequency band of the antenna and surface wave suppressing band of the metamaterial to be within the same frequency region. One more challenge is that, looking at the existing publications, it is found that the metamaterial inspired antenna reported to date have a relatively narrow bandwidth, which needs to be improved in future work.

BIBLIOGRAPHY

[1] *Qualcomm: http://qualcomm.com/technology*, Retrieved 30 August 2011. (Cited on page 1.)

[2] Motorola. Long Term Evolution (LTE). Technical report, Retrieved 12 August 2011. (Cited on page 2.)

[3] IEEE-SA. IEEE 802.11n-2009-Amendment 5: Enhancements for Higher Throughput. Technical report, 2009. (Cited on page 2.)

[4] Ke-Lin Du and M. N. S. Swamy. *Wireless Communication Systems: From RF Subsystems to 4G Enabling Technologies*. Cambridge University Press, 2010. (Cited on page 3.)

[5] B.B.Mandelbrot. *The Fractal Geometry of Nature*. N.Y.W.H.Freeman, 1983. (Cited on page 3.)

[6] D.H.Werner and S.Ganduly. An Overview Of Fractal Antenna Engineering Research. *IEEE Antennas and Propagation Magazine*, 45(1):38–57, 2003. (Cited on pages 3 and 51.)

[7] G.G.Chavka. Beauty Of Fractals, Design Of Fractal Antennas. In *Proceedings of International Conference on Antenna Theory and Techniques*, 2007. (Cited on page 3.)

[8] R. Mitrra. A Critical Look At The Problem Of Small Antenna Design And A Review Of Physics-Based Performance Limitations Of These Antenna. In *Proceedings of Loughborough Antennas and Propagation Conference*, UK, March 2008. (Cited on page 3.)

[9] J.P.Gianvittorio and Y.Rahmat-Samii. Fractal Antennas: A Novel Antenna Miniaturization Techniques, And Applications. *IEEE Antennas and Propagation Magazine*, 44(1):20–36, 2002. (Cited on pages 3 and 51.)

[10] Gerald Edgar. *Measure, Topology, and Fractal Geometry (2nd Edition)*. Springer Science, 2008. (Cited on pages 4 and 42.)

[11] O.Q.Teruel; E.Pucci and E.R.Iglesias. Compact Loaded PIFA for Multifrequency Application. *IEEE Transactions on Antennas and Propagation*, 58(3):656–664, 2010. (Cited on pages 4 and 92.)

[12] B.R.Holland; R.Ramadoss; S.Pandey and P.Agrawal. Tunable coplanar patch antenna using varactor. *Electronic Letters*, 42(6):319–321, 2006. (Cited on pages 4 and 6.)

[13] K.Wong and S.Chen. Printed Single-Strip Monopole Using A Chip Inductor For Penta-Band WWAN Operation In The Mobile Phone. *IEEE Transactions on Antennas and Propagation*, 58(3):1011–1014, 2010. (Cited on pages 4, 92, and 112.)

[14] T. Kang and K.Wong. Chip-Inductor-Embedded Small-Size Printed Strip Monopole For WWAN Operation In The Mobile Phone. *Microwave and Optical Technology Letter*, 51(4):966–971, 2009. (Cited on pages 4 and 92.)

[15] F.Yang and Y. Rahmat-Samii. Microstrip Antennas Integrated With Electromagnetic Band-Gap (EBG) Structures: A Low Mutual Coupling Design for Array Applications. *IEEE Transactions on Antennas and Propagation*, 51(10):2936–2946, 2003. (Cited on pages 5 and 158.)

[16] A. Tavakoli M. Salehi; A. Motevasselian and T. Heidari. Mutual Coupling Reduction of Microstrip Antennas using Defected Ground Structure. In *Proceeding of 10th IEEE Singapore International Conference on Communication systems*, 2006. (Cited on pages 5 and 158.)

[17] C.Luxey. Design of Multi-Antenna Systems for UMTS Mobile Phones. In *Preceeding of Loughborough Antenna & Propagation Conference, UK*, 2009. (Cited on pages 5, 10, 129, 130, 131, 158, and 159.)

[18] A.Diallo; C.Luxey; P.L.Thu; R.Staraj and G.Kossiavas. Enhanced two-antenna structures for universal mobile telecommunications system diversity terminals. *IET Microwave and Antenna Propagation*, 2(1):93–101, 2008. (Cited on page 5.)

[19] A. Diallo;C. Luxey; P. Le Thuc; R. Staraj and G. Kossiavas. Efficient two-port antenna system for GSM/DCS/UMTS multimode mobile phones. *Electronic Letters*, 43(7):369–370, 2007. (Cited on page 5.)

[20] A.S.; Gyubok Park; Minchan Kim; Taesik Yang; Joonho Byun; Kim. The compact quad-band mobile handset antenna for the LTE700 MIMO application. In *Proceedings of IEEE Antennas and Propagation Society International Symposium*, 2009. (Cited on page 5.)

[21] E. Del Re; S. Morosi; D. Marabissi; L. Mucchi; L. Pierucci and L. S. Ronga;. Reconfigurable Antenna for FutureWireless Communication Systems. *Wireless Personal Communications (Springer)*, 42:405–430, 2007. (Cited on page 6.)

[22] N.P. Cummings. *Active Antenna Bandwidth Control Using reconfigurable antenna elements*. PhD thesis, Faculty of the Viginia Polytechnic Institure & State University, 2003. (Cited on page 6.)

[23] D. Peroulis; K. Sarabandi and L. P. B. Katehi;. Design of Reconfigurable Slot Antennas. *IEEE Transactions on Antennas and Propagation*, 53(2):645–654, 2005. (Cited on page 6.)

[24] F.Yang. *EBG Structure and Reconfigurable Techniques in Antenna Design: Application to Wireless Communications*. PhD thesis, Department of Electrical Engineering, University of California, 2003. (Cited on page 6.)

[25] V.K. Kunda and M. Ali;. Reconfigurable stacked patch antenna for satellite and terrestrial applications. In *Proceedings of IEEE Topical Conference on Wireless Communication Technology*, pages 152–153, 2003. (Cited on page 6.)

[26] S.Oh; J. T. Aberle; S. Anantharaman; K. Arai; H. L.Chong and S. C. Koay;. Electronically Tunable Antenna Pair and Novel RF Front-End Architecture for Software-Defined Radios. *EURASIP Journal on Applied Signal Processing*, 2005:2701–2707, 2005. (Cited on page 6.)

[27] G. Goussetis; A.P. Feresidis and J.C. Vardaxoglou;. Tailoring the AMC and EBG Characteristics of Periodic Metallic Arrays Printed on Grounded Dielectric Substrate. *IEEE Transactions on Antennas and Propagation*, 54(1):82–89, 2006. (Cited on page 7.)

[28] Dan Sievenpiper; Lijun Zhang; Romulo F. Jimenez Broas; Nicholas G. Alexopolous and Eli Yablonovitch;. High-Impedance Electromagnetic Surfaces with a Forbidden Frequency Band. *IEEE Transactions on Antennas and Propagation*, 47(11):2059–2074, 1999. (Cited on page 7.)

[29] F.Costa; S.Talarico; A.Monorchio and M.F.Valeri. An active AMC ground plane for tunable low-profile antennas. In *Proceeding of IEEE Antenna and Propagation Society international Symposium*, 2008. (Cited on pages 7 and 147.)

[30] J.Liang and H.Y.D.Yang. Microstrip Patch Antenna on Tunable Electromagnetic Band-Gap Substrate. *IEEE Transactions on Antennas and Propagation*, 57(6):1612–1617, 2009. (Cited on pages 7 and 147.)

[31] D. H. Werner; D. J. Kern and M. G. Bray. Advances in EBG Design Concepts Based on Planar FSS Structures. In *Proceedings of the Loughborough Antennas and Propagation Conference*, 2005. (Cited on pages 7 and 147.)

[32] L.J.Rocha; M.Martinez-Vazquez and R.S.Calvo, editors. *Hand-Book on Small Antennas (Special Draft Edition)*. Universitat Politecnica de Catalunya, Spain, 2011. (Cited on page 15.)

[33] W.Yu; X.Yang; Y.Liu; Z.Li; R.Mittra; L.Li and N.Huang. *Electromagnetic Simulation Engineering*. Pennsylvania State University, USA, 2010. (Cited on page 15.)

[34] D. Manteuffel. Numerical technique. Lecture notes for Europen Antenna School on Industry Antenna Design, April 2011. (Cited on page 15.)

[35] R. F. Harrington. *Field computation by moment methods*. Macmillan, 1968. (Cited on page 15.)

[36] K.Yee. Numerical solution of initial boundary value problems involving maxwell's equations in isotropic media. *IEEE Transactions on Antennas and Propagation*, 14:302–307, 1966. (Cited on page 17.)

[37] P.P.Silvester. Finite elements solution of homogeneous waveguide problems. *Alta Freq.*, 38:313–317, May 1969. (Cited on page 21.)

[38] K.K.Mei. Unimoment method of solving antenna and scattering problems. *IEEE Transactions on Antennas and Propagation*, 22:760–766, November 1974. (Cited on page 21.)

[39] J.M.Jin. *The finite element method in electromagnetics (2nd)*. John Wiley & SONS, INC, 2002. (Cited on pages 21, 22, 30, 32, and 33.)

[40] A.C.Polycarpou. *Introduction to the finite element method in electromagnetics*. Morgan & Claypool, 2006. (Cited on pages 22, 23, 24, 25, and 28.)

[41] Hyochoong Bang Young W.Kwon. *The Finite Element Method using MATLAB*. CRC Press, 1997. (Cited on page 31.)

[42] Benoit B. Mandelbrot. *The Fractal Geometry of Nature*. W. H. Freeman and Company,New York, 1982. (Cited on page 41.)

[43] Kenneth Falconer. *FRACTAL GEOMETRY:Mathematical Foundations and Applications(2nd Edition)*. John Wiley & Sons, 2003. (Cited on pages 41 and 44.)

[44] Stephen Demko. Construction of fractal objects with iterated function systems. In *SIGGRAPH '85 Proceedings of the 12th annual conference on Computer graphics and interactive techniques*, volume 19, 1985. (Cited on page 43.)

[45] Ansoft. *HFSS Scripting Guide: HFSS and VBScript*, 2010. (Cited on page 46.)

[46] David M. Pozar. *Microwave engineering*. J. Wiley, 2005. (Cited on page 48.)

[47] J Anguera; C Puente and J Soler. Miniature monopole antenna based on the fractal hilbert curve. *IEEE Antennas and Propagation Society International Symposium*, 4:546–549, 2002. (Cited on page 51.)

[48] G.F.Tsachtsiris; C.F.Soras; M.P.Karaboikis and V.T.Makios. Analysis of a modified sierpinski gasket monopole antenna printed on dual band wireless devices. *IEEE Transactions on Antennas and Propagation*, 52(10):2571–2579, 2004. (Cited on page 51.)

[49] S.R.Best and J.D.Morrow. The effectiveness of space-filling fractal geometry in lowering resonant frequnency. *IEEE Antennas and Wireless Propagation Letter*, 1:112–115, 2002. (Cited on pages 51 and 85.)

[50] S.R.Best. A discussion on the significance of geometry in determining the resonant behaviour of fractal and other non-euclidean wire antennas. *IEEE Antennas and Propagation Magazine*, 45(3):9–28, 2003. (Cited on page 51.)

[51] W.C.Su and K.L.Wong. Internal pifas for umts/wlan/wimax multi-network for a usb dongle. *Microwave and Optical Technology Letters*, 48:2249–2253, 2006. (Cited on page 59.)

[52] C.C.Lin; S.W. Kuo and H.R. Chuang. A 2.4-ghz printed meander-line antenna for usb wlan with notebook-pc housing. *IEEE Microwave and Wireless Components Letters*, 15(9):546–548, 2005. (Cited on page 59.)

[53] Y. Song; Y.C.Jiao and ed. Compact printed monopole antenna for multiband wlan applications. *Microwave and Optical Technology Letters*, 50(2):365–367, 2008. (Cited on page 59.)

[54] N.Cohen. Fractal antenna applications in wireless telecommunications. In *Electronics Industries Forum of New England, 1997. Professional Program Proceedings*, pages 43 – 49, 1997. (Cited on page 60.)

[55] R.R.Ramirez; F. De Flaviis; N.G.Alexopoules. Single feed circularly polarized microstrip ring antenna aiid arrays. *IEEE Transactions on Antennas and Propagation*, 48(7):1040 – 1047, 2000. (Cited on page 73.)

[56] A.E.Abdulhadi and A.R.Sebak. Single feed circularly polarized microstrip antenna array. In *2nd International ITG Conference on Antennas*, pages 162 – 165, 2007. (Cited on page 73.)

[57] T.Y.Wu; S.T.Fang and K.L.Wong. Printed monopole array antenna for wlan operation in the 2.4/5.2/5.8ghz bands. *Microwave and Optical Technology Letters*, 37(5):370–372, 2003. (Cited on page 73.)

[58] Q. Luo; H. M. Salgado; J. R. Pereira. Fractal monopole antenna design using minkowski island geometry. In *IEEE International Symposium on Antennas & Propagation Proceeding*, 2009. (Cited on page 73.)

[59] C.Y.Pan; T.S.Horng; W.S.Chen and C.H.Huang. Dual wideband printed monopole antenna for wlan/wimax applications. *IEEE Antenna and Wireless Propagation Letters*, 6:149–151, 2007. (Cited on pages 73 and 75.)

[60] M.John and M.J.Ammann. Wideband printed monopole design using a genetic algorithm. *IEEE Antenna and Wireless Propagation Letters*, 6:447–449, 2007. (Cited on page 73.)

[61] H.A.Wheeler. Fundamental limitations of small antennas. *Proceedings of the I.R.E.*, 35(12):1479–1484, December 1947. (Cited on pages 85 and 86.)

[62] R.B.Adler; L.J.Chu and R.M.Fano. *Electromagnetic Energy Transmission and Radiation*. New York: Wiley, 1960. (Cited on page 85.)

[63] S.R.Best. *Antenna Engineering Handbook*. McGraw-Hill, fourth edition edition, 2007. (Cited on page 85.)

[64] L.J.Chu. Physical limitations of omni-directional antennas. *J.Appl.Phys.*, 19:1163–1175, December 1948. (Cited on pages 86 and 87.)

[65] R.C.Hansen. Fundamental limitations in antennas. *Proceedings of the IEEE*, 69(2):170–182, February 1981. (Cited on page 86.)

[66] J.S.McLean. A re-examination of the fundamental limits on the radiation q of electrically small antennas. *IEEE Transactions on Antennas and Propagation*, 44(5):672–676, May 1996. (Cited on page 87.)

[67] A.D.Yaghjian and S.R.Best. Impedance, bandwidth, and q of antennas. *IEEE Transactions on Antennas and Propagation*, 53(4):1298–1234, April 2005. (Cited on page 87.)

[68] Coicraft. www.coicraft.com. Technical report, Retrieved 10 March 2011. (Cited on page 88.)

[69] J.Xiong; Z.Ying and S.He. A broadband low profile patch antenna of compact size with three resonances. *IEEE Transactions on Antennas and Propagation*, 57(6):1838–1843, 2009. (Cited on page 92.)

[70] O.Kramer; T.Djerafi and K.Wu. Vertically multilayer-stacked yagi antenna with single and dual polarizations. *IEEE Transactions on Antennas and Propagation*, 58(4):1022–1030, 2010. (Cited on page 92.)

[71] M.Z.Azad and M.Ali. A miniature implanted inverted-f antenna for gps application. *IEEE Transactions on Antennas and Propagation*, 57(6):1854–1858, 2009. (Cited on page 92.)

[72] D.D.Krishna; M.Gopikrishna; C.K.Aanandan; P.Mohanan and K.Vasudevan. Compact wideband koch fractal printed slot antenna. *IET Microwave and Antenna Propagation*, 3(5):782–789, 2009. (Cited on page 92.)

[73] B.Ghosh; SK.M.Hauqe; D.Mitra and S.Ghosh. A loop loading technique for the miniaturization of non-planar and planar antennas. *IEEE Transactions on Antennas and Propagation*, 58(6):2116–2121, 2010. (Cited on page 92.)

[74] J.Zhu; M.A.Antoniade and G.V.Eleftheriades. A compact triband monopole antenna with single cell metamaterial loading. *IEEE Transactions on Antennas and Propagation*, 58(4):1031–1038, 2010. (Cited on page 92.)

[75] J.Park; Y.Ryu; J.Lee and J.Lee. Epsilon negative zeroth-order resonator antenna. *IEEE Transactions on Antennas and Propagation*, 55(12):3710–3712, 2007. (Cited on page 92.)

[76] J.Park; Y.Ryu and J.Lee. Mu-zero resonance antenna. *IEEE Transactions on Antennas and Propagation*, 58(6):1865–1875, 2010. (Cited on page 92.)

[77] K.L.Wong and C.H.Huang. Compact multiband pifa with a coupling feed for internal mobile phone antenna. *Microwave and Optical Technology Letter*, 50(10):2487–2491, 2008. (Cited on page 111.)

[78] C.H.Chang; K.L.Wong and J.S.Row. Coupled-fed small-size pifa for penta-band folder-type mobile phone application. *Microwave and Optical Technology Letter*, 51(1):18–23, 2009. (Cited on page 111.)

[79] C.I.Lin and K.L.Wong. Printed monopole slot antenna for penta-band operation in the folder-type mobile phone. *Microwave and Optical Technology Letter*, 50(9):2237–2242, 2008. (Cited on page 111.)

[80] F.H.Chu and K.L.Wong. Simple folded monopole slot antenna for penta-band clamshell mobile phone application. *IEEE Transactions on Antennas and Propagation*, 57(11):3680–3684, 2009. (Cited on page 111.)

[81] K.L.Wong and C.H.Huang. Printed loop antenna with a perpendicular feed for penta-band mobile phone application. *IEEE Transactions on Antennas and Propagation*, 56(7):2138–2141, 2008. (Cited on page 111.)

[82] C.I.Lin and K.L.Wong. Internal meandered loop antenna for gsm/dcs/pcs multiband operation in a mobile phone with the user's hand. *Microwave and Optical Technology Letter*, 49(4):759–765, 2007. (Cited on page 111.)

[83] Y.W.Chi and K.L.Wong. Half-wavelength loop strip capacitively fed by a printed monopole for penta-band mobile phone antenna. *Microwave and Optical Technology Letter*, 50(10):2549–2554, 2008. (Cited on page 111.)

[84] P.Ciais; R.Staraj; G.Kossiavas and C.Luxey. Compact internal multiband antenna for mobile phone and wlan standards. *Electronic Letters*, 40(15):920–921, 2004. (Cited on page 112.)

[85] C.I.Lin and K.L.Wong. Printed monopole slot antenna for internal multiband mobile phone antenna. *IEEE Transactions on Antennas and Propagation*, 55(12):3690–3697, 2007. (Cited on page 112.)

[86] H.W.Hsieh; Y.C.Lee; K.K.Tiong and J.S.Sun. Design of a multiband antenna for mobile handset operation. *IEEE Antennas and Wireless Propagation Letters*, 8(12):200–203, 2009. (Cited on page 112.)

[87] A.C.K.Mak; C.R.Rowell; R.D.Murch and C.L.Mak. Reconfigurable multiband antenna designs for wireless communication devices. *IEEE Transactions on Antennas and Propagation*, 55(7):1919–1928, 2007. (Cited on page 112.)

[88] J.K.Ji; G.H.Kim and W.M.Deong. A compact multiband antenna based on dng zor for wireless mobile system. *IEEE Antennas and Wireless Propagation Letters*, 8:920–923, 2009. (Cited on page 112.)

[89] Ansoft HFSS. *Ansoft High Frequency Structure Simulator v10 User's Guide*, rev 1.0 edition, June 2005. (Cited on page 120.)

[90] R.G.Vaughan; J.B.Andersen. Antenna diversity in mobile communications. *IEEE Transactions on Vehicular Technology*, VT-36(4):149–172, November 1987. (Cited on pages 125 and 126.)

[91] S.Blanch; J.Romeu and I.Corbella. Exact representation of antenna system diversity performance from input parameter description. *Electronics Letter*, 39(9):705–707, 2003. (Cited on page 126.)

[92] P.Hallbjorner. The significance of radiation efficiencies when using s-parameters to calculate the received signal correlation from two antennas. *IEEE Antennas and Wireless Propagation Letters*, 4:97–99, 2005. (Cited on pages 127 and 128.)

[93] W.L.Schroeder and A.Krewski. Total multi-port return loss as a figure of merit for mimo antenna system. In *Proceedings of the 40th European Microwave Conference*, 2010. (Cited on page 128.)

[94] K. Sekine and H. Iwasaki. Usb memory size antenna for 2.4 ghz wireless lan and uwb. In *Proceedings of the 38th European Microwave Conference*, 2008. (Cited on page 129.)

[95] A. Gummalla; M. Achour; G. Poilasne and V. Pathak. Compact dual-band planar metamaterial antenna arrays for wireless lan. In *Proceeding of IEEE Antennas and Propagation Society International Symposium*, 2008. (Cited on pages 129 and 158.)

[96] J. Kwon; D Kim; Y. Lee and J. Choi. Design of a mimo antenna for usb dongle application using common grounding. In *Proceeding of Advanced Communication Technology (ICACT)*, 2011. (Cited on page 129.)

[97] Z.N.Chen. Note on impedance characteristics of l-shaped wire monopole antenna. *Microwave and Optical Technology Letters*, 26(1):365–367, 2008. (Cited on page 131.)

[98] A.P.Feresidis; G.Goussetis; S.Wang and J.C.Vardaxoglou. Artificial magnetic conductor surface and their application to low-profile high-gain planar antennas. *IEEE Transactions on Antennas and Propagation*, 53(1):209–215, January 2005. (Cited on pages 141 and 142.)

[99] Y.Zhang; J.Hagen; M.Younis; C.Fischer and W.Wiesbeck. Planar artificial magnetic conductor and patch antennas. *IEEE Transactions on Antennas and Propagation*, 51(10):2704–2712, October 2003. (Cited on pages 143 and 146.)

[100] M.Hosseinipanah; Q.Wu. Characteristic estimation of artificial magnetic conductors. *Electromagnetics*, 30(5):435–447, 2010. (Cited on page 143.)

[101] O. Luukkonen; C. Simovski; G. Granet; G. Goussetis; D. Lioubtchenko; A.V. Raisanen and S.A. Tretyakov. Simple and accurate analytical model of planar grids and high-impedance surfaces comprising metal strips or patches. *IEEE Transactions on Antennas and Propagation*, 50(6):1624 – 1632, June 2008. (Cited on pages 145 and 146.)

[102] M.Hosseini and M.Hakkak. Characteristics estimation for jerusalem cross-based artificial magnetic conductors. *IEEE Antennas and Wireless Propagation Letters*, 7:58–61, 2008. (Cited on page 146.)

[103] B.R.Holland; R.Ramadoss; S.Pandey and P.Agrawal. Tunable coplanar patch antenna using varactor. *Electronic Letters*, 42(6):319–321, 2006. (Cited on page 146.)

[104] B.A.Cetiner; H.Jafarkhani and etc. Multifunctional Reconfigurable MEMS Integrated Antennas for Adaptive MIMO Systems. *IEEE Communications Magazine*, 42(12):62–70, 2004. (Cited on page 147.)

[105] G. H. Huff and J. T. Bernhard. Integration of Packaged RF MEMS Switches With Radiation Pattern Reconfigurable Square Spiral Microstrip Antennas. *IEEE Transactions on Antennas and Propagation*, 54(2):464–469, 2006. (Cited on page 147.)

[106] M.P.Daly and J.T.Bernhard. RF MEMS Switch Model for Reconfigurable Antenna Design. In *Proceeding of IEEE Antenna and Propagation Society international Symposium*, 2008. (Cited on page 147.)

[107] S. Su; J. Chou and Y. Liu. Printed coplanar two-antenna element for 2.4/5 GHz WLAN operation in a MIMO system. *Microwave and Optical Technology Letter*, 50(6):1635–1638, 2008. (Cited on page 158.)

[108] I. J. Bahl and D. K. Trivedi. A Designer's Guide to Microstrip Line. *Microwaves*, 16:174–182, May 1977. (Cited on page 167.)

[109] K.L. Wong; T.W. Kang and M.F.Tu. Internal mobile phone antenna array for lte/wwan and lte mimo operations. *Microwave and Optical Technology Letter*, 53(7):1569–1573, July 2011. (Cited on page 177.)